Electronic structure of complex oxides and sulphides, and statistical mechanics of Néel and structural transitions from first-principles

A Thesis

Submitted For the Degree of

DOCTOR OF PHILOSOPHY

in the Faculty of Science

by

Arpita Paul

THEORETICAL SCIENCES UNIT
JAWAHARLAL NEHRU CENTRE FOR ADVANCED SCIENTIFIC RESEARCH
Bangalore – 560 064

JULY 2017

To my family

DECLARATION

I hereby declare that the matter embodied in the thesis entitled "**Electronic structure of complex oxides and sulphides, and statistical mechanics of Néel and structural transitions from first-principles**" is the result of investigations carried out by me at the Theoretical Sciences Unit, Jawaharlal Nehru Centre for Advanced Scientific Research, Bangalore, India under the supervision of Prof. Umesh V. Waghmare and that it has not been submitted elsewhere for the award of any degree or diploma.

In keeping with the general practice in reporting scientific observations, due acknowledgement has been made whenever the work described is based on the findings of other investigators.

_____

Arpita Paul

CERTIFICATE

I hereby certify that the matter embodied in this thesis entitled "**Electronic structure of complex oxides and sulphides, and statistical mechanics of Néel and structural transitions from first-principles**" has been carried out by Ms. Arpita Paul at the Theoretical Sciences Unit, Jawaharlal Nehru Centre for Advanced Scientific Research, Bangalore, India under my supervision and that it has not been submitted elsewhere for the award of any degree or diploma.

Prof. Umesh V. Waghmare
(Research Supervisor)

Acknowledgements

I would like to thank my advisor Prof. Umesh V. Waghmare for his constant motivation and excellent guidance throughout my work. This work certainly would have been impossible without his guidance and constant support. His generosity and enormous patience cannot be exaggerated, and his style of Physics will forever influence my work.

I would also like to thank my collaborators: Dr. Priya Sharma, Prof. Goutam Sheet, Prof. Ashok K Ganguly, Prof. John P. Perdew, Prof. Jianwei Sun, Prof. J. Paul Attfield for fruitful scientific discussions.

I thank all the TSU faculty: Prof. Shobhana Narasimhan, Prof. Vidyadhiraja, Prof. Subir K. Das, Prof. SwapanK. Pati, Prof. Meher K. Prakash, Prof. Srikanth Sastry and Prof. Kavita Jain for the courses they have offered and the scientific interactions.

I would like to thank Prof. Chandrabhas Narayana for the interesting course and scientific interactions during the classes.

I am thankful to Department of Science and Technology (DST), India for a research fellowship.

I thank my present and past lab mates Anjali, Suchitra, Pawan, Koushik, Meha, Henu, Sweta, Anuja, Aseem, Simran, Sharmila, Summayya, Anjali, Vinay, Sandhya, Himanshu, Shashwat for many discussions.

I would like to acknowledge the Centre for Computational Material Science (CCMS), JNCASR for the computational facilities.

I would like to thank Librarian, Academic and Administrative staff for their efficiency and helpfulness.

I thank the Hostel staff, Mess workers and Chandraiah canteen for keeping me well fed.

Last but not the least, to the people I owe the most: my parents for their unconditional love and affection. To my grandmother for her blessings. To my brother and sister for their support and love. To my husband for his constant encouragement and support. To my in-laws for their love and moral support.

Synopsis

Oxides form an important class of materials that exhibit rich varieties of physical states and properties, such as ferroelectricity, antiferromagnetism, antiferroelectricity, piezoelectricity, giant magnetoresistance, superconductivity, charge and orbital orderings, along with a remarkable diversity in the nature of phase transitions (metal-insulator, magnetic, ferroelectric and structural transitions) they undergo. The exotic phenomena in oxides are attributed to the complex interplay between several degrees of freedom such as spin, charge and lattice. The fine tuning of physical properties of oxides by varying temperature, pressure and external fields give rises to novel phases.

We have used first-principles density functional theoretical (DFT) calculations to (a) identify the degrees of freedom that are relevant to the instabilities like antiferromagnetism, ferroelectricity, charge disproportionation and superconductivity, and (b) determine their couplings, i.e., electron-phonon coupling, spin-spin, spin-phonon, spin-strain, phonon-phonon couplings. We used effective Hamiltonian (microscopic) and Landau theory (macroscopic) to model their interactions and emerging behavior. We have demonstrated how effective Hamiltonians capture the microscopic mechanisms of magnetoelastic effect, formation of magnetic vortices, and ferroelectric phase transitions. We present a detailed study of Néel transition in hexagonal multiferroic $YMnO_3$ (Chapter 3), structural transitions in ferroelectric perovskites (Chapter 4), chemical and electronic instabilities in Lanthanide Ruthenium oxides (Chapter 5) and ferromagnetic superconductor, $Sr_{0.5}Ce_{0.5}FBiS_2$ (Chapter 6). In addition, we have assessed the accuracy of first-principles calculations by determining the interatomic interactions in perovskite oxides through the utilization of the newly developed SCAN metaGGA exchange-correlation functional, which accurately predicts the geometries and energies of diversely bonded (from hydrogen bonding to

ionic bonding) molecules and materials.

List of Publications

(1) Spin-orbit interaction, spin-phonon coupling, and anisotropy in the giant magnetoelastic effect in $YMnO_3$, **Arpita Paul**, Priya Sharma and Umesh V. Waghmare, Phys. Rev. B **92**, 054106 (2015).

(2) Evidence of a pseudogap driven by competing orders of multi-band origin in the ferromagnetic superconductor $Sr_{0.5}Ce_{0.5}FBiS_2$, Mohammad Aslam, **Arpita Paul**, Gohil S Thakur, Sirshendu Gayen, Ritesh Kumar, Avtar Singh, Shekhar Das, Ashok K Ganguli, Umesh V Waghmare and Goutam Sheet, J. Phys.: Condens. Matter **28**, 195701 (2016).

(3) Accurate first-principles structures and energies of diversely bonded systems from an efficient density functional, Jianwei Sun, Richard C. Remsing, Yubo Zhang, Zhaoru Sun, Adrienn Ruzsinszky, Haowei Peng, Zenghui Yang, **Arpita Paul**, Umesh Waghmare, Xifan Wu, Michael L. Klein and John P. Perdew, Nature Chemistry **8**, 831836 (2016)

(4) Accuracy of first-principles interatomic interactions and predictions of ferroelectric phase transitions in perovskite oxides: Energy functional and effective Hamiltonian, **Arpita Paul**, Jianwei Sun, John P. Perdew, Umesh V. Waghmare, Phys. Rev. B **95**, 054111 (2017).

(5) Ab-initio statistical mechanics of Nel transition, magnetic domains and topological defects in hexagonal $YMnO_3$, **Arpita Paul** and Umesh V. Waghmare

(manuscript under preparation)

(6) First-principles study of electronic structures of stoichiometric and non-stoichiometric Lanthanide Ruthenium oxide perovskites, **Arpita Paul**, J. Paul Attfield and Umesh V. Waghmare (manuscript under preparation)

(7) **Book chapter: Arpita Paul** and Umesh V. Waghmare, Phosphorene, in 2-D Inorganic Materials beyond Graphene, CNR Rao and Umesh V. Waghmare, World Scientific Publishing, in Press

List of Figures

1.1 Coupling between different degrees of freedom and emergent properties of a material. 2
1.2 Splitting of five-fold degenerate d levels in the octahedral crystal field. 6
1.3 Superexchange interaction in antiferromagnetic insulator MnO. 7
1.4 (a) Proper ferroelectric ($BaTiO_3$) and (d) improper ferroelectric ($TbMnO_3$). (b) Dzyaloshinskii-Moriya (DM) interaction and (c) weak ferromagnetism in $LaCu_2O_4$ induced due to DM interaction. 9
1.5 Order parameter as a function of temperature: (a) first order and (b) second order phase transitions. 11

2.1 Iterative scheme used to solve the Kohn-Sham equations self-consistently. 22
2.2 Schematic representation of all-electron wavefunction in the Coulomb potential (dotted line) in comparison with pseudo wavefunction in pseudopotential (solid line). 29

3.1 The crystal structure of $YMnO_3$ below Néel temperature. 41
3.2 Schematic diagram of configurations of magnetic ordering corresponding to different irreducible representations: (a) Γ_1, (b) 1^{st} basis vector of Γ_2 (Γ_2(I) ordering), (c) 2^{nd} basis vector of Γ_2 (Γ_2(II) ordering), (d) 1^{st} basis vector of Γ_3 (Γ_3(I) ordering), (e) Γ_4 and (f) 2^{nd} basis vector of Γ_3 (Γ_3(II) ordering). 42
3.3 Electronic structure of noncollinearly ordered magnetic and NM states of $YMnO_3$: (a) electronic density of states (O_{eq} and O_{ap} are equatorial and apical oxygen ions respectively) and (b) band structure. 45

3.4 Schematic diagram of evolution of energies of $3d$ orbitals of Mn^{3+} ion: (I) effect of trigonal bipyramidal crystal field (Δ_{CF} is the energy difference between two lowest lying doublets), (II) effect of spin-orbit coupling (λ is the strength of spin-orbit coupling) and (III) effect of magnetic exchange splitting (Δ_{xc} is the energy difference between up and down spin levels coming from exchange splitting). 47
3.5 m_j projected density of states: (a) and (b) Γ_3(I) magnetic state (orderings of spins in the ***ab*** plane), (c) and (d) Γ_3(II) magnetic state (spins are along ***c*** axis). 49
3.6 Phonon density of states at Γ point of noncollinearly ordered magnetic and nonmagnetic states of $YMnO_3$. 51
3.7 Due to the change of magnetic ordering from Γ_3(I) to Γ_3(II) forces (in the scale of mRy/bohr) acting on: (a) O1 and O2 atoms, (b) Y1 and Y2 atoms. Pictorial representation of independent atomic displacements with Γ_1 symmetry: (c) 1st basis vector, (d) 2nd basis vector for apical oxygen atoms (O1 and O2), (e) basis vector for yttrium atoms (Y1 and Y2) and (f) basis vector for equatorial oxygen atoms (O3 and O4). 57
3.8 Visualization of the eigendisplacements of zone-centre phonon modes having Γ_1 symmetry of magnetic phases with Γ_3(I) ordering with frequencies: (a) 666 cm^{-1}, (b) 484 cm^{-1}, (c) 450 cm^{-1}, (d) 152 cm^{-1} and (e) 236 cm^{-1} show strong overlap with the forces acting on atoms which arises due to the change of magnetic ordering from Γ_3(I) to Γ_3(II). 60
3.9 Visualization of the eigen-displacements of zone-centre phonon modes (side view) with Γ_1 symmetry having frequencies of (a) 264 cm^{-1} (Γ_3(I) phase) and (b) 279 cm^{-1} (Γ_3(II) phase). 61
3.10 Temperature variations of (a) antiferromagnetic order parameters (A and M), (b) specific heat (C_V), (c) magnetic susceptibilities associated with A and M (χ_A and χ_M) and (d) amplitude of the phonon mode (u). 64
3.11 (a) Variations of Binder cumulants associated with A and M with temperature and (b) distribution of A at 2 K (low temperature phase) and 68 K (high temperature phase). 66

3.12 (a) A type, (b) -A type magnetic orderings are represented by θ_1 and θ_2 angles. (c) stripe domains of magnetic orderings and Γ_1 magnetic ordering at the 180° domain wall. 67
3.13 In-plane displacements of O1 atoms (red color) according to K_3 phonon mode with (a) Φ=$2\pi/3$, (c) Φ=0 and (d) Φ=-$2\pi/3$. (b) Displacements of yttrium (Y1 and Y2 in purple color) and equatorial oxygen (O3 and O4 in red color) atoms according to K_3 phonon mode. 68
3.14 (a) Magnetic ordering (magnetic moments of Mn atoms) according to Γ_3 symmetry, (c) atomic displacements (O1 atoms) according to Γ_1 phonon mode. (b) Hexagon formed by six Mn atoms to define magnetic states (A, A' and A''). 69
3.15 Temperature variations of (a) and (e) magnetic order parameters (A, A', A'' and M), (b) and (f) specific heat (C_V), (c) and (g) amplitude of the phonon mode (u, u' and u''), (d) and (h) magnetic susceptibilities associated with A, A', A''. 72
3.16 Stripe domains of magnetic orderings at 2 K in the ***ab*** plane. 73
3.17 Magnetic vortex and antivortex states obtained with (a) periodic boundary condition and (b) open boundary condition. 74

4.1 Optimized lattice constants of eight cubic oxides using the SCAN meta-GGA functional in comparison with experimental and earlier theoretical (using LDA) lattice parameters. 82
4.2 Direct band gaps of eight perovskites in comparison with earlier theoretical results using LDA and experimentally measured band gaps. . 86
4.3 Variations of total energies of unstrained (a) $BaTiO_3$ and (b) $PbTiO_3$ as a function of polar structural distortions (u) along [001] and [111] directions respectively, from SCAN. 91
4.4 Eigenvalue (κ_x) of x-polarized soft mode (with Γ_{15} symmetry) of $BaTiO_3$ as functions of strains applied (a) along x (η_1) and (b) y (η_2) directions, from SCAN. 92
4.5 Calculated energy difference (using fourth-order expansion of energy as a function of soft mode amplitude) between cubic (E_C) and tetragonal (E_T) phases of perovskites in comparison with earlier theoretical results using LDA. 93

4.6 Half of the eigenvalues of (a) short-range interaction matrix and (b) total (long- and short-range) interaction matrix along the high symmetry directions of $BaTiO_3$. 98
4.7 Simulated temperature dependence of lattice parameters of (a) $BaTiO_3$, (b) $KNbO_3$ and (c) $PbTiO_3$ at zero pressure. 101
4.8 Projection of forces arising due to the freezing of soft mode (a) on v_1 and (b) v_2 modes of $BaTiO_3$. Eigenvalues of (c) v_1 and (d) v_2 modes as a function of soft mode amplitude (u). 106
4.9 Estimated T_C's of (a) $BaTiO_3$, (b) $KNbO_3$ and (c) $PbTiO_3$ including the fourth-order coupling between soft and higher energy phonon modes. 109

5.1 Crystal structure of lanthanide (La/Y) ruthenium oxide. 115
5.2 Spin-resolved electronic density of states of $LaRuO_3$: (a) with ferromagnetic ordering, (b) antiferromagnetic ordering in the absence of Hubbard U and (c) ferromagnetic and (d) antiferromagnetic orderings in the presence of Hubbard U parameter (U=3.0 eV). 117
5.3 Spin-resolved electronic density of states of $YRuO_3$: (a) with ferromagnetic and (b) antiferromagnetic orderings with using Hubbard U parameter (U=3.0 eV). 118
5.4 Electronic density of states of $LaRuO_3$ in the presence of spin-orbit coupling: (a) ferromagnetic, (b) antiferromagnetic states without using Hubbard U and (c) ferromagnetic and (d) antiferromagnetic states with using Hubbard U (U=2.0 eV). 120
5.5 Spin-resolved electronic density of states with using Hubbard U (U=3.0 eV): (a) ferromagnetic $LaRu_{0.88}O_3$, (b) antiferromagnetic $LaRu_{0.88}O_3$, (c) ferromagnetic $YRu_{0.88}O_3$ and (d) antiferromagnetic $YRu_{0.88}O_3$. . . 121
5.6 Spin resolved density of states projected on Ru $4d$ orbitals of $LaRuO_3$ and $YRuO_3$. 123

6.1 Different types of point-contact spectra obtained on $Sr_{0.5}Ce_{0.5}FBiS_2$: (a) a representative spectrum of **type A**. The double peaks structure symmetric about $V = 0$ indicated by arrows is a hallmark of Andreev reflection in NS point-contacts. (b) a representative spectrum of **type B**. (c) Temperature dependence of a spectrum of **type A** with BTK fits (indicated by solid lines) of each spectra. (d) Temperature dependence of a representative spectrum of **type B**. 129

6.2 (a) Crystal structure of bulk $Sr_{0.5}Ce_{0.5}FBiS_2$. (b) spin resolved electronic density of states of bulk $Sr_{0.5}Ce_{0.5}FBiS_2$. Spin resolved Fermi surface contributed by three bands crossing Fermi level: (c) band **A** for majority spin, (d) band **B** for majority spin, (e) band **C** for majority spin, (f) band **A** for minority spin, (g) band **B** for minority spin and (h) band **C** for minority spin. Superlattice $SrCeF_2Bi_2S_4Pd_4$: (j) crystal structure and (k) spin resolved electronic density of states. . . 132
6.3 Spin resolved electronic structure of bulk $Sr_{0.5}Ce_{0.5}FBiS_2$: (a) band structure for majority spin and (b) band structure for minority spin. . 133
6.4 (a) Atomic displacements of A_{1g} phonon mode having frequency 46 cm $^{-1}$, which exhibits a strong electron phonon coupling and (b) distribution of frequency of phonons at Γ point of bulk $Sr_{0.5}Ce_{0.5}FBiS_2$. Change in the electronic density of states of bulk $Sr_{0.5}Ce_{0.5}FBiS_2$ after freezing the phonon mode with frequency 46 cm^{-1}: (c) projected on Sr $5s$ orbital and (d) projected on Ce $4f$ orbital. 135
6.5 Spin resolved Fermi surface contributed by three bands crossing Fermi level of superlattice: (a) band **A** for majority spin, (b) band **B** for majority spin, (c) band **C** for majority spin, (d) band **A** for minority spin, (e) band **B** for minority spin and (f) band **C** for minority spin. . 136

7.1 Schematic summarizing all the work presented in this thesis. 141

List of Tables

3.1 Total energies of magnetic and nonmagnetic phases of $YMnO_3$ per unit cell with six formula unit relative to the ground state configuration $\Gamma_3(I)$. 43

3.2 Phonon frequencies (in cm^{-1}) of silent modes at Γ point calculated from first-principles for magnetic and nonmagnetic phases of $YMnO_3$ in comparison to frequencies calculated using LSDA + U method. . . 52

3.3 Raman active phonon frequencies (in cm^{-1}) calculated from first-principles for magnetic and nonmagnetic phases of $YMnO_3$ in comparison with frequencies calculated using LSDA + U method and experimentally observed Raman and IR (given in parenthesis) active modes below and above T_N. 53

3.4 Born effective charges of noncollinear antiferromagnetic phase with Γ_3(I) ordering of hexagonal $YMnO_3$ calculated from first-principles in comparison with the values calculated using self-interaction corrected LSDA method. 54

3.5 Calculated bond lengths (in Å) and bond angles (in °) of several magnetic states of $YMnO_3$. 56

3.6 Coupling of force arising due to the change of magnetic ordering from Γ_3(I) to Γ_3(II) with the phonon modes of magnetic phase of $YMnO_3$ with Γ_3(I) ordering. 59

3.7 Transformation of order parameters under the operations of symmetry elements of $P6_3/mmc$ space group. 69

4.1 Optimized tetragonal lattice parameters (in Å) and z component of atomic displacements (from cubic to tetragonal phase) for $BaTiO_3$ and $PbTiO_3$ using the SCAN meta-GGA functional in comparison with earlier theoretical and experimental results. 83

4.2 Optimized lattice parameters of orthorhombic and rhombohedral phases of $BaTiO_3$ and $KNbO_3$ using the SCAN meta-GGA functional in comparison with earlier theoretical and experimental results. 84
4.3 Elastic constants (in GPa) of cubic perovskites using the SCAN meta-GGA functional in comparison with earlier theoretically-calculated values using LDA and experimentally-measured values 85
4.4 Predicted zone-centre optical phonon frequencies (in cm^{-1}) of $BaTiO_3$, $PbTiO_3$, $SrTiO_3$ and $KNbO_3$ at theoretical lattice constants in comparison with earlier theoretically-calculated and experimentally-measured frequencies 88
4.5 Harmonic (κ in eV/Å^2), anharmonic (α and γ in eV/Å^4) and strain-phonon coupling parameters (B_{1xx}, B_{1yy} and B_{4yz} in eV/Å^2) in comparison with earlier theoretically-calculated values using LDA. 89
4.6 Computed eigenvectors (ξ_z^{atom} (unitless)) and amplitudes of the soft modes of eight perovskites in comparison with earlier LDA results. . . 90
4.7 Calculated local and short-range interaction parameters (in eV/Å^2) of $BaTiO_3$, $PbTiO_3$ and $KNbO_3$ in comparison with earlier theoretical results determined using LDA and WC-GGA functionals 99
4.8 Estimated T_C's of $BaTiO_3$, $PbTiO_3$ and $KNbO_3$ in comparison with earlier theoretical and experimental T_C's 103

5.1 Our estimated bandgaps and energies (with respect to ferromagnetic state) and local magnetic moment of Ru atom (μ in the unit of μ_B) of ferromagnetic and antiferromagnetic states of lanthanide ruthenium oxides. 119
5.2 Our estimated bandgaps and energies (with respect to ferromagnetic state) of ferromagnetic and antiferromagnetic states of nonstoichiometric $LnRuO_3$. 122
5.3 Distortions of RuO_6 octahedra in stoichiometric and nonstoichiometric $LnRuO_3$ with ferromagnetic ordering in presence of Hubbard U (=3.0 eV) parameter. 124

6.1 Fermi velocities in the bands crossing Fermi level of bulk $Sr_{0.5}Ce_{0.5}FBiS_2$. 133

Contents

Acknowledgements **v**

Synopsis **vii**

List of Publications **ix**

List of Figures **xi**

List of Tables **xvii**

1 Introduction **1**

1.1 Magnetic oxides 3

1.2 Ferroelectric oxides 8

1.3 Symmetry breaking phase transition 10

1.4 Overview 12

2 Methodology **16**

2.1 Introduction 17

2.2 Density Functional Theory 19

2.2.1 Hohenberg-Kohn theorems 19

2.2.2 Kohn-Sham ansatz 20

2.2.3 Exchange-correlation functionals 23

2.2.4 Basis sets 25

2.2.5 Full potential linearly augmented plane wave (FLAPW) method . 27

2.2.6 Pseudopotentials 28

2.2.7 Frozen phonon method 29

2.2.8 Density functional perturbation theory 31

2.3 Limitations of density functional theory 33

3 Hexagonal $YMnO_3$: spin-phonon coupling, spin-orbit coupling and magnetic domain structures 34

3.1 Introduction 34
3.2 Methods 39
3.3 Symmetry of crystal structure and magnetic ordering 40
3.4 Results and discussions 42
3.4.1 Magnetic ground state and electronic origin of its stability 42
3.4.2 Phonons 50
3.4.3 Born effective charges 54
3.4.4 Spin-phonon coupling 55
3.4.5 Properties at T>0 K 61
3.4.5.1 Results of Monte Carlo simulations 63
3.4.5.2 Structural and magnetic states 67
3.5 Summary 75

4 Accuracy of first-principles interatomic interactions and predictions of ferroelectric phase transitions in perovskite oxides 77

4.1 Introduction 77
4.2 Methods 80
4.3 Results and discussion 81
4.3.1 Ground-state properties 81
4.3.1.1 Structural and electronic properties 81
4.3.1.2 Vibrational properties 86
4.3.2 Finite temperature properties 94
4.3.2.1 Effective Hamiltonian 94
4.3.2.2 MD simulations 98
4.3.3 Anharmonic coupling between phonons 104
4.4 Summary 110

5 Lanthanide ruthenium perovskite oxides: electronic properties 112

5.1 Introduction 112
5.2 Methods 114
5.3 Results and discussion 115
5.3.1 Stoichiometric $LnRuO_3$ 115
5.3.1.1 Effect of Hubbard U 116

5.3.1.2 Effect of spin-orbit coupling 119
5.3.2 $LnRu_{1-\delta}O_3$ 120
5.4 Summary 125

6 Competing electronic orders in ferromagnetic superconductor $Sr_{0.5}Ce_{0.5}FBiS_2$ 127
6.1 Introduction 127
6.2 Crystal structure and computational details 130
6.3 Results and discussions 131
6.3.1 Electronic structure 131
6.3.2 Electron phonon coupling 134
6.3.3 Interaction with Pd layers 134
6.4 Summary 137

7 Summary 138

Bibliography 142

Chapter 1

Introduction

Oxides are mostly non-toxic and quite abundant in nature. They form an important class of materials due to their chemical and structural (halite, wurzite, spinel, corrundum, rutile, perovskite and pyrochlore) diversity. Oxides with transition metal ions have been studied greatly as these exhibit rich varieties of physical properties such as metallicity, semiconductivity, insulating, ferromagnetism, antiferromagnetism, ferroelectricity, antiferroelectricity, piezoelectricity, colossal magnetoresistance, superconductivity, charge and orbital orderings [1–9] along with a remarkable diversity in the nature of phase transitions (high-spin/low spin, metal-insulator, magnetic, ferroelectric and structural transitions) they undergo [2, 4, 5, 10–13].

The macroscopic properties of a material are a consequence of how electrons and atoms are arranged and held together in a solid. Since the motion of electrons (atoms) is governed by quantum mechanical laws (Newtonian mechanics), most of the physical properties can be determined in principle from these laws. Accurate evaluation of the macroscopic properties of a material directly from the fundamental equations (first-principles) of electrons is of fundamental importance, but also quite difficult. The introduction of density functional theory by Kohn and Sham [14]

marked a breakthrough in first-principles computational techniques. Physical properties of a material such as electronic structure, stress, elastic constant, polarization, magnetic state and vibrational properties can now be estimated, thanks to the advances in computational power and algorithms of first-principles methods. It also gives access to the atomistic information, which is sometimes challenging to obtain from experiments.

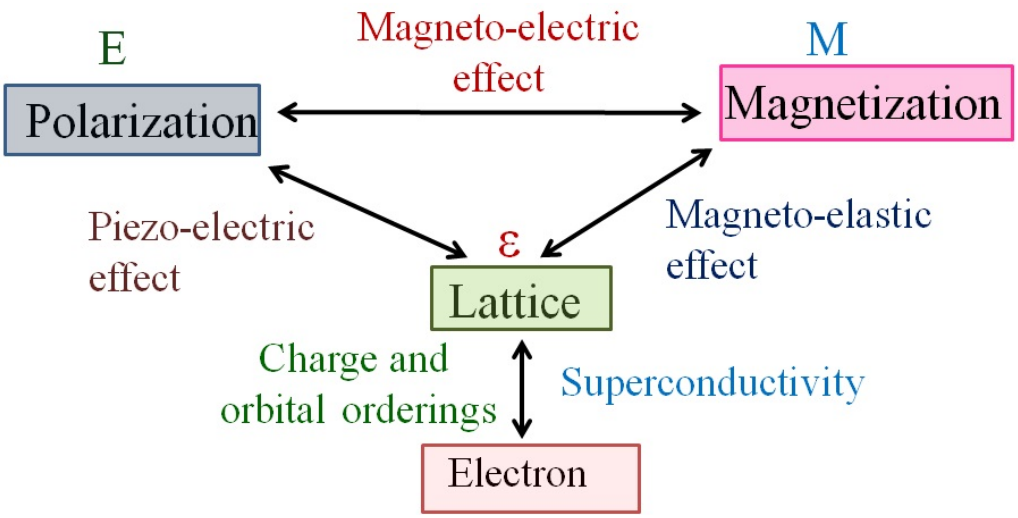

Figure 1.1: Coupling between different degrees of freedom and emergent properties of a material. E, M and ε denote externally applied electric field, magnetic field and mechanical stress on the system respectively.

The coupling between several degrees of freedom (e.g., electronic charge, spin and lattice) at the microscopic level dictates the behaviour of a material (see Figure 1.1). We have used first-principles density functional calculations to (a) identify different degrees of freedom that are relevant to the instabilities such as antiferromagnetism ($YMnO_3$), ferroelectricity (ABO_3), charge disproportionation ($LnRuO_3$) and superconductivity ($Sr_{0.5}Ce_{0.5}FBiS_2$), (b) determine their couplings such as spin-spin, spin-phonon, electron-phonon, spin-strain, strain-phonon couplings, and (c) model their interactions using Landau theory (macroscopic) and effective Hamiltonian (microscopic). Emergence of physical properties from these interactions is fundamentally interesting and the focus of this thesis is on interaction among phonons

and electrons in magnetic and ferroelectric oxides.

1.1 Magnetic oxides

Magnetism in a solid is closely linked with the quantum mechanical angular momentum of its electrons. According to the Bohr's model, the z component of orbital angular momentum (L) is quantized in the unit of $\hbar$. The eigenvalue of L_z is $m_L\hbar$ with m_L=0, $\pm$1, $\pm$2, ..., $\pm L$. The magnetic moment contributed by the orbital angular momentum can be expressed as,

$$\begin{aligned} \mu_{L,z} &= \frac{e}{2m_e} m_L \hbar, \\ &= m_L \mu_B. \end{aligned} \tag{1.1}$$

μ_B is Bohr-magneton (fundamental unit of atomic scale magnetism). An electron also possesses intrinsic angular momentum (apart from orbital angular momentum), S known as the spin. The spin magnetic moment of electron is written as,

$$\mu_{S,z} = 2 m_S \mu_B, \tag{1.2}$$

where m_S (z component of S) can take integer or half-integer values ranging from -S to S in increment of one unit at each step.

The net magnetic moment of filled electronic shells ($1s$, $2s$, $2p$ etc) is zero ($\sum_L m_L$=0 and $\sum_S m_S$=0). Magnetic moment of partially filled electronic shells can be nonzero. When the coupling between L and S (spin-orbit coupling) is strong, the total angular momentum (J) is the conserved angular momentum even though $\hat{L}$ and $\hat{S}$ change. The allowed values of J range from |L-S| to (L+S) in increments

of one unit. The total magnetic moment of a free ion can be written as,

$$\mu_{J,z} = g_J m_J \mu_B, \tag{1.3}$$

where g_J is the Landé-g factor [15] and m_J is the azimuthal angular momentum quantum number (from -J to +J in increment of one unit at each step). According to the Hund's rule, electrons (in a multi-electron system) occupy the states in a way to maximize the angular momentum. In this way, Coulomb repulsion energy is minimized because the Pauli exclusion principle forces electrons to occupy different orbitals. Magnetic properties of transition metal oxides arise from the partially filled d levels of transition metal ion. We now discuss the interaction of a magnetic ion with its neighbouring nonmagnetic and magnetic ions in a lattice.

The free magnetic ions are subjected to static electric field originating from the interaction with surrounding negatively charged nonmagnetic ions (oxygen ion in transition metal oxides) in the lattice. This electrostatic field is known as the crystal field. The effect of crystal field is stronger in transition metal ions containing d electrons. As $4f$ orbitals are shielded by filled $5s$ and $5p$ orbitals, the effect of crystal field on those orbitals is much weaker. The kind of splitting of d levels induced by crystal field critically depends on the symmetry of the local environment. The electronic charge distribution in a d orbital is aspherical. Thus, d electrons close to the negatively charged ion (ligand) will have higher energy compared to those which are far from ligand. There is a remarkable diversity in the geometry (octahedral, tetrahedral, square planer, square antiprismatic, square pyramidal, trigonal bipyramidal, pentagonal bipyramidal) of the crystal field in most commonly known structures of transition metal oxides. As an example, five degenerate d levels in the octahedral crystal field (see Figure 1.2) split into a lowest lying triply degenerate

state (t_{2g}) and one doubly degenerate (e_g) state with higher energy. The competition between crystal field and Coulomb repulsion energy gives rise to high-spin and low-spin states of magnetic ions in transition metal oxides [10, 16].

When the degenerate d orbitals are partially filled in the ground state, it is energetically favorable to spontaneously distort an octahedron (surrounding transition metal ion), as the cost of increased elastic energy is balanced by the resulting gain in electronic energy from the distortion. This effect is known as Jahn-Teller distortion [16]. The ligand (oxygen) ions surrounding the magnetic (transition metal) ion change their positions in a crystal to remove the orbital degeneracy by creating an asymmetry in different directions. To explain the Jahn-Teller effect, we consider the splitting of d levels of Mn^{3+} ion (d^4 configuration) in the octahedral crystal field (see Figure 1.2). Three d electrons occupy the $t_{2g,\uparrow}$ state and one d electron occupy the $e_{g,\uparrow}$ state (energy required to doubly occupy a state is larger than crystal field splitting energy). Here, the ground state of Mn^{3+} ion is two-fold degenerate. The tetragonal elongation of the octahedron along z direction induced by Jahn-Teller distortion lifts the degeneracy of ground state (see Figure 1.2). The Jahn-Teller distortion is also associated with charge and orbital orderings observed in Fe_3O_4, $YNiO_3$ and $Ln_{1-x}A_xMnO_3$ (Ln=Rare earth, A=Ca and Sr) [8, 17, 18].

The magnetic moment of a magnetic ion in a crystal lattice couples to the magnetic moments of neighbouring magnetic ions via magnetic exchange interactions. The exchange interaction is a quantum mechanical effect and arises as a consequence of overlap of electronic orbitals and Pauli exclusion principle. The total wavefunction of two electrons is composed of the product of spatial and spin parts and it is necessary for it to be antisymmetric. When the spin part of the wavefunction is antisymmetric (singlet state) then the spatial part is forced to be symmetric, symmetric triplet state (spin) forces the antisymmetric spatial part. The exchange integral is the differences in energies of singlet and triplet states. When the exchange integral is

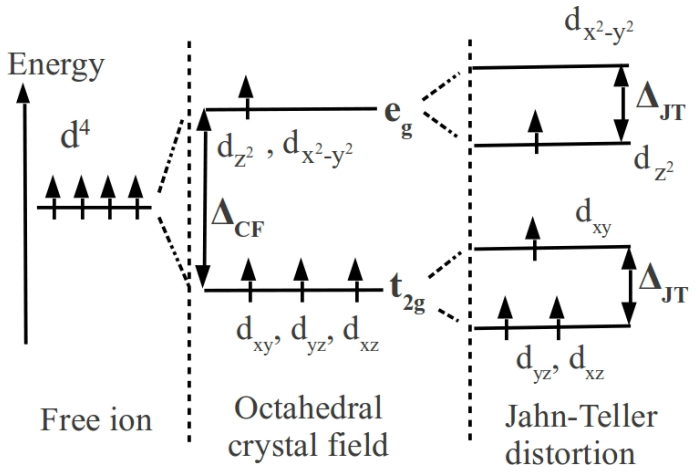

Figure 1.2: Splitting of five-fold degenerate d levels in the octahedral crystal field. Δ_{CF} and Δ_{JT} are the energy associated with crystal field splitting and Jahn-Teller distortion respectively.

negative, the ferromagnetic alignment of magnetic moments is energetically favored, whereas the antiferromagnetic alignment is favored for positive exchange integral.

In the absence of any exchange interaction, the magnetic moments are randomly oriented at any temperature in the absence of magnetic field. The presence of long-range magnetic ordering in magnetic oxides below the Curie temperature is a result of magnetic exchange interaction. Its strength depends on the geometric connectivity (and overlap of orbitals) between the two magnetic ions. When the electronic orbitals of magnetic ions directly overlap with each other, then the exchange interaction is known as direct. However, magnetic exchange interaction can be indirect in nature. In superexchange mechanism, the exchange interaction is mediated by a nonmagnetic ion connecting the two magnetic ions [16, 19]. As an example, the superexchange interaction between Mn^{2+} ions in MnO (see Figure 1.3) involves virtual transfer of two electrons [19]. First an electron from p state of oxygen ion is transferred to the d state of one of the Mn^{2+} ion. Then, one electron from d state of another Mn^{2+} ion is transferred to the p state (see Figure 1.3). Thus, the virtual electron transfer from one magnetic ion to another via nonmagnetic ion develops an effective exchange coupling between them.

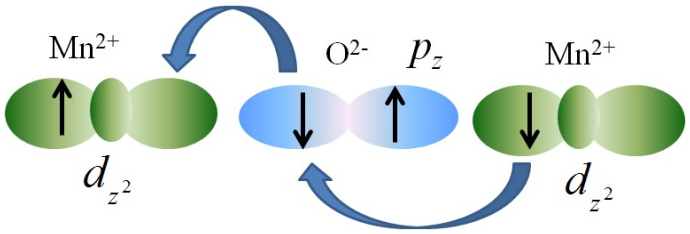

Figure 1.3: Superexchange interaction in antiferromagnetic insulator MnO.

The strength of superexchange interaction in transition metal oxides strongly depends on the overlap between d orbital of transition metal ion (TM) and $2p$ orbital of oxygen ion, i.e., bond length (TM-O) and bond angle (TM-O-TM). The sign of superexchange interaction is determined by the occupancy and orbital degeneracy of d states. According to Goodenough Kanamori rules [15], the superexchange interaction is antiferromagnetic when virtual electron transfer occurs between overlapping orbitals (TM-O-TM bond angle is 180°) which are half-filled (e.g. Figure 1.3). If the virtual electron transfers from a half-filled orbital of one magnetic ion to an empty orbital of another magnetic ion then the superexchange interaction is ferromagnetic. Also, when the TM-O-TM bond angle is 90°, the exchange interaction can be ferromagnetic in nature (even in half-filled case).

Dzyaloshinskii and Moriya proposed another kind of anisotropic magnetic exchange interaction in transition metal oxides, which originates from the relativistic correction to the superexchange interaction. The Dzyaloshinskii-Moriya interaction is expressed as,

$$H_{DM} \propto \lambda(\mathbf{x} \times \mathbf{r}_{12}).(\mathbf{S}_1 \times \mathbf{S}_2). \tag{1.4}$$

Two magnetic ions (with magnetic moments S_1 and S_2) are separated by r_{12} and x is the vector pointing towards oxygen ion from r_{12} (see Figure 1.4b). The strength of Dzyaloshinskii-Moriya interaction (λ) depends on the spin-orbit coupling constant. This interaction favors noncollinear arrangements of magnetic moments (see Figure 1.4b) in a lattice, in which O is at a site without spatial inversion symmetry. Weak

ferromagnetism associated with canting of magnetic moments (see Figure 1.4c) in $BiFeO_3$ is a result of Dzyaloshinskii-Moriya interaction [4].

Our work explains the observed magnitude of magnetic moment of Mn^{3+} ion in hexagonal $YMnO_3$ by considering the splitting and ordering of d levels induced by a combination of crystal field, spin-orbit and magnetic exchange interaction. We determine the spin and oxidation states of Ru atoms in orthorhombic $LnRu_{1-\delta}O_3$ using first-principles analysis.

1.2 Ferroelectric oxides

Ferroelectric materials are insulators, exhibiting a spontaneous electric polarization. Polarization is an outcome of arrangement of charge and polar bonds which breaks the spatial inversion symmetry (noncentrosymmetric). This polarization vanishes above the Curie temperature in the paraelectric phase (centrosymmetric). The spatial inversion symmetry in the paraelectric phase suggests two possible orientations of polarization (P and -P) in the ferroelectric phase. An externally applied electric field (E) can switch the direction of polarization through its coupling with polarization ($-E.P$), because of which ferroelectric materials have applications in memory devices. They can also be used in actuators and sensors due to linear piezoelectric coupling [20–22]. Experimentally, ferroelectricity was first observed by J. Valasek in Rochelle salt in 1920 [23]. Rochelle salt has a complex structure and is also unstable against dehydration. The breakthrough in ferroelectrics came from the discovery of ferroelectricity in potassium dihydrogen phosphate (KH_2PO_4) in 1935 by Busch and Scherer [24]. In this material, ferroelectricity is from the ordering of hydrogen bonds [25]. However, ferroelectricity exists in transition metal oxides such as $BaTiO_3$, $KNbO_3$ and $PbTiO_3$ with perovskite structure [12, 13]. In these oxides, transition metal ion has empty d shells (d^0). Perovskite oxides have a chemical

formula ABO_3, with the A cation at the corner of the cube, and B and O atoms located at the body-centered and face-centered positions respectively. Breaking of inversion symmetry takes place by the off-centering displacements of A/B cations associated with the soft polar phonon modes (see Figure 1.4). As an example, off-centerings of Ti atoms in $BaTiO_3$ and Pb atoms in $PbTiO_3$ induce ferroelectricity in these compounds [26–28]. In addition to Ti, the stereochemically active lone pair of electrons of Pb is responsible for its off-centering in $PbTiO_3$ in contrast to that in $BaTiO_3$ [29]. Polarization in perovskite oxides is proportional to the amplitude of the off-centering displacements of cations relative to anions.

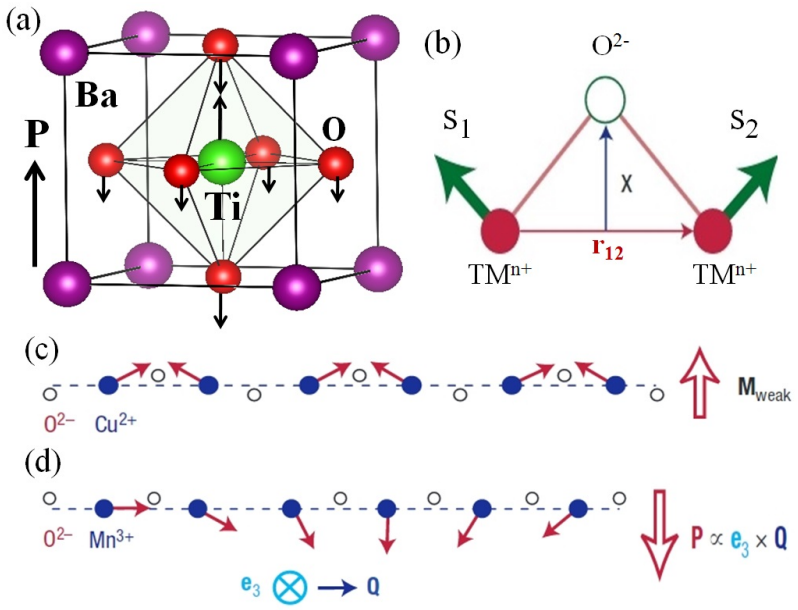

Figure 1.4: (a) Proper ferroelectric ($BaTiO_3$) and (d) improper ferroelectric ($TbMnO_3$). (b) Dzyaloshinskii-Moriya (DM) interaction and (c) weak ferromagnetism in $LaCu_2O_4$ induced due to DM interaction. e_3 is the rotation axis of spins and Q represents the wavevector associated with the spin spiral. Reprinted by permission from Macmillan Publishers Ltd: (Nature) [4], copyright (2007).

There is another class of ferroelectric materials known as improper ferroelectrics where the polarization appears as a secondary effect of another non-polar ordering. For example, polarization in hexagonal $YMnO_3$ emerges as a result of nonlinear coupling of polarization with zone boundary phonon which is the primary order

parameter of its structural transition [4]. If the charges of transition metal ions order in a noncentric fashion in charge ordered insulators ($LuFe_2O_4$), it can induce ferroelectric polarization [4]. A spiral ordering of magnetic moments in $TbMnO_3$ (see Figure 1.4) breaks the spatial inversion symmetry, and induces ferroelectric polarization [4]. The materials in which ferrolectricity and magnetic order coexist are known as multiferroics (e.g., $BiFeO_3$, $YMnO_3$ and $TbMnO_3$).

We determine the interatomic interactions relevant to ferroelectric transitions in cubic ABO_3 perovskites from first-principles and assess the accuracy with which we can estimate T_C's. Our work also investigates the indirect coupling between antiferromagnetic and ferroelectric order parameters in hexagonal $YMnO_3$.

1.3 Symmetry breaking phase transition

A stable phase of a material and is controlled by thermodynamic variables such as temperature, pressure and volume, and macroscopic properties can be qualitatively different in phases of different symmetry. Transitions among different phases are common in nature, and characterized by discontinuities in the free energy.

In a symmetry breaking transition, the high symmetric phase transforms to low symmetric phase (see Figure 1.5) as a function of thermodynamic variables. The driving fields in commonly known symmetry breaking transitions are temperature, pressure, electric and magnetic fields. The space groups of the phases have group-subgroup relationship across the transition. Examples of symmetry breaking transitions are ferromagnetic, ferroelectric and structural transitions. Magnetic moments are randomly oriented in the paramagnetic phase above the transition temperature (T_C), whereas they order ferromagnetically in the low temperature phase. The high temperature phase is more disordered than the low temperature phase, but more symmetric in average sense. Structural transitions are driven by unstable phonon

modes (zone centre or zone boundary). The phonon mode (zone centre or zone boundary) softens with reducing temperature at the transition, and again hardens below it as the system stabilizes in the equilibrium distorted structure. The periodicity of the structure remains unchanged if the transition is associated with zone-centre mode, whereas the periodicity changes in transitions associated with zone boundary mode.

A phase transition is clearly revealed in the order parameter (e.g., magnetization and polarization), which is a measure of degree of order in a system undergoing transition. The order parameter (ψ) has a finite value in the low temperature phase (below T_C), whereas it is zero in the high temperature phase (see Figure 1.5). In the first-order phase transition, the order parameter shows a jump at the transition temperature, and this transition is associated with a latent heat. In contrast, the order parameter varies continuously with temperature in the second order phase transition. The specific heat and susceptibility (associated with order parameter) exhibit divergence near the transition temperature in the second order transitions, while they are cut off at a finite value in first-order transition.

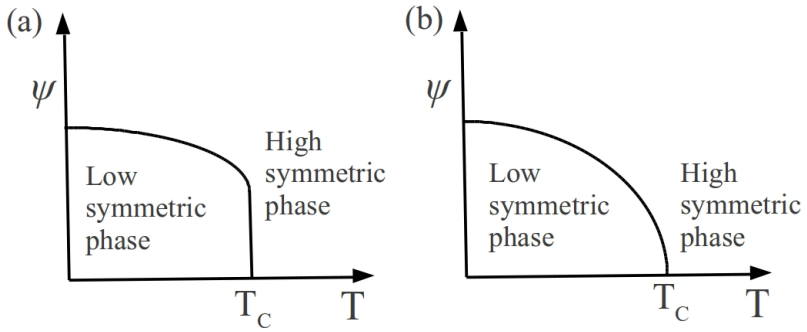

Figure 1.5: Order parameter as a function of temperature: (a) first order and (b) second order phase transitions.

In this thesis, we predict the behaviour of Néel transition and magnetic domain structures in hexagonal $YMnO_3$ and structural transitions in ferroelectric oxides

using effective Hamiltonian with parameters obtained from first-principles calculations.

1.4 Overview

The theme of this thesis induce determination of the couplings between several degrees of freedom (spin, charge, phonon and strain) using first-principles density functional theoretical calculations to explain experimentally observed phenomena, and to analyze the Néel and structural phase transitions by constructing effective Hamiltonian. We have chosen the materials that are fundamentally interesting as exhibiting unusual phenomena which involve fascinating physics.

In Chapter 2, we briefly describe first-principles methods used in this work, and discuss the basic aspects of Hohenberg-Kohn theorems and Kohn-Sham density functional theory.

In Chapter 3, we present our work uncovering the microscopic mechanisms of the experimentally observed "giant" magnetoelastic effect at Néel transition in hexagonal $YMnO_3$ using first-principles DFT calculations and effective Hamiltonian. The magnetic frustration and spin-orbit coupling give rise to a remarkable magneto-crystalline anisotropy and noncollinear ordering of magnetic moments of Mn^{3+} ions in $YMnO_3$, opening up a gap in the electronic spectrum with vanishing on-site electron correlations (Hubbard U=0). We analyze how the crystal field, magnetic exchange and the spin-orbit coupling influence the splitting and ordering of energy levels of d orbitals of Mn^{3+} ion in $YMnO_3$ that result in the observed magnitude of its local magnetic moment. We estimate the coupling of spins with phonon and strain, and show using Landau theory that a strong and anisotropic coupling of spin with Γ_1 phonons and strain constitute the microscopic mechanisms of giant magneto-elastic effect observed at Néel temperature. We present ab-initio statistical mechanical

analysis of Néel transition in $YMnO_3$ through Monte Carlo simulations of the model Hamiltonian constructed here to capture the physics of coupling between spins and phonons. Spins confine and order in the *ab*-plane with symmetry of the Γ_3 representation below T_N, and is accompanied by finite phonon mode amplitude (Γ_1 mode) as the secondary order parameter. Monte Carlo simulations of effective Hamiltonian with open and periodic boundary conditions highlight the specific initial states that facilitate formation of magnetic topological defects in the antiferromagnetic phase of $YMnO_3$. We observe that (a) the magnetic vortex and antivortex structures (topological defects) occur along the line defined by intersection of six magnetic domain walls, and (b) the magnetic domains get locked to the structural or ferroelectric domains.

In Chapter 4, we present analysis of the accuracy of SCAN metaGGA functional of the density functional theory to determine structural and electronic properties of ferroelectric (d^0) perovskite oxides. The parametrized effective Hamiltonian based on these calculations partly rectifies the errors in estimating ferroelectric transition temperatures in perovskites. We show that the recently developed strongly constrained and appropriately normed (SCAN) meta-GGA functional is quite accurate in estimating the lattice constants of perovskite oxides, i.e., $BaTiO_3$, $PbTiO_3$, $SrTiO_3$, $CaTiO_3$, $BaZrO_3$, $KNbO_3$, $NaNbO_3$ and $PbZrO_3$. The typical errors in the estimation of lattice constants of perovskite oxides obtained earlier within local density approximation (LDA) constitute one of the main sources of errors in prediction of their ferroelectric transition temperatures, which is partly resolved through the use of SCAN metaGGA functional. We determine ferroelectric ground state properties of eight oxides and transition temperatures of $BaTiO_3$, $PbTiO_3$ and $KNbO_3$ with effective Hamiltonian obtained using SCAN metaGGA functional. Molecular Dynamics simulations of effective Hamiltonian obtained from SCAN metaGGA based energy surface gives better estimation of ferroelectric transition temperatures

without having to use any negative pressure for compensation of the errors in lattice constant, e.g., in LDA. These improvements in estimation of the transition temperatures relative to LDA results are shown to arise from changes in the estimation of the strain-phonon coupling parameters and frequencies of the soft modes in the effective Hamiltonian. In addition, we have addressed the issues of errors in estimation of transition temperatures, which arise from the truncation of the subspace in construction of effective Hamiltonian. We quantify the lowest (fourth) order coupling between soft modes and higher-energy phonon modes, that influences the energy surfaces of the polar distortions. Finally, we demonstrate that the anharmonic coupling between soft mode and higher-energy modes renormalize the effective Hamiltonian to deeper double well energy functions associated with ferroelectric distortions, leading to further improvement in estimation of the ferroelectric transition temperatures.

In Chapter 5, we present analysis of the experimentally observed chemical instability of charge disproportionation in orthorhombic $LnRu_{1-\delta}O_3$ through first-principles DFT calculations. We predict the stoichiometric $LaRuO_3$ to be a half metallic ferromagnet in its ground state. The nature of this state is insensitive to on-site correlations included with Hubbard U term. In contrast, inclusion of Hubbard U (U=3.0 eV) in our analysis of $YRuO_3$ changes its metallic antiferromagnetic state to semiconducting state, and also gives a realistic magnetic moment of Ru atom close to its experimental value. In contrast to $LaRuO_3$, $YRuO_3$ is semiconducting in states with ferromagnetic and antiferromagnetic ordering. Introduction of cation vacancies induces a gap in the electronic spectrum in both lanthanide ruthenium oxides, consistent with experimental observations. Our calculations corroborate the simultaneous occurrence of Ru^{4+} (S=1, d^4) and Ru^{3+} ions (S=1/2, d^5) in $LaRu_{1-\delta}O_3$ ($YRu_{1-\delta}O_3$). Our estimate of the cohesive energy per one Ru vacancy in $LaRuO_3$ is quite small. This highlights the chemical instability in the

stoichiometric $LaRuO_3$, consistent with the properties observed in the experimental samples. We expect charge disproportionation to stabilize the system to a lower energy state. Comparatively larger energy cost of Ru vacancy in $YRuO_3$ is due to higher electronegativity of Y and stability of Ru^{3+} state reflected in its nonzero bandgap.

In Chapter 6, we present a possible mechanism of competing ordering relevant to the observed pseudogap in electronic structure (also linked with fluctuations of superconducting order parameter up to 40 K) of $Sr_{0.5}Ce_{0.5}FBiS_2$. From our work using first-principles theoretical analysis, we propose that the nesting of multi-band Fermi surface in its ferromagnetic state is the case for its electronic instability that competes with superconducting instability and suppresses the superconducting T_C. We identify the soft Raman active phonon mode involving eigen-displacements of Bi and S atoms, which couples strongly (λ=0.34) with electrons. The electrostatic interaction of a few ad-layers of Pd atoms with $Sr_{0.5}Ce_{0.5}FBiS_2$ modifies and weakens the nesting of Fermi surface. Effective weakening of the competing instability eventually increases its superconducting T_C (5 K) (through suppression of charge density wave-like instabilities). This provides a possible explanation for enhanced T_C upon Pd-tip interaction observed in experiment.

Finally, we summarize the thesis in Chapter 7 and present our outlook to the opportunities of further work.

Chapter 2

Methodology

Materials are composed of low energy electrons and nuclei, which determine their ground state and excited state properties. Many of the properties can be determined by calculating the first derivatives (e.g., stress, magnetization and forces are the first derivatives of energy with respect to strain, magnetic field and atomic displacements respectively) and second derivatives (e.g., interatomic force constants, elastic constants, magnetic and dielectric susceptibility are second derivatives of total energy with respect to atomic displacements, strain and magnetic and electric fields respectively) of total energy which is the sum of many-electron quantum ground state energy and classical electrostatic interaction energy between nuclei.

The main difficulty lies in determination of the quantum mechanical ground state of many-electron system. In 1965, Kohn *et. al.* [14, 30] developed a density functional theory, which maps an interacting electron system to a system of independent electrons within an effective potential. This leads to a method, which is approximate but computationally more efficient compared to the exact solutions of many electron system quantum Monte Carlo methods. Methods based on density functional theory are useful in prediction of various ground state properties of materials some of which might be hard to determine using experiments.

The total energy obtained within density functional theory (T=0 K) defines the energy surface as a function of variables in the phase space which can be used in statistical mechanical analysis of structural and magnetic transitions.

In this chapter, we review briefly the theoretical methods that have been employed to determine physical properties of materials. We present the formulation of density functional theory, and a mapping of many-body interacting system to independent particle system to determine the quantum mechanical ground state density of energy of materials. We describe various ab-initio methods that are used to calculate the total energy of system, and briefly discuss the frozen phonon and linear response methods used to calculate the vibrational spectra, dielectric constants and Born effective charges, etc.

2.1 Introduction

To find the quantum mechanical ground state, we start with a Hamiltonian of a system of interacting electrons and nuclei in the following general form:

$$\begin{aligned}\hat{H} = &-\frac{\hbar^2}{2m_e}\sum_{i=1}^{N}\nabla_i^2 - \sum_{i=1}^{N}\sum_{I=1}^{P}\frac{Z_I e^2}{|\mathbf{r}_i - \mathbf{R}_I|} + \frac{1}{2}\sum_{i=1}^{N}\sum_{j\neq i}^{N}\frac{e^2}{|\mathbf{r}_i - \mathbf{r}_j|} \\ &- \frac{\hbar^2}{2M_I}\sum_{i=1}^{N}\nabla_I^2 + \frac{1}{2}\sum_{I=1}^{P}\sum_{J\neq I}^{P}\frac{Z_I Z_J e^2}{|\mathbf{R}_I - \mathbf{R}_J|},\end{aligned} \tag{2.1}$$

where $\mathbf{r}$={r_i, i=1,....,N} and $\mathbf{R}$={R_I, I=1,....,P} are the sets of electronic and nuclear (ionic) position coordinates, $\hbar$ is the Planck's constant, Z_I and M_I are the atomic number and mass of I^{th} ion, m_e and e are the electronic mass and charge. The first and third terms in Equation 2.1 represent kinetic (T) and Coulomb interaction (V_{ee}) energies of electrons respectively, the fourth and fifth terms indicate ionic kinetic and coulomb interaction energies respectively. The Coulomb interaction energy between electrons and ions is included in the second term, which acts like an external

potential (V_{ext}) to the electronic system, and also includes the effects of external perturbations such as strain, electric and magnetic fields. As the nuclear mass (M_I) is significantly larger ($\frac{M_I}{m_e} \approx 1836$) than electronic mass, the kinetic energies of ions are small and can be ignored. This approximation is known as Born-Oppenheimer or adiabatic approximation [31]. Within this approximation, the motions of nuclei do not induce any electronic transition from one stationary quantum state to another. As electrons and nuclei are decoupled within the adiabatic approximation, the many body wavefunction can be written as a product of electronic and nuclear wavefunctions given as:

$$\Psi(\mathbf{R}, \mathbf{r}, t) = \sum_{n,n'} \phi_n(\mathbf{R}, t)\psi_{n'}(\mathbf{R}, \mathbf{r}). \tag{2.2}$$

$\psi_{n'}(\mathbf{R},\mathbf{r})$ are the electronic wavefunctions, which depend on the nuclear or ionic positions $\mathbf{R}$. $\phi_n(\mathbf{R})$ are nuclear wavefunctions but are independent of electronic positions $\mathbf{r}$. Electronic many-body wavefunctions are determined by the solution of time independent Schrödinger equation:

$$\hat{H}\Psi(\mathbf{R}, \mathbf{r}) = \epsilon\Psi(\mathbf{R}, \mathbf{r}). \tag{2.3}$$

Substituting Eq. 2.1 and Eq. 2.2 in Eq. 2.3 we get

$$\left[-\frac{\hbar^2}{2m_e}\sum_i \nabla_i^2 - \sum_{i,I}\frac{Z_I e^2}{|\mathbf{r}_i - \mathbf{R}_I|} + \frac{1}{2}\sum_{i\neq j}\frac{e^2}{|\mathbf{r}_i - \mathbf{r}_j|} + \frac{1}{2}\sum_{I\neq J}\frac{Z_I Z_J e^2}{|\mathbf{R}_I - \mathbf{R}_J|}\right]\psi_n(\mathbf{R}, \mathbf{r}) = E_n(\mathbf{R})\psi_n(\mathbf{R}, \mathbf{r}) \tag{2.4}$$

and

$$\left[-\frac{\hbar^2}{2M_I}\sum_{I=1}^{P}\nabla_I^2 + E_n(\mathbf{R})\right]\phi_n(\mathbf{R}) = \epsilon_n\phi_n(\mathbf{R}). \tag{2.5}$$

The ground state or the lowest energy state ψ_0(r) is determined by finding the minimum of total energy (Eq. 2.6) with respect to all the parameters defining ψ(r).

$$E_{tot}[\psi] = \frac{\left\langle \psi \left| \hat{H}_e \right| \psi \right\rangle}{\langle \psi \mid \psi \rangle}, \text{ where} \qquad \hat{H}_e = \hat{T} + \hat{V}_{ee} + \hat{V}_{ext}. \tag{2.6}$$

Electronic wavefunctions have to be antisymmetric as electrons are Fermions. While Born-Oppenheimer approximation partially resolves the difficulty in determining the quantum mechanical ground state for a given set of atomic positions (R_I), ψ_i is still a function of $3N$ number of variables (N=number of electrons) and hence determination of the ground state still remains quite hard and requires additional approximations.

2.2 Density Functional Theory

Density functional theory was developed to tackle the problem of correlated many body systems. The ground-breaking work of Hohenberg-Kohn in 1964 [30] and Kohn-Sham in 1965 [14] marked the development of density functional theory which became effective in treating electrons in atoms, molecules and condensed matter.

2.2.1 Hohenberg-Kohn theorems

Hohenberg and Kohn demonstrated a new approach to determine the ground state of an electron gas in an external potential (Eq. 2.6) [30]:

Theorem I: *The ground state electron density $n_0(\boldsymbol{r})$ uniquely determines the external potential except for a trivial constant. All ground state properties of a system can be determined if $n_0(\boldsymbol{r})$ is known.*

Theorem II: *The universal energy functional $E[n]$ can be defined in terms of*

density $n(\boldsymbol{r})$ which is valid for any external potential $V_{ext}(\boldsymbol{r})$. For a particular V_{ext}, the ground state energy is the global minimum of energy functional, and the density $n(\boldsymbol{r})$ that minimizes the energy functional is the exact ground state (wavefunction) energy density $n_0(\boldsymbol{r})$.

These two theorems reduce the number of variables of a function from 3N (in equation 2.4) to 3 (in n(**r**)). As the total energy is a function of ground state electron density, the theory is known as density functional theory. The total energy functional is given by,

$$\begin{aligned} E_{HK}[n] =& T[n] + E_{ee}[n] + \int d\mathbf{r} V_{ext}(\mathbf{r}) n(\mathbf{r}) + E_{ion-ion} \\ =& F_{HK}[n] + \int d\mathbf{r} V_{ext}(\mathbf{r}) n(\mathbf{r}) + E_{ion-ion}. \end{aligned} \tag{2.7}$$

$T[n]$ and $E_{ee}[n]$ are the kinetic and potential energies of interacting electron system. E_{II} represents the coulomb interaction energy of nuclei.

These theorems do not provide a practical scheme for determining the ground state electron density or energy of an interacting electron system. Kohn and Sham in 1965 proposed a method for determining ground state electron density $n_0(\mathbf{r})$.

2.2.2 Kohn-Sham ansatz

In the Kohn-Sham formalism [14], an interacting many-body system is mapped onto a fictitious non-interacting system but with same ground state density. The ground state density of spin polarized (σ=↑ and ↓) electrons can be written as:

$$n(\mathbf{r}) = \sum_{\sigma} n(\mathbf{r}, \sigma) = \sum_{\sigma} \sum_{i=1}^{N^{\sigma}} \psi_i^{\sigma *}(\mathbf{r}) \psi_i^{\sigma}(\mathbf{r}), \tag{2.8}$$

where $N = N^{\uparrow} + N^{\downarrow}$ is total number of electrons (sum of spin-up and spin-down electrons) and $\psi_i^{\sigma}(\mathbf{r})$ are the single electron wavefunctions.

The total energy functional in the Kohn-Sham formalism is written as,

$$\begin{aligned} E_{KS}[n] =& T_s[n] + \frac{e^2}{2}\int d\mathbf{r}d\mathbf{r}'\frac{n(\mathbf{r})n(\mathbf{r}')}{|\mathbf{r}-\mathbf{r}'|} + \int d\mathbf{r}V_{ext}(\mathbf{r})n(\mathbf{r}) + E_{XC}[n] + E_{ion-ion} \\ =& T_s[n] + E_{Hartree}[n] + \int d\mathbf{r}V_{ext}(\mathbf{r})n(\mathbf{r}) + E_{XC}[n] + E_{ion-ion}. \end{aligned} \tag{2.9}$$

T_s is the kinetic energy of single electron (non-interacting system). $E_{Hartree}$ and E_{XC} are the Hartree and exchange-correlation energy of electrons.

The Kohn-Sham non-interacting single particle Hamiltonian is,

$$\begin{aligned} H^{\sigma}_{KS} &= -\frac{\hbar^2}{2m_e}\nabla^2 + V^{\sigma}_{KS}(\mathbf{r}), \text{ where} \\ V^{\sigma}_{KS}(\mathbf{r}) &= V_{Hartree}(\mathbf{r}) + V_{ext}(\mathbf{r}) + V_{XC}[n(\mathbf{r})], \end{aligned} \tag{2.10}$$

where V_H and V_{XC} are functional derivatives of E_H and E_{XC} with respect to n(r).

Kohn-Sham (Schrödinger-like) equations are given by,

$$H^{\sigma}_{KS}\ \psi^{\sigma}_i = \epsilon^{\sigma}_i\ \psi^{\sigma}_i. \tag{2.11}$$

The Kohn-Sham equation can be solved iteratively to self-consistency as illustrated in Figure 2.1.

Within the relativistic treatment of electrons, we should use Dirac equation instead of Schrödinger equation. From the Dirac equation, a relativistic density functional theory is developed [32]. The Dirac-like single particle Kohn-Sham equation is given by,

$$H_e\psi_\nu(r) = (c\alpha.\mathbf{p} + \beta m_e c^2 + V_{KS})\psi_\nu(r) = E_\nu\psi_\nu(r). \tag{2.12}$$

$\mathbf{p}$ is the momentum operator, and c is the velocity of light. $E_\nu(=\epsilon_\nu + mc^2)$ is the sum of the Kohn-Sham eigenvalue and rest mass energy. V_{KS} represent the Kohn-Sham

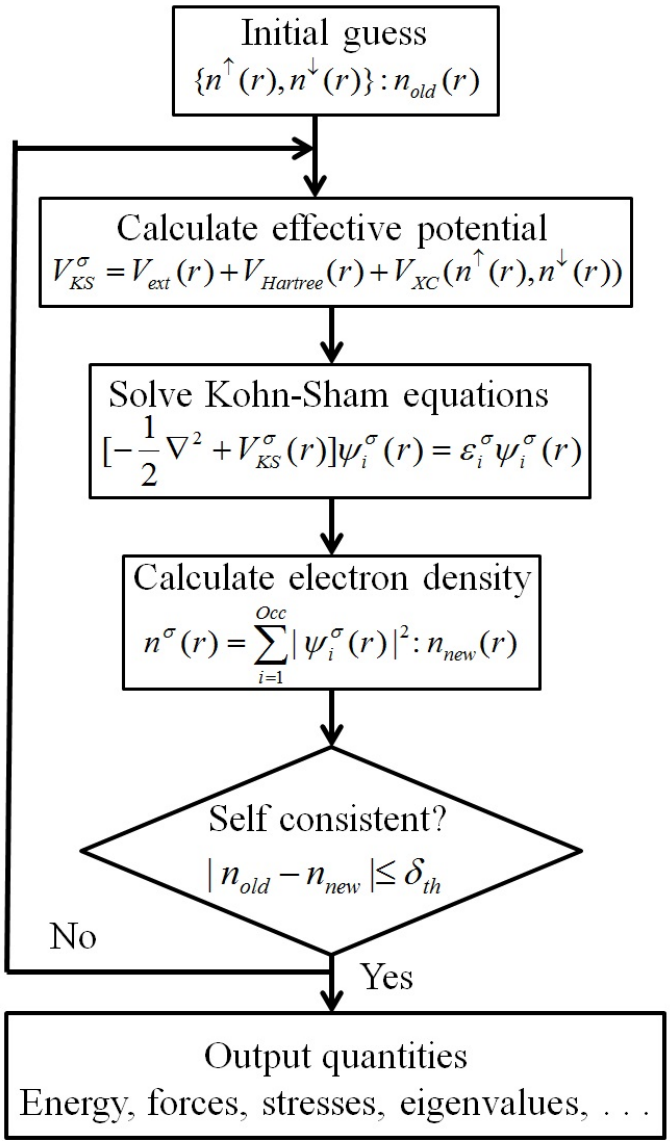

Figure 2.1: Iterative scheme used to solve the Kohn-Sham equations self-consistently.

potential. α and β are 4×4 Dirac matrices:

$$\alpha = \begin{pmatrix} 0 & \sigma_i \\ \sigma_i & 0 \end{pmatrix}, \beta = \begin{pmatrix} \mathbf{I} & 0 \\ 0 & \mathbf{I} \end{pmatrix}. \tag{2.13}$$

σ_i's are the (2×2) Pauli spin matrices, $\mathbf{I}$ is the 2×2 identity matrix. ψ_ν is a four

component spinor,

$$\psi_\nu(r) = \begin{pmatrix} \varphi_\nu^\uparrow(r) \\ \varphi_\nu^\downarrow(r) \\ \chi_\nu^\uparrow(r) \\ \chi_\nu^\downarrow(r) \end{pmatrix}. \tag{2.14}$$

φ_ν and χ_ν represent the large and small components of the wavefunction respectively. The Hamiltonian in Eq. 2.12 has the contributions of spin-orbit coupling and other relativistic terms (mass-velocity and Darwin).

2.2.3 Exchange-correlation functionals

Exchange-correlation energy (E_{XC}) includes all the many body effects such as exchange and correlation between electrons and their kinetic energies, expressed as:

$$E_{XC}[n] = T[n] - T_s[n] + E_{ee}[n] - E_{Hartree}. \tag{2.15}$$

E_{XC} is the difference between energies of true interacting system (kinetic and internal interaction energies) and fictitious non-interacting system (electron-electron interaction is replaced by Hartree energy). Its exact form is not known, and is typically approximated as a local or non-local functional of electron density. The well known approximations are discussed below.

Electrons in a solid can be approximated as a locally homogeneous electron gas. In this approximation, the effects of exchange and correlation are local, and exchange-correlation energy density at each point is the same function of density as that of a homogeneous electron gas. In local density approximation (LDA) or local spin density approximation (LSDA) [33], the exchange-correlation energy functional is written as,

$$E_{XC}^{LSDA}[n^\uparrow, n^\downarrow] = \int d\mathbf{r} n(\mathbf{r}) \epsilon_{XC}^{hom}(n^\uparrow(\mathbf{r}), n^\downarrow(\mathbf{r})), \tag{2.16}$$

where ϵ_{XC}^{hom} is the exchange-correlation energy per electron of a homogeneous electron gas of density $n_0 = n(\mathbf{r})$. An additional orbital dependent term U (for on-site correlations as given by Hubbard U term) is considered with LSDA to tackle highly localized atomic-like orbitals in correlated systems.

Spin quantization axis can vary in space for electronic systems with non-collinear spin as

compared to the collinear-spin system, where the spin quantization axis is fixed. The charge density matrix can be written as

$$n^{\alpha\beta}(\mathbf{r}) = \sum_{\sigma} \sum_{i=1}^{N} \psi_i^{\alpha *}(\mathbf{r}) \psi_i^{\beta}(\mathbf{r}), \tag{2.17}$$

where ψ^{α}(r) is a two component spinor (α=1,2). Kohn-Sham Hamiltonian here is a 2×2 matrix, given by,

$$H_{KS}^{\alpha\beta} = -\frac{\hbar^2}{2m_e}\nabla^2 + V_{KS}^{\alpha\beta}(\mathbf{r}). \tag{2.18}$$

The exchange-correlation potential ($V_{XC}^{\alpha\beta}$) has off-diagonal terms (Eq. 2.18) in α and β (as opposed to diagonal one for the collinear-spin case, LSDA). However, a local approximation can be made by finding the local axis of spin quantization and using the same functional form $\epsilon_{XC}^{hom}(n^{\uparrow}, n^{\downarrow})$. The non-collinear spin density matrix is expressed as,

$$m(\mathbf{r}) = \sum_{\alpha\beta} \sigma^{\alpha\beta} n^{\alpha\beta}(\mathbf{r}). \tag{2.19}$$

LSDA (LDA) works very well for homogeneous as well as for inhomogeneous electronic systems, but it fails when density changes very abruptly (e.g., molecules). A generalized gradient approximation (GGA) [34] overcomes the limitations of LSDA by considering the dependence of ϵ_{XC} on charge density as well as its gradient and is expressed as:

$$E_{XC}^{GGA}(n^{\uparrow}, n^{\downarrow}) = \int d\mathbf{r} n(\mathbf{r}) \epsilon_{XC}(n^{\uparrow}(\mathbf{r}), n^{\downarrow}(\mathbf{r}), \nabla n^{\uparrow}, \nabla n^{\downarrow}) \tag{2.20}$$

This leads to some improvement over LDA results by achieving higher accuracy in energies close to correlated wavefunction methods. The next step of approximation beyond GGA is the meta generalised gradient approximation (metaGGA) which includes dependence of ϵ_{XC} an kinetic energy density (semi-local) and can handle slowly varying as well as rapidly varying charge densities [35, 36]. Within the metaGGA approximation the exchange-correlation functional is:

$$\begin{aligned} E_{XC}^{MGGA}(n^{\uparrow}, n^{\downarrow}) &= \int d\mathbf{r} n(\mathbf{r}) \epsilon_{XC}(n^{\uparrow}(\mathbf{r}), n^{\downarrow}(\mathbf{r}), \nabla n^{\uparrow}, \nabla n^{\downarrow}, \tau^{\uparrow}, \tau^{\downarrow}), \text{ where} \\ \tau^{\sigma} &= \frac{1}{2} \sum_{i}^{Occ} |\nabla \psi_{i,\sigma}|^2 . \end{aligned} \tag{2.21}$$

τ^σ represents Kohn-Sham kinetic energy density of electrons (with spin σ). A metaGGA functional includes effects of shell structure on exchange-correlation energy through τ^σ, which LDA and GGA do not include. In contrast to LDA and GGA, metaGGA functionals recognize different types of chemical bonding in a way similar to electron localization function which also depends on τ^σ. As an example, the recently developed SCAN (strongly constrained and appropriately normed) metaGGA functional identifies various types of chemical bonds through a dimensionless parameter α (function of τ^σ): (a) covalent (α=0), (b) metallic (α=1) and (c) weak ($\alpha >> 1$) bonds [37–40]. Secondly, SCAN metaGGA functional satisfies 17 exact constraints (six for exchange, six for correlation and another five for the sum of the two), and is appropriately normed on the systems for which semilocal functional can be exact or nearly exact [37–40]. SCAN metaGGA functional accurately predicts the properties of diversely bonded materials and molecules (including covalent, metallic, ionic, hydrogen and van der Waal bonds) [37–40]. For example, SCAN metaGGA functional yields structures and relative energies of various phases of water clusters, ice and Si (semiconducting diamond and metallic β-Sn phases) with an accuracy comparable to that of coupled cluster (for water clusters) and expensive diffusion Monte Carlo (for ice and Si) predictions [37,38]. In addition, structures and band gaps of ferroelectric and multiferroic oxides are more accurately estimated using SCAN metaGGA functional (closer to their experimental values) compared to LDA and GGA [37, 38].

2.2.4 Basis sets

In a DFT calculation, basis set is used to expand the Kohn-Sham wavefunctions. In this thesis, we used plane wave basis and linearized augmented plane wave (LAPW) basis. These methods are quite accurate provided they are applied carefully, and converged with respect to size of basis set.

Plane wave basis is extensively used for its simplicity and absence of Pulay forces. They form a natural basis for description of valence electrons in sp-bonded metals and semiconductors. The Kohn-Sham wavefunction in the plane wave basis is expanded as follows:

$$\psi_{\mathbf{k},i}(\mathbf{r}) = \sum_{|\mathbf{G}|<G_{cut}} C_{i,(\mathbf{k}+\mathbf{G})} e^{i.(\mathbf{k}+\mathbf{G})\cdot\mathbf{r}}. \tag{2.22}$$

G are the reciprocal lattice vectors and **k** is the Bloch wavevector of the Kohn-Sham wavefunction in a crystal [41, 42], belonging to the Brillouin zone. The truncation of the set of **G** vectors is achieved using a kinetic energy cutoff. We choose these reciprocal vectors, which satisfy the condition:

$$\frac{\hbar^2}{2m_e}|\mathbf{k}+\mathbf{G}|^2 \leq E_{cut} = \frac{\hbar^2 G_{cut}^2}{2m_e}. \tag{2.23}$$

The calculated total energy is converged by increasing the energy cutoff (E_{cut}).

On the other hand, in LAPW method [43], a system is divided into two parts: (a) non-overlapping atomic spheres centered at atomic sites, called Muffin-Tins (MT) and (b) the interstitial region. Muffin-tin radius should be chosen carefully such that the atomic spheres do not overlap with each other. Different basis sets are used in these regions: (a) Inside the atomic sphere with radius R_{MT} (Muffin-tin radius), a wavefunction is expressed as a linear combination radial functions times spherical harmonics (Y_{lm}).

$$\phi_G(k,r) = \sum_{lm} [A_{lm} u_l(r, E_l) + B_{lm} \dot{u}_l(r, E_l)] Y_{lm}(r). \tag{2.24}$$

$u_l(r, E_l)$ is the regular solution of the radial part of Schrödinger equation with energy E_l, and $\dot{u}_l$(r,E$_l$) is the energy derivative of $u_l(r, E_l)$ calculated at E_l. A_{lm} and B_{lm} are functions of blochvector **k** and are determined from the boundary conditions

(boundary of two regions) of u_l and $\dot{u}_l$.

(b) In the interstitial region, plane wave basis is used.

$$\phi_G(k,r) = C_{(\mathbf{k}+\mathbf{G})} e^{i(\mathbf{k}+\mathbf{G})\cdot\mathbf{r}}. \tag{2.25}$$

Each plane wave is augmented by an atomic-like wavefunction inside the atomic sphere.

In the LAPW method, the Kohn-Sham wavefunction is expanded as linear combination of ϕ_G:

$$\psi(r) = \sum_G C_G \phi_G(k,r), \tag{2.26}$$

and the coefficients (C_G) are determined using Raleigh-Ritz variational principle. The convergence of this basis set is controlled by a cutoff parameter $R_{MT}\,G_{max}$, R_{MT} being the muffin-tin radius of the smallest atomic sphere, and G_{max} is the largest G vector. Thus, it allows an accurate description of both rapidly varying wavefunctions near nuclei as well as smoother part of it in the interstitial region.

2.2.5 Full potential linearly augmented plane wave (FLAPW) method

Kohn-Sham equations can be solved for all-electrons using the FLAPW method (all-electron method) that combines the LAPW basis sets (as discussed in previous section) with the treatment of full potential, i.e., without any shape approximations in the interstitial and Muffin-Tin regions. The general form of the potential here is given as:

$$V(r) = \begin{cases} \sum_{\mathbf{lm}} V_{lm}^{MT}(r) Y_{lm} & : r \le R_{MT} \\ \sum_G V_G^I e^{iGr} & : r > R_{MT} \end{cases} \tag{2.27}$$

Inside the Muffin-Tin sphere, the potential includes spherical as well as non-spherical terms. This method is different from LAPW and LMTO methods which considers constant potential in the interstitial region and spherical potential inside the Muffin-Tin sphere.

2.2.6 Pseudopotentials

Pseudopotential is another approximation necessary for DFT calculations based on plane wave basis. There are three types of electrons in an atom based on their chemical activity. Core electrons do not take part in chemical bonding and have highly localized wavefunctions. Their contributions to total binding energy of a molecule or crystal are negligible. Valence and semi-core electrons are not tightly bound to nuclei and actively take part in chemical bonding.

As the wavefunctions of core electrons are highly localized in the vicinity of nucleus, valence electrons wavefunctions have to vary rapidly inside the core region to satisfy the orthogonality conditions. Large kinetic energy of valence electrons associated with such rapid oscillations of wavefunctions inside the core region cancel approximately the potential energy arising from deep Coulomb potential.

The strong Coulomb potential, high kinetic energy of valence electrons and potential of electrons in the core region are replaced by a much weaker effective pseudopotential. Thus, it reduces the number of electrons as well as the demand on basis sets to represent the valence wavefunctions. The rapidly varying valence electronic wavefunctions inside the core region are replaced by a smoothly varying functions (see Figure 2.2). Pseudopotentials are constructed by defining a cutoff radius (r_c). Outside this cutoff radius, all the electron and pseudo wavefunctions are identical. The scattering properties and eigenvalues of a pseudopotential are the same as those of the atomic core. If the all-electron and pseudo wavefunctions generate same charge density in the regions $r \leq r_c$ (and also $r \geq r_c$ due to normalization),

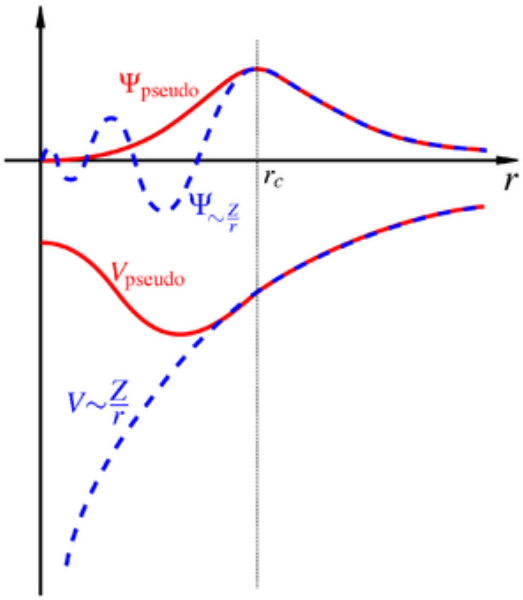

Figure 2.2: Schematic representation of all-electron wavefunction in the Coulomb potential (dotted line) in comparison with pseudo wavefunction in pseudopotential (solid line). Real and pseudopotentials and their corresponding wavefunctions match above the cutoff radius (r_c).

then the pseudopotential is norm conserving [44]. Ultrasoft pseudopotential includes an augmented charge inside the core region to conserve the total charge [45] while making the potential softer. The benefit of ultrasoft pseudopotential over normconserving pseudopotential is that it is computationally more efficient, and maintains the accuracy and transferability.

2.2.7 Frozen phonon method

Phonon is a quantum of energy associated with a normal mode of atomic (ionic) vibration in a crystal. Within Born-Oppenheimer approximation, electrons remain in their ground state and total energy is only a function of ionic positions ($\mathbf{R}_I$). The adiabatic motion of ions is governed by this Born-Oppenheimer surface ($E(\mathbf{R}_I)$). The amplitude of atomic vibration is typically small compared to the interatomic distance. The position of the I^{th} atom is $\mathbf{R}_I = \mathbf{R} + \mathbf{u}_I$, $\mathbf{u}_I$ is vibrating displacement

of the I^{th} atom from its equilibrium position ($\mathbf{R}$).

The potential energy is expressed as a Taylor expansion in $\mathbf{u}$:

$$V = V_0 + \sum_{I,\alpha} \frac{\partial E}{\partial R_{I,\alpha}} \mid_{u=0} u_{I\alpha} + \frac{1}{2} \sum_{I,J,\alpha,\beta} \frac{\partial^2 E}{\partial \mathbf{R}_{I,\alpha} \partial \mathbf{R}_{J,\beta}} \mid_{u=0} u_{I\alpha} u_{J\beta} + O(u^3). \quad (2.28)$$

At the equilibrium atomic positions, forces acting on the atoms are zero, and hence the second term of Equation 2.28 is zero. Ignoring the terms V_0 and $O(u^3)$, force constant matrix $K_{IJ,\alpha\beta}$ from the quadratic term in $\mathbf{u}$ is given by,

$$\begin{aligned} V &= \frac{1}{2} \sum_{I,J} \sum_{\alpha,\beta} \frac{\partial^2 E}{\partial \mathbf{R}_{I,\alpha} \partial \mathbf{R}_{J,\beta}} \mid_{u=0} u_{I\alpha} u_{J\beta} \\ &= \frac{1}{2} \sum_{I,J} \sum_{\alpha,\beta} K_{I\alpha,J\beta} u_{I\alpha} u_{J\beta}. \end{aligned} \quad (2.29)$$

Solving the equation of motion of these harmonic oscillators, we get,

$$M_I \frac{\partial^2 u_{I\alpha}}{\partial t^2} = - \sum_{J,\beta} K_{I\alpha,J\beta} u_{J\beta}. \quad (2.30)$$

Assuming the time dependence of $u_{I\alpha}$ to be,

$$\mathbf{u}_I(t) = u_I e^{i\omega t}, \quad (2.31)$$

equation 2.30 reduces to,

$$\omega^2 M_I u_{I\alpha} = \sum_{J,\beta} K_{I\alpha,J\beta} u_{J\beta}. \quad (2.32)$$

We can get phonon frequencies (ω: eigenvalue) and eigenvectors (u) by solving the above eigenvalue equation. For the atomic system, the force constant matrix is $(3N \times 3N)$ dimensional and there will be 3 normal mode frequencies. Phonon frequencies determine the thermal stability of the structure. When $\omega^2 > 0$ (stable

system), the excitation of any phonon mode with frequency ω increases the energy of the system. In an unstable system ($\omega^2 < 0$), a finite amplitude of unstable phonon mode results in lowering of the total energy of the structure.

In the frozen phonon method, we calculate total energy and forces (within the framework of density functional theory) by displacing the atoms by small amount ($\pm$d). The force constant matrix is obtained with:

$$K_{I\alpha,J\beta} \approx -\frac{\Delta F_{I,\alpha}}{\Delta \mathbf{R}_{J,\beta}} \approx -\frac{\Delta F_{I,\alpha}}{2\ d}, \tag{2.33}$$

where d is the amplitude of atomic displacement that is frozen in each direction. We can determine phonons at $q \neq 0$ using frozen phonon method by considering supercells (commensurate with the q-vector) and obtain the full phonon dispersion. Thus, it is computationally expensive and time consuming to calculate phonons at $q \neq 0$ with frozen phonon method. Density functional perturbation theory overcomes this drawback of frozen phonon method.

2.2.8 Density functional perturbation theory

Density functional perturbation theory is a linear response theory used to calculate response functions (physical property such as phonons, force, stress, dielectric constant and Born effective charges) as the second derivatives of total energy with respect to external perturbation (λ_i). The first and second derivatives of energy are,

$$\begin{aligned} \frac{\partial E}{\partial \lambda_i} =& \frac{\partial E_{ion-ion}}{\partial \lambda_i} + \int d\mathbf{r} \frac{\partial V_{ext}(\mathbf{r})}{\partial \lambda_i} n(\mathbf{r}), \\ \frac{\partial^2 E}{\partial \lambda_i \lambda_j} =& \frac{\partial^2 E_{ion-ion}}{\partial \lambda_i \lambda_j} + \int d\mathbf{r} \frac{\partial^2 V_{ext}(\mathbf{r})}{\partial \lambda_i \partial \lambda_j} n(\mathbf{r}) + \int d\mathbf{r} \frac{\partial n(\mathbf{r})}{\partial \lambda_i} \frac{\partial V_{ext}(\mathbf{r})}{\partial \lambda_j}. \end{aligned} \tag{2.34}$$

The first-order change in electron density with respect to λ_i is determined by linearizing equation 2.8 as

$$\Delta n(\mathbf{r}) = 2Re \sum_{i=1}^{N_e/2} \psi_i^*(\mathbf{r}) \Delta\psi_i(\mathbf{r}). \tag{2.35}$$

The variation in Kohn-Sham wavefunctions can be evaluated by solving first-order perturbation theory:

$$(H_{KS} - \epsilon_i)|\Delta\psi_i\rangle = -(\Delta V_{KS} - \Delta\epsilon_i)|\psi_i\rangle. \tag{2.36}$$

$\Delta\epsilon_i$ ($= \langle\psi_i|\Delta V_{KS}|\psi_i\rangle$) is the first-order variation in Kohn-Sham eigenvalues. The change in Kohn-Sham effective potential (ΔV_{KS}) is given as:

$$\Delta V_{KS}(\mathbf{r}) = \Delta V_{ext}(\mathbf{r}) + e^2 \int d\mathbf{r}' \frac{\Delta n(\mathbf{r}')}{|\mathbf{r} - \mathbf{r}'|} + \int d\mathbf{r}' \frac{\partial^2 V_{XC}(\mathbf{r})}{\partial n(\mathbf{r}) \partial n(\mathbf{r}')} \Delta n(\mathbf{r}'). \tag{2.37}$$

The response of electron density to external perturbation depends on the coupling between occupied and empty electronic states, and $\Delta\psi_i$ is projected onto empty states manifold (of gapped systems) and given by,

$$(H_{KS} - \epsilon_i)|\Delta\psi_i\rangle = -\hat{P}_{empty}\ \Delta V_{KS}|\psi_i\rangle, \tag{2.38}$$

where $\hat{P}_{empty}$ is the projection onto the empty states manifold and is defined as,

$$\hat{P}_{empty} = 1 - \hat{P}_{occ};\ \hat{P}_{occ} = \sum_{i=1}^{N_e} |\psi_i\rangle\langle\psi_i|. \tag{2.39}$$

From the solution of (Eq. 2.38) this set of linear equations, the response properties of a system can be obtained accurately and efficiently.

$K_{I\alpha,J\beta}$ can be evaluated using DFPT by calculating the second derivative of

total energy with respect to atomic displacements. Born effective charges (Z^*) can be estimated using DFPT as the mixed derivative of total energy with respect to electric field and atomic displacements. The dielectric constant (ϵ^∞) can be determined from the second derivative of total energy with respect to the electric field.

As the responses to phonon perturbations with different wavelengths are decoupled, linear perturbation theory is beneficial over the non-perturbative approaches like frozen phonon methods, and the calculation of phonon frequencies at arbitrary q-vectors can be performed using DFPT without introducing supercells.

2.3 Limitations of density functional theory

The estimation of physical properties within the approximations of density functional theory (DFT) suffers from the errors which originate from the violations of conditions of the exact energy functional. Some of the major failures in DFT calculations are underestimation of band gaps of materials and energy barriers of chemical reactions, and overestimation of binding energies of charge transfer complexes and the response to the electric field in materials [46]. They inaccurately estimate structural parameters of materials. DFT also fails to predict the insulating ground state of correlated systems such as transition metal oxides. These common issues are known to arise from the delocalization and static correlation errors of approximate functionals [46]. The delocalization error originates from the dominating Coulomb term which forces electrons to be far apart. On the other hand, static correlation error of approximate functionals arises due to the difficulty in using charge density to describe the interaction between the degenerate spin-up and spin-down states [46]. The development in constructing new functionals can be achieved by identifying and minimizing these errors and it will open a new route for the applications of DFT.

Chapter 3

Hexagonal $YMnO_3$: spin-phonon coupling, spin-orbit coupling and magnetic domain structures *

3.1 Introduction

At the microscopic level, spin-phonon coupling results in modulation of the magnetic exchange coupling arising from a structural change [48], and manifests itself in the consequent change in the energy gap of spin wave spectrum. Spin-phonon coupling is relevant to several phenomena exhibited by solids such as superconductivity, magneto-electric effects in multiferroics, magnetic semiconductors and charge transport. In a double perovskite La_2NiMnO_6, frequencies of polar phonons have been shown to be sensitive to anti-parallel or parallel arrangement of spins of neighboring transition metal atoms, which are responsible for its observed magnetocapacitance [49]. A piezo-magnetic effect viz., the change in the magnitude of magnetic

*A part of this work has been published in Physical Review B and reprinted with permission from [47]. Copyright (2015) by the American Physical Society, URL: https://doi.org/10.1103/PhysRevB.92.054106.

moment with change in volume, as well as the spin-phonon coupling have been observed in Raman spectroscopic analysis of iron based superconductors [50, 51]. The lowest frequency polar phonon of cubic $SrMnO_3$ was shown to soften anomalously below its antiferromagnetic transition temperature as a result of strong spin-phonon coupling [52]. The spin dependence of dielectric response has been observed in $EuTiO_3$ due to the coupling of lowest frequency IR active phonon with spins [53]. Spin-phonon coupling can be useful in developing new functionality in materials, as shown in stabilization of a desired magnetic order with epitaxial strain and generating a magneto-elastic effect through change in the direction of magnetic easy axis in $LaMnO_3$ [54].

Spin-phonon coupling is fundamentally interesting, and has been investigated extensively in cubic perovskite oxides [48–52, 55, 56], particularly in multiferroics. First-principles density functional theoretical calculations have been very effective in quantitatively understanding the spin-phonon coupling, as they allow (a) identification of the phonon modes that couple strongly with spin, (b) systematic quantification of the coupling at various orders, and (c) determination of mechanism in terms of structure and exchange interactions that cause spin-phonon coupling. However, first-principles studies [48, 49, 52, 55] of the spin-phonon coupling have so far not included the effects of spin-orbit coupling (SOC) which is a natural coupling between lattice and spin, and hence, a natural mechanism responsible for magneto-crystalline anisotropy [57].

Application of an electric field often lowers the crystal field symmetry surrounding the magnetic ions and hence changes the magnetic easy axis arising from SOC, resulting in a contribution of the SOC to magneto-electric effect [58]. This is indeed how the magneto-electric coupling arises from the antisymmetric Dzyaloshinskii-Moriya interaction driven by the SOC, which stabilizes a noncollinear magnetic ordering [59]. Thus, SOC is a common contributor to both magneto-elastic and

magneto-electric effects [4, 60].

Hexagonal multiferroics are ideal choice of materials to explore the interesting physics of SOC in the context of spin-phonon coupling. Hexagonal manganites ($RMnO_3$) are improper ferroelectrics [61], whose high symmetry paraelectric phase ($P6_3/mmc$) undergoes a structural transition at fairly high temperatures through trimerization of MnO_5 polyhedra alongwith shift of R^{3+} and equatorial oxygen ions along **c** axis due to a structural instability at the zone-boundary point K [61,62]. A spontaneous electric polarization emerges from a nonlinear coupling between trimerization (K_3) and zone-centre polar (Γ_2^-) modes [61,62]. Due to the nearest neighbor antiferromagnetic exchange interaction and hexagonal lattice in the ***ab*** plane, they are magnetically frustrated and have a high degeneracy of the magnetic ground states [63]. Spin frustration parameters for hexagonal manganites are close to 10 ($|\theta_{\mathrm{CW}}|/T_N$, where θ_{CW} and T_N are Curie-Weiss (CW) and Néel temperatures respectively) [64]. Magnetic frustration releases through coupling of spins with lattice degrees of freedom, facilitating the stabilization of a specific magnetic ground state below T_N [65]. It has been observed experimentally that magnetic ground states of hexagonal manganites are achieved through relatively large atomic displacements corresponding to the Γ_1 phonon mode resulting in changes in lattice and internal structural parameters - termed as the giant magneto-elastic effect [66]. Inelastic neutron scattering experiments have uncovered a notable magneto-crystalline anisotropy [63] in the spin-wave spectra of hexagonal manganites. As the SOC is quite relevant to the physics of magneto-crystalline anisotropy, magneto-elastic and magneto-electric effects in hexagonal manganites, the goal of the present work is to analyze their microscopic origin in $YMnO_3$ with a particular focus on SOC.

$YMnO_3$, a member of the family of hexagonal multiferroics [67], exhibits a spontaneous ferroelectric polarization of about 6.5 $\mu C/cm^2$ below the ferroelectric and structural transition temperature of 1270 K [68,69]. Structural domains or different

trimerized states in hexagonal $YMnO_3$ arise below T_C (1270 K) as a result of condensation of the trimerization mode K_3 [62,70]. Six different structural and ferroelectric domains merge at one point and form topological defect, which has been observed in conducting force and transmission electron microscopy experiments [71,72]. The change of sign of polarization at boundaries of structural domains in topological defect state is an outcome of the coupling between lattice distortion and polarization (improper ferroelectricity) [62].

On the other hand, antiferromagnetic ordering in $YMnO_3$ sets in at much lower temperature (T_N = 75 K) with no reduction in the structural symmetry ($P6_3cm$) [66]. The magnetic susceptibility and specific heat exhibit divergence near the isostructural antiferromagnetic transition temperature T_N [67]. Neutron diffraction measurements and optical second harmonic spectroscopy [73, 74] showed that the magnetic moments of Mn^{3+} ion are confined in the ***ab*** plane according to Γ_3 magnetic representation below T_N. This has been verified using Hartree-Fock calulations [75]. The spin-phonon coupling in $YMnO_3$, as evident in the inelastic neutron scattering experiments, [76] also manifests itself in an anomalous variation of Raman spectra at T_N [77]. At present, the precise nature and microscopic origin of the spin-phonon coupling are not quite clear.

Antiferromagnetic ordering in the ***ab*** plane below T_N is not coupled with the direction of macroscopic ferroelectric polarization (arises below T_C) as the coupling is forbidden by symmetry. In recent non-linear optical experiments, it has been surprisingly observed that ferroelectric domain walls are locked to the magnetic domain walls [78]. This non-trivial magneto-electric coupling is believed to originate from the modification of spin interactions at the ferroelectric domain walls [79, 80]. Free magnetic domain walls not associated with ferroelectric domain walls are also observed in experiments [78]. However, the correlation between antiferromagnetic, structural and ferroelectric orderings below T_N is not properly understood.

First-principles calculations and Landau theory have been used effectively in understanding improper ferroelectricity [69,70] and magnetic and structural domains [62] in hexagonal $YMnO_3$. Determination of phonons of $YMnO_3$ from first-principles [69, 81] are based on collinear antiferromagnetic ordering in which an insulating ground state is achieved using a local spin dependent functional approximation of density functional theory, but using a rather large Hubbard U parameter of 8 eV [82] for on-site correlations. With this choice, the $3d$ states of Mn^{3+} occur at energies lower than that of the $2p$ states of O, while calculations with triangular antiferromagnetic order and those including the SOC give an insulating state with $U = 0$ with the $3d$ states of Mn occurring slightly higher than the valence band of $2p$ orbitals of oxygen [83].

In this chapter, we determine the electronic structure and energetics of several noncollinear antiferromagnetic phases of $YMnO_3$ using first-principles calculations based on density functional theory (DFT) that include the SOC. We find an insulating magnetic ground state of Γ_3 symmetry even in the absence of any on-site correlation modeled with Hubbard U parameter, in agreement with results of Ref. [83]. Building on this, we analyze the role of SOC in splitting d levels near the gap, and understand the electronic structure relevant to the magnetic ordering in $YMnO_3$. We determine the nature of spin-phonon coupling and estimate it quantitatively, and discuss its implications to the observed giant anisotropic magneto-elastic effect just below T_N. We predict the behaviour of Néel transition and magnetic domain structures in $YMnO_3$ by constructing a model Hamiltonian derived from first-principles calculations. We describe methods of first-principles calculations in section 3.2, structural details and noncollinearly ordered magnetic states considered here in section 3.3. In section 3.4.1 and 3.4.2, we discuss about energetics, electronic structures and phonon spectra of noncollinear magnetic and nonmagnetic states. We analyze the anomaly in Born effective charges of atoms in the magnetic

ground state in section 3.4.3 and determine the origin and order of spin-phonon coupling in $YMnO_3$ using Landau theory in section 3.4.4. In section 3.4.5.1, we determine the temperature dependence of order parameters relevant to Néel transition by using a model Hamiltonian. We discuss about magnetic domain structures and coupling between structural, antiferromagnetic and ferroelectric order parameters below Néel temperature in section 3.4.5.2, and finally conclude in Section 3.5.

3.2 Methods

We use fully relativistic pseudopotentials [84] to represent the interactions between the ionic cores and valence electrons and include the effects of SOC. Valence electrons wave functions are represented in the two component spinor form in relativistic calculations. The spin dependent exchange-correlation energy is treated within a local density approximation with Perdew-Zunger parametrized form of the energy functional [85] as implemented in QUANTUM ESPRESSO [86]. We consider various configurations with noncollinear magnetic ordering of spins as well as a nonmagnetic ($S = 0,\ d^4$) state of $YMnO_3$ in simulations. We use an energy cutoff of 30 Ry to truncate the plane wave basis used to represent wave functions, and 240 Ry in representation of charge density. Brillouin zone integrations of ferroelectric and antiferromagnetic hexagonal unit cell (containing 30 atoms) are sampled on $5 \times 5 \times 3$ mesh of k-points. We determine dynamical matrix and phonons at Γ point using a frozen phonon method with atomic displacements of $\pm$ 0.04 Å in each Cartesian direction. We compute 90 zone-centre phonon modes from the eigenspectrum of dynamical matrix, obtained from Hellmann-Feynman forces acting on atoms in each of the q_0 distorted configuration. Born effective charges are obtained by displacing atoms about 0.04 Å along the three Cartesian direction and calculating resulting difference in polarization using Berry phase method [87].

We perform classical Monte Carlo simulations to study Néel transition by using our developed model Hamiltonian. For simulations, we consider the hexagonal lattice formed only by Mn atoms ($P6_3cm$ phase below T_N) and ignore other atomic sites. The direction of Heisenberg spin at ith Mn site is defined by ($\theta_i \in [0, \pi]$, $\phi_i \in [0, 2\pi]$) and it is updated by randomly choosing ($\delta\theta_i$, $\delta\phi_i$). The new direction of spin ($\theta_i + \delta\theta_i$, $\phi_i + \delta\phi_i$) is accepted by following the standard Metropolis algorithm. We consider a supercell of system size 10×10×10 (6,000 spins) and ±2 K temperature step for heating-up and cooling-down simulations with periodic boundary conditions. We use 60,000 Monte Carlo steps for thermalization and another 70,000 Monte Carlo steps for averaging properties of the system at each temperature. We choose random spin configuration as the initial state in cooling-down simulations. Magnetic ordering in the ***ab*** plane according to Γ_3 symmetry is chosen as the initial state in heating-up simulations. To visualize magnetic domain structures, we consider 16×16×16 (24,576 spins) and 60×60×8 (1,72,800 spins) supercells.

3.3 Symmetry of crystal structure and magnetic ordering

The unit cell of hexagonal crystal of $YMnO_3$ contains six formula units, i.e. 30 atoms, in the low temperature antiferromagnetic and ferroelectric phase. Mn^{3+} ions are surrounded by three equatorial oxygen ions (two O3 and one O4) and two apical oxygen ions (O1 and O2) forming a triangular bipyramidal coordination geometry as shown in Figure 3.1. These MnO_5 bipyramids are linked together with the corner sharing equatorial oxygen ions (O3 and O4). The Mn^{3+} ions in the ***ab*** plane form a triangular lattice. The two planes of Mn^{3+} ions along the ***c*** axis are linked through apical oxygen ions weakly bridged by yttrium ions (Y1 and Y2). We have used experimental lattice constants a = 6.12049 Å and c = 11.40756 Å

(see supplementary information of Ref. [66]) in our calculations of the magnetically ordered structures. It is known from the group theoretical analysis that ferroelectric

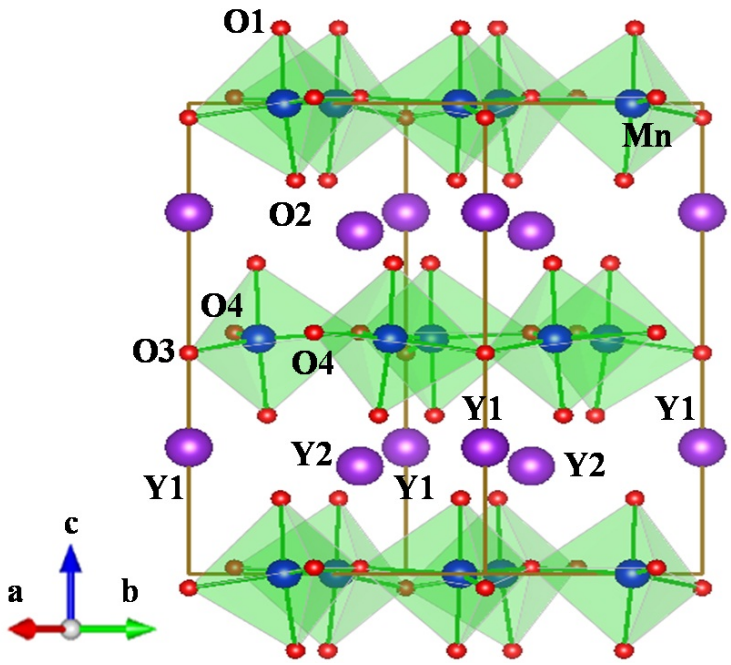

Figure 3.1: The crystal structure of $YMnO_3$ below Néel temperature. Copyright (2015) by the American Physical Society [47].

and paramagnetic phase of hexagonal $YMnO_3$ with space group $P6_3cm1'$ lowers its symmetry to magnetic space groups $P6_3cm$, $P6_3c'm'$, $P6'_3cm'$, $P6'_3c'm$ (prime sign is associated with the time reversal operation) by freezing magnetic moments according to four one dimensional magnetic representations Γ_1, Γ_2, Γ_3 and Γ_4 (Figure 3.2) at Γ point [67]. For Γ_1 and Γ_4 magnetic representations, spins have only component in the ***ab*** plane. On the other hand, Γ_2 and Γ_3 magnetic representations both have two magnetic basis vectors, one spin-polarized in the ***ab*** plane (Γ_2(I) and Γ_3(I)) and other with spins along ***c*** axis (Γ_2(II) and Γ_3(II)). For Γ_2(II) magnetic ordering all the spin moments ferromagnetically ordered along ***c*** axis whereas spin moments in the two different plane are antiferromagnetically coupled in the Γ_3(II) magnetic ordering. The magnetic moments of six Mn^{3+} ions in the ***ab*** plane for four one dimensional magnetic representations are either directed towards the crystallographic axes or

perpendicular to it. Six fold screw axis operation (6_{3z}) around $\boldsymbol{c}$ axis associated with time reversal operation is a symmetry respected by magnetic ordering of Γ_3 and Γ_4 representations not of Γ_1 and Γ_2 representations. The Γ_1 (Γ_2) and Γ_4 (Γ_3) magnetic representations differ by the ordering of magnetic moments at c=0 and c=1/2 planes.

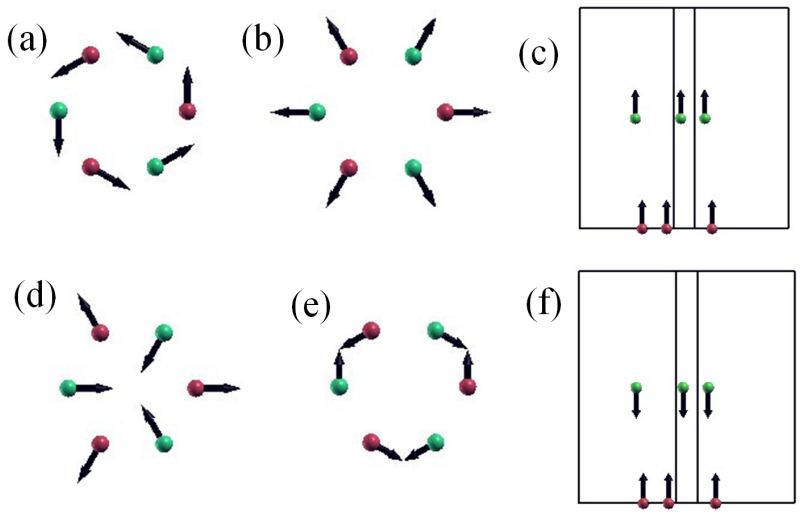

Figure 3.2: Schematic diagram of configurations of magnetic ordering corresponding to different irreducible representations: (a) Γ_1, (b) 1^{st} basis vector of Γ_2 (Γ_2(I) ordering), (c) 2^{nd} basis vector of Γ_2 (Γ_2(II) ordering), (d) 1^{st} basis vector of Γ_3 (Γ_3(I) ordering), (e) Γ_4 and (f) 2^{nd} basis vector of Γ_3 (Γ_3(II) ordering). Mn^{3+} ions at $c = 0$ and $c = 1/2$ planes are represented in red and green colors respectively. Copyright (2015) by the American Physical Society [47].

3.4 Results and discussions

3.4.1 Magnetic ground state and electronic origin of its stability

Among the five magnetically ordered states with Γ_1, Γ_2(I), Γ_3(I), Γ_3(II) and Γ_4 symmetry and a nonmagnetic (NM) state, our first-principles calculations show that the magnetic state with Γ_3 symmetry and magnetic moments lying in the basal

plane has the lowest energy (see TABLE 3.1), consistent with experimental [73, 74] as well as earlier theoretical results [75].

Table 3.1: Total energies of magnetic and nonmagnetic phases of $YMnO_3$ per unit cell with six formula unit relative to the ground state configuration $\Gamma_3(I)$. Copyright (2015) by the American Physical Society [47].

Magnetic representation	Energy (meV)
Γ_1	3.9
Γ_2	2.7
$\Gamma_3(I)$	0.0
Γ_4	1.4
$\Gamma_3(II)$	520
NM	3946

As expected for magnetically frustrated systems, the differences in energy of the magnetically ordered states with magnetic moments confined in the ***ab*** plane are quite small (approximately 1 meV per six formula unit). We checked convergence with finer $10 \times 10 \times 6$ mesh of k-points and these results are essentially unchanged. The magnetic state with Γ_3(II) ordering is significantly higher in energy (by 520 meV per six formula unit) relative to the ground state with Γ_3(I) ordering of $YMnO_3$. This large energy difference between the two magnetic states can be readily understood using a model Hamiltonian:

$$H = E_0 + J_p \sum_{\langle ij \rangle} \hat{s}_i.\hat{s}_j + J_{ip} \sum_{\langle ij \rangle} \hat{s}_i.\hat{s}_j + K_p \sum_i \sin^2 \theta_i + K_a \sum_i (\hat{r}_i.\hat{s}_i)^2. \qquad (3.1)$$

E_0 is the energy of the paramagnetic state ($P6_3cm1'$). J_p and J_{ip} are the nearest neighbour in-plane and inter-plane superexchange coupling parameters. K_p and K_a are the easy-plane and in-plane easy axis magneto-crystalline anisotropy originating from the spin-orbit coupling. $\hat{s}_i$ is the direction of spin at ith site, θ_i is the angle

between $\hat{s}_i$ and $\boldsymbol{c}$ axis and $\hat{r}_i$ is the in-plane projection of the position vector of ith Mn atom with respect to the centre ($\sum_{i=1}^{6} \hat{r}_i$=0). We determine values of the parameters (J_p=18 meV, J_{ip}=0.07 meV, K_p=-4 meV and K_a=-0.3 meV) in H_s by fitting to the energies of various magnetically ordered states considered here. The magnetic energies of Γ_3(I) and Γ_3(II) states per six Mn atom can be obtained using H_s:

$$H_s(\Gamma_3(I)) = E_0 - 9J_p + 6K_p + 6K_a. \tag{3.2}$$

$$H_s(\Gamma_3(II)) = E_0 + 18J_p - 18J_{ip}. \tag{3.3}$$

Energy difference ($27J_p$ - $18J_{ip}$ - $6(K_p + K_a)$) between the two magnetic states of Γ_3 symmetry arises mainly from the in-plane superexchange interaction and to some extent from the easy-plane magneto-crystalline anisotropy. The in-plane easy axis magneto-crystalline anisotropy and inter-plane superexchange coupling contribute weakly to this energy difference. At low temperature, the spin moments of Mn^{3+} ions are confined in the ***ab*** plane due to the presence of magneto-crystalline anisotropy. All the magnetically ordered states are more stable compared to NM state of $YMnO_3$.

Figure 3.3 represents the electronic structures of NM and low energy magnetically ordered states of $YMnO_3$. Significant contribution to the conduction band is from Mn $3d$ orbitals (J = 5/2, 3/2), while the valence band is contributed by Mn $3d$ (J = 5/2, 3/2) and O $2p$ (J = 3/2, 1/2) orbitals as shown in Figure 3.3a. However, We find a small contribution to the valence band in the energy range from -6 eV to -2 eV coming from Y $4d$ (J = 5/2, 3/2) orbitals due to its strong hybridization with O $2p$ orbitals. At the magnetically ordered states of $YMnO_3$ with magnetic moments in the ***ab*** plane are insulators with an indirect band gap of about 0.67 eV, underestimated compared to the experimentally measured band gap about 1.55

eV [88, 89]. In contrast, the magnetic state with Γ_3(II) ordering and NM state are metallic in nature. We note that LSDA+U (with a large Hubbard U parameter, U=8 eV) and self-interaction corrected LSDA calculation were done previously to get insulating collinear antiferromagnetic state of $YMnO_3$ with 3d states of Mn energetically lower than the valence band of 2p orbitals of O [70,82]. Our calculated band gap and electronic density of states with 3d states of Mn energetically higher than the valence band of 2p orbitals of O are in close agreement with the results obtained using GGA + SOC [83].

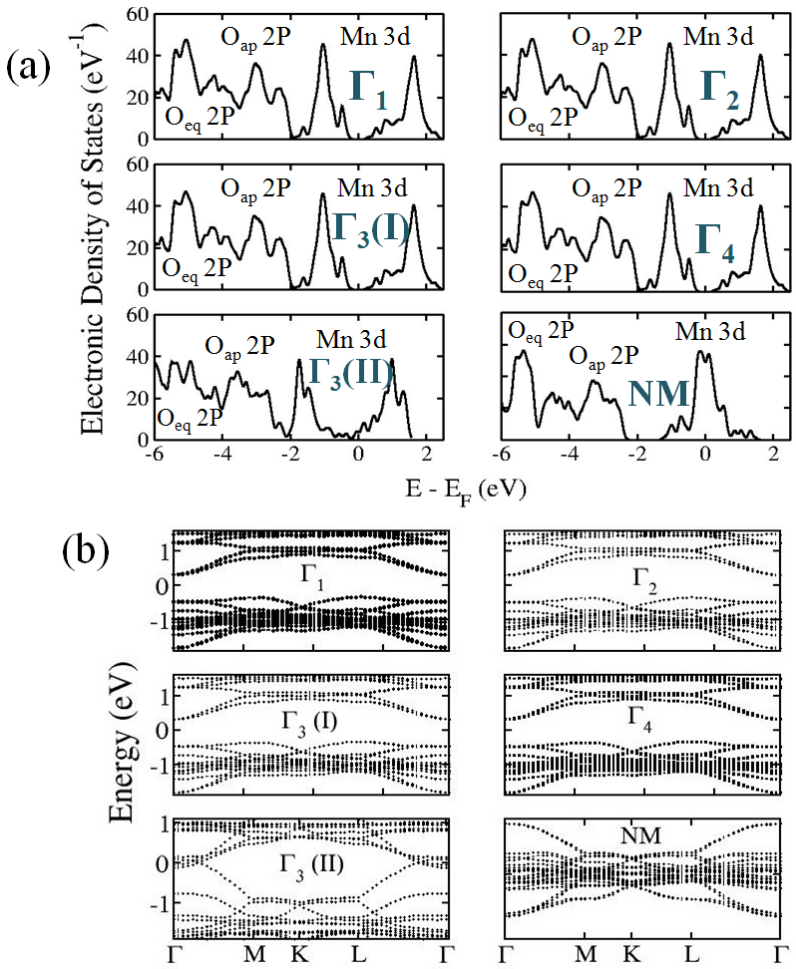

Figure 3.3: Electronic structure of noncollinearly ordered magnetic and NM states of $YMnO_3$: (a) electronic density of states (O_{eq} and O_{ap} are equatorial and apical oxygen ions respectively) and (b) band structure. Copyright (2015) by the American Physical Society [47].

As discussed earlier in this section, the NM state is energetically much higher than the magnetic states. In contrast to the noncollinearly ordered magnetic states, a high electronic density of states at the Fermi level for the NM state suggests a possible Stoner instability (see Figure 3.3a). Indeed, Mn $3d$ bands at the Fermi level of NM state split due the SOC and magnetic exchange coupling, giving the low energy magnetic structure. We now analyze the splitting of Mn $3d$ levels around the Fermi level, starting with five-fold degenerate d orbitals and introduce the effect of crystal field, SOC and magnetic exchange coupling on atomic energy levels (see Figure 3.4). In the trigonal bipyramidal crystal field, five-fold degenerate d orbitals split into two lowest lying doublets (b (=xz+iyz, m_L=1), b' (=xz-iyz, (m_L=-1)) and (a (=xy+i[x^2 - y^2], m_L=2), a' (=xy-i[x^2 - y^2], m_L=-2)) and a higher energy singlet z^2. These two lowest lying doublets are separated by Δ_{CF} amount of energy. The spin-orbit coupling term in Hamiltonian:

$$\hat{H}_{\mathrm{LS}} = \lambda \hat{L}.\hat{S} = \lambda(\hat{L}_+\hat{S}_- + \hat{L}_-\hat{S}_+ + \hat{L}_z\hat{S}_z), \tag{3.4}$$

where $\hat{L}$ and $\hat{S}$ are orbital and spin angular momentum operator, $\hat{L}_+$ ($\hat{S}_+$) and $\hat{L}_-$ ($\hat{S}_-$) are the corresponding raising and lowering operators, and λ is the strength of SOC. The spherical harmonics, Y_{Lm_L} (=a, a', b, b'), are the eigenfunctions of $\hat{L}_z$ operator. The eigenfunctions of SOC operator contain orbital part as well as spin part, and a suitable basis function is denoted as $|L, m_L, S, m_S\rangle$ [90].

$$\begin{aligned} E_{\mathrm{SOC}} &= \left\langle L, m_{L'}, S, m_{S'} \left| \hat{H}_{\mathrm{LS}} \right| L, m_L, S, m_S \right\rangle \\ &= \lambda[(m_L+1)(m_S-1)\delta_{m_{L'},m_L+1}\delta_{m_{S'},m_S-1} \\ &+ (m_L-1)(m_S+1)\delta_{m_{L'},m_L-1}\delta_{m_{S'},m_S+1} \\ &+ m_L m_S \delta_{m_{L'},m_L}\delta_{m_{S'},m_S}]. \end{aligned} \tag{3.5}$$

E_{SOC} is the spin-orbit coupling energy. For convenience, we present the basis functions in the form of $\left|Y_{Lm_L}, \uparrow (m_S = \frac{1}{2})\right\rangle$ and $\left|Y_{Lm_L}, \downarrow (m_S = -\frac{1}{2})\right\rangle$. The SOC splits the two sets of lowest degenerate energy levels (doublets).

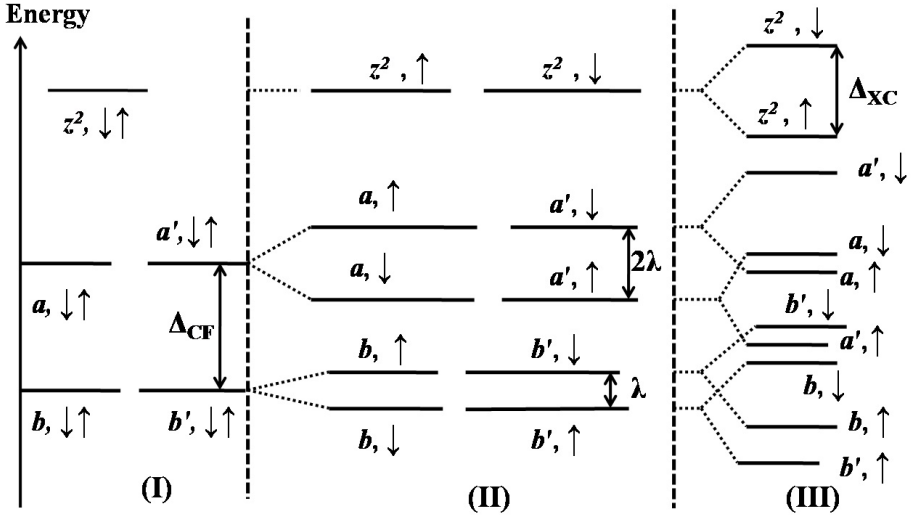

Figure 3.4: Schematic diagram of evolution of energies of $3d$ orbitals of Mn^{3+} ion: (I) effect of trigonal bipyramidal crystal field (Δ_{CF} is the energy difference between two lowest lying doublets), (II) effect of spin-orbit coupling (λ is the strength of spin-orbit coupling) and (III) effect of magnetic exchange splitting (Δ_{xc} is the energy difference between up and down spin levels coming from exchange splitting). The energy levels in the three sections are denoted by $(Y_{Lm_L}, \uparrow (m_S = \frac{1}{2}))$ and $(Y_{Lm_L}, \downarrow (m_S = -\frac{1}{2}))$ notation (a=$Y_{2,2}$=xy+$i[x^2$-$y^2]$, a'=$Y_{2,-2}$=xy-$i[x^2$-$y^2]$, b=$Y_{2,1}$=xz+iyz and b'=$Y_{2,-1}$=xz-iyz). Copyright (2015) by the American Physical Society [47].

The eigenfunctions of SOC operator in the subspace of (b (m_L=1), b' (m_L=-1), $\uparrow\downarrow$ ($m_S = \pm\frac{1}{2}$)) are $|b, \uparrow\rangle$ and $|b', \uparrow\rangle$, $|b, \downarrow\rangle$ and $|b', \downarrow\rangle$ with eigenvalues $\lambda/2$, -$\lambda/2$, -$\lambda/2$, $\lambda/2$ respectively (using Eq. 3.5). Similarly SOC splits the degenerate a (m_L=2) and a' (m_L=-2) energy levels into two doubly degenerate states $[|a, \uparrow\rangle, |a', \uparrow\rangle]$ and $[|a, \downarrow\rangle, |a', \downarrow\rangle]$, separated by 2λ amount of energy (see section (II) of Figure 3.4). The magnetic exchange interaction further splits the up and down spin states by Δ_{xc} amount of energy (see section (III) of Figure 3.4), where Δ_{xc} is the exchange coupling constant.

In the absence of SOC, the magnetic exchange coupling favors occupation of four d electrons in the two lowest lying degenerate up spin states ($|a, \uparrow\rangle$, $|a', \uparrow\rangle$,

$|b,\uparrow\rangle$ and $|b',\uparrow\rangle$) following the Hund's rule. The contribution to magnetic moment of each Mn^{3+} ion comes from spin part of angular momentum ($M_S = 2$) as M_L (M_L=$m_L(a)$+$m_L(a')$+$m_L(b)$+$m_L(b')$) is zero for the two lowest lying degenerate states. M_L=0 corresponds to $L \geqslant 0$ and M_S=2 ($m_S(a)$+$m_S(a')$+$m_S(b)$+$m_S(b')$) corresponds to $S \geqslant 2$. The value of J(=L+S) is 2. The value of magnetic moment for M_J=2 (g_J=2):

$$\mu_{J,z} = g_J M_J \mu_B = 4\mu_B. \tag{3.6}$$

However, experimentally measured (from neutron diffraction experiments) value of magnetic moment (defined by $g_J M_J \mu_B$) per Mn^{3+} ion is 3 μ_B which is much smaller than 4 μ_B [67]. Thus, magnetic exchange coupling alone can not explain the observed reduction in magnetic moment of each Mn^{3+} ion. The combined effect of both SOC and magnetic exchange coupling on crystal field split d levels causes crossing of energy levels (see section (III) in Figure 3.4). In this case, four d electrons occupy $|b',\uparrow\rangle$, $|b,\downarrow\rangle$, $|b,\uparrow\rangle$ and $|a',\uparrow\rangle$ states and give total M_L = -1 and $M_S = 1$. If $\lambda < 0$ and $\Delta_{XC} > 0$, then M_L becomes +1 and M_S becomes +1 ($|b',\uparrow\rangle$, $|b,\uparrow\rangle$, $|b',\downarrow\rangle$ and $|a,\uparrow\rangle$). If $\lambda > 0$ and $\Delta_{XC} < 0$, then M_L becomes -1 and M_S becomes -1 ($|b',\downarrow\rangle$, $|b,\downarrow\rangle$, $|b,\uparrow\rangle$ and $|a',\downarrow\rangle$). M_L=±1 gives $L \geqslant 1$ and M_S=±1 gives $S \geqslant 1$. The total angular momentum (J) is 2 for (L+S) and 0 for $|\ L - S\ |$. M_J=2 state is energetically favorable according to Hund's rule. The Landé g-factor [90] for $L = 1$ and $S = 1$ is $\frac{3}{2}$. The value of magnetic moment for $M_J = 2$ ($J = 2$),

$$\mu_{J,z} = g_J M_J \mu_B = 3\mu_B. \tag{3.7}$$

Since the NM state has S=0, there is no spin-orbit and magnetic exchange coupling effect (see Figure 3.3a).

Next, we investigate the electronic density of states (obtained from DFT calculation) projected on 3d orbitals of Mn atom to find the signature of the many-electron

state (M_J=2). The single-electron state (non-interacting system) associated with d level is defined as $|j, m_j\rangle$ when spin-orbit coupling is included in DFT calculation. The allowed values of j (in single-electron picture) are 3/2 (l-1/2, l=2) and 5/2 (l+1/2, l=2). The m_j projected density of states obtained using DFT+SOC calculation for the two values of j are given in Figure 3.5.

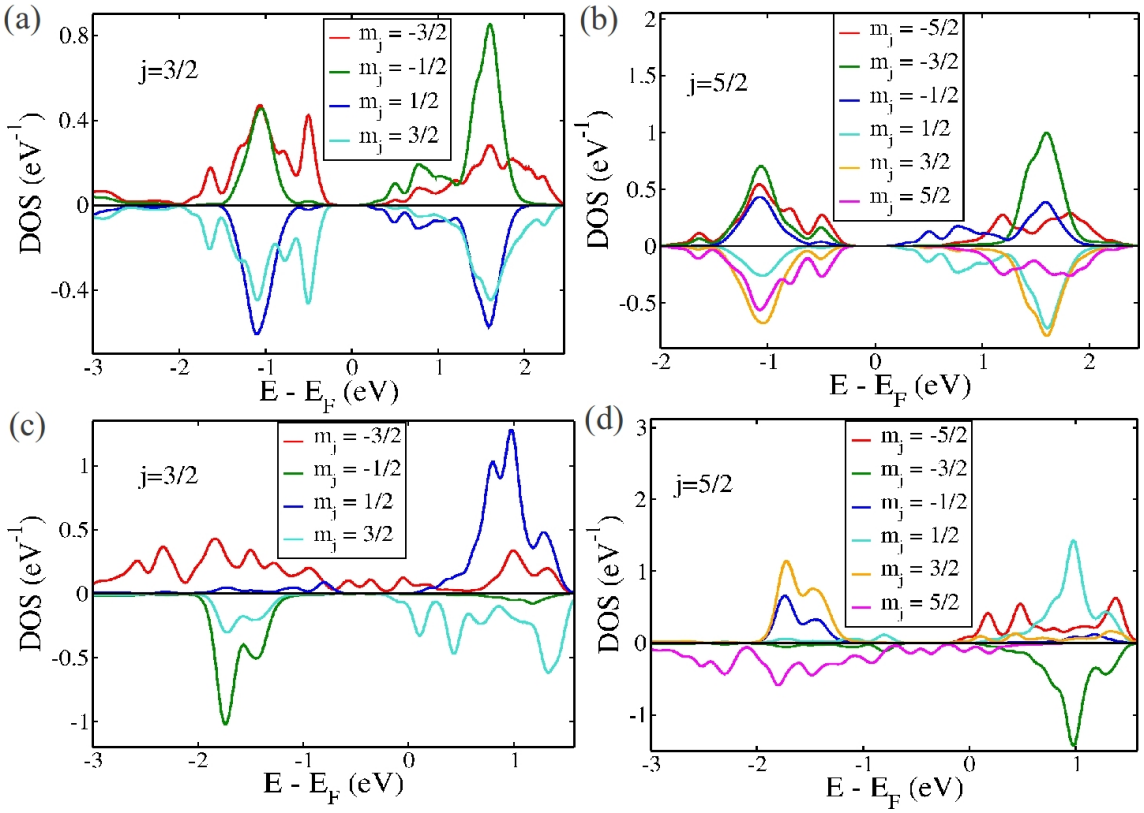

Figure 3.5: m_j projected density of states: (a) and (b) Γ_3(I) magnetic state (orderings of spins in the ***ab*** plane), (c) and (d) Γ_3(II) magnetic state (spins are along ***c*** axis).

We determine M_J from the m_j projected density of states by using the expression given as,

$$M_J = \sum_j m_j \int_{-\infty}^{0} \rho_{m_j}(E - E_F)dE. \tag{3.8}$$

The estimated value of M_J is 0.03 for Γ_3(I) magnetic state as the electronic density of states associated with +m$_j$ and -m$_j$ are almost identical (see Figure 3.5). For Γ_3(II) magnetic state, some of the electronic states ($|j, m_j\rangle$) are occupied and give

the value of M_J as 2.3. This highlights that the magnetic quantization axis is along the crystallographic ***c*** axis. As magnetic moments are confined in the ***ab*** plane for Γ_3(I) state, component of J along ***c*** axis is zero, i.e., M_J=0.03.

Next, we estimate the value of spin-only magnetic moment per Mn^{3+} ion ($\mu_{s,z}$= $g_S M_S \mu_B$, g_S=2) using DFT+SOC calculation as 3 μ_B (four d electron). To explain the origin of spin-only magnetic moment, we consider two possible spin states (as described earlier): S=1 ($\mu_{s,z}$=2 μ_B) and S=2 ($\mu_{s,z}$=4 μ_B). But, neither of the spin states give the magnetic moment as 3 μ_B. However, it appears that the admixture of these two states can give S=3/2 state ($\mu_{s,z}$=3 μ_B). On the other hand, hybridization between Mn 3d and O 2p states can also reduce the spin-only magnetic moment from 4 μ_B to 3 μ_B.

In the next subsection, we determine the spin-phonon coupling arising from SOC through determination of phonon spectra of hexagonal antifferomanetic $YMnO_3$ with different Γ_3 magnetic ordering.

3.4.2 Phonons

Using frozen phonon method, we determined zone-centre (Γ point) phonons of the NM state and magnetic states with Γ_3(I), Γ_3(II) and Γ_1 orderings. From the zone-centre phonon density of states (see Figure 3.6), it is clear that there are no significant differences in phonon spectra of the magnetic phases with magnetic moments confined in the ***ab*** plane. The peak at 600 cm^{-1} in the vibrational DOS of the magnetic state with Γ_3(I) ordering is split in case of the magnetic state with Γ_3(II) ordering. The presence of phonon modes at 180 cm^{-1} in the Γ_3(II) phase and 259 cm^{-1} in the Γ_3(I) phase differentiates the two phases with Γ_3 symmetry. On the other hand, the absence and presence of modes at 600 cm^{-1} and 39 cm^{-1} respectively in the NM state differentiates it from the magnetically ordered states. We have assigned a symmetry label to each phonon mode by calculating the overlap of its eigenvector

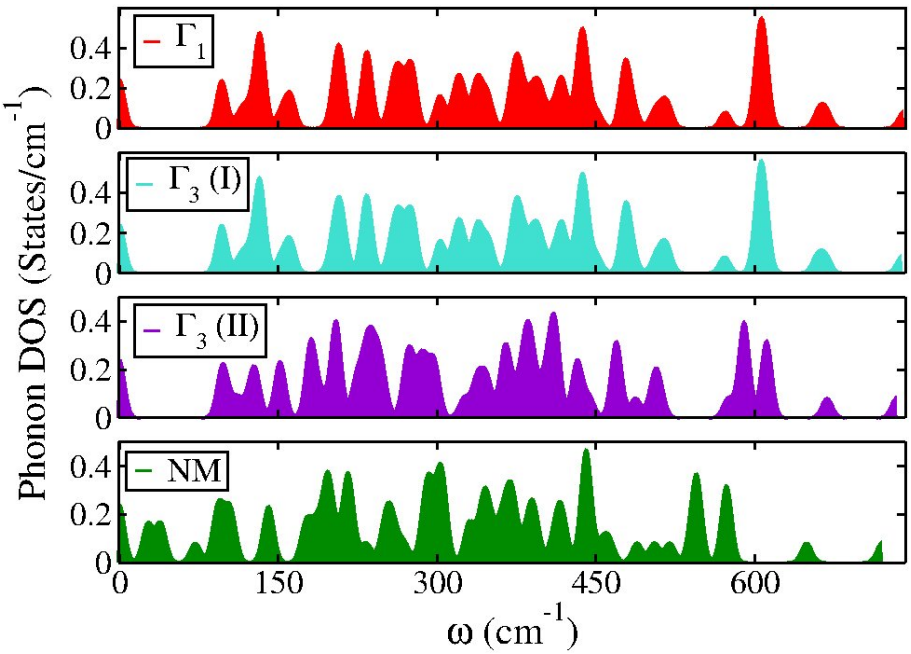

Figure 3.6: Phonon density of states at Γ point of noncollinearly ordered magnetic and nonmagnetic states of $YMnO_3$. Copyright (2015) by the American Physical Society [47].

with linear combinations of atomic displacements that form the basis vectors of different irreducible representations, obtained using ISOTROPY program [91]. There are 10 Γ_1, 5 Γ_4, 5 Γ_2, 10 Γ_3 and 30 Γ_6 and 30 Γ_5 symmetry modes in the magnetically ordered states as well as for NM state of $YMnO_3$. Out of the three acoustic modes at Γ point, two have Γ_6 symmetry and one has Γ_1 symmetry. Optical phonon modes with Γ_1, Γ_5 and Γ_6 symmetry are Raman active, whereas phonon modes having Γ_2, Γ_3 and Γ_4 symmetry are silent modes (neither Raman nor IR active) [92].

In TABLE 3.3, we present our results for frequencies of Raman active phonons at Γ point for magnetic and NM states of $YMnO_3$, and compare with phonon frequencies calculated using LSDA + U method [81] and experimentally observed Raman and IR active phonon modes below and above T_N [77, 92]. Our estimates of the frequencies of Raman active phonons of Γ_3(I) and Γ_1 magnetic states deviate from the observed Raman frequencies below T_N at most by 11 %. Since first-principles based DFT calculations do not include the effect of temperature, we consider this

Table 3.2: Phonon frequencies (in cm^{-1}) of silent modes at Γ point calculated from first-principles for magnetic and nonmagnetic phases of $YMnO_3$ in comparison to frequencies calculated using LSDA + U and B1-WC methods [81]. Copyright (2015) by the American Physical Society [47].

Symmetry	Γ_3(I)	Γ_1	Γ_3(II)	NM	LSDA + U [81]	B1-WC [81]
Γ_2	506	505	506	488	524	533
Γ_2	409	409	382	409	401	412
Γ_2	266	266	276	268	306	309
Γ_2	256	256	270	184	266	250
Γ_2	114	114	111	95	105	43
Γ_4	513	513	510	505	520	531
Γ_4	377	376	363	352	424	429
Γ_4	303	302	299	307	271	274
Γ_4	259	259	272	202	262	260
Γ_4	97	97	100	71	137	130
Γ_3	738	740	733	719	769	790
Γ_3	658	660	588	519	700	719
Γ_3	517	518	503	455	529	538
Γ_3	437	436	409	438	454	461
Γ_3	382	382	376	344	401	397
Γ_3	337	337	362	340	342	350
Γ_3	263	262	287	187	274	281
Γ_3	212	210	234	175	224	221
Γ_3	200	202	204	176	207	194
Γ_3	122	122	123	101	127	130

deviation of frequencies from experimentally determined values as acceptable. For silent modes with Γ_2, Γ_3 and Γ_4 symmetries (listed in TABLE 3.2), our results for their frequencies in the three magnetic states differ by about 9 % from the estimates obtained using LSDA + U and B1-WC methods [81].

Table 3.3: Raman active phonon frequencies (in cm^{-1}) calculated from first-principles for magnetic and nonmagnetic phases of $YMnO_3$ in comparison with frequencies calculated using LSDA + U and B1-WC methods [81] and experimentally observed Raman and IR (given in parenthesis) active modes below and above T_N [77, 92]. Copyright (2015) by the American Physical Society [47].

	Theory						Experiment	
Symmetry	Γ_3(I)	Γ_1	Γ_3(II)	NM	LSDA + U [81]	B1-WC [81]	15 K [77]	300 K [92]
Γ_1	666	667	668	648	691	707	686	681
Γ_1	571	571	574	540	593	583		(612)
Γ_1	484	485	487	463	498	513	466	459
Γ_1	450	451	443	440	460	472	435	433 (428)
Γ_1	419	418	386	440	428	421		(398)
Γ_1	302	302	325	420	313	317		297
Γ_1	264	263	279	294	272	287	264	257 (265)
Γ_1	236	236	249	233	252	233	210	190
Γ_1	152	152	149	138	170	130	160	148
Γ_5	607	608	610	573	643	651	647	
Γ_5	604	603	590	572	623	620		
Γ_5	477	477	470	441	490	474	483	
Γ_5	437	437	410	372	455	451	444	
Γ_5	433	433	402	362	440	432	406	
Γ_5	390	390	384	330	398	401	331	
Γ_5	371	371	346	303	376	368	307	
Γ_5	338	337	296	292	350	360	302	
Γ_5	323	323	285	257	314	301		
Γ_5	274	274	224	250	261	241		
Γ_5	208	208	204	196	243	209	225	$\sim$ 215
Γ_5	205	205	204	196	210	189		
Γ_5	133	133	180	106	184	168		135
Γ_5	132	133	152	92	145	122	141	
Γ_5	96	96	96	27	102	95		
Γ_6	602	603	589	545	622	619		(596)
Γ_6	609	609	611	545	644	653	638	632
Γ_6	477	477	468	441	489	494	509	(491)
Γ_6	439	439	433	415	459	443		
Γ_6	417	417	412	392	419	426	420	(457)
Γ_6	397	397	390	386	403	414		408
Γ_6	376	376	366	368	379	377	377	376
Γ_6	348	347	337	346	367	361	360	(308)
Γ_6	317	317	245	303	302	298		(281)
Γ_6	277	277	239	288	274	239		(238)
Γ_6	233	233	232	218	245	227	247	
Γ_6	232	232	234	214	211	192		211
Γ_6	161	161	181	141	183	161		
Γ_6	130	130	128	39	171	129		

3.4.3 Born effective charges

Born effective charge of an atom in a crystal (Z^*) is its force response to electric field or the polarization response to atomic displacement $u_{i,\beta}$, defined as [93]:

$$Z^*{}_{i,\alpha\beta} = \Omega_0 \frac{\partial F_{i\beta}}{\partial E_\alpha} = \Omega_0 \frac{\partial P_\alpha}{\partial u_{i,\beta}}. \tag{3.9}$$

Ω_0 is the volume of the unit cell. P_α is the polarization per unit cell in the direction α (=x, y, z) induced by the displacement of i^{th} atom in the direction β (=x, y, z). $F_{i\beta}$ is the β component of force acting on i^{th} atom due to the application of electric field (E) in the direction of α.

Table 3.4: Born effective charges of noncollinear antiferromagnetic phase with Γ_3(I) ordering of hexagonal $YMnO_3$ calculated from first-principles in comparison with the values calculated using self-interaction corrected LSDA method [70]. Copyright (2015) by the American Physical Society [47].

Atoms	Z^*_{xx}	Z^*_{yy}	Z^*_{zz}	Z^* [70]
Mn	3.26	3.31	3.87	3.3
Y1	3.53	3.53	4.21	3.6
Y2	3.58	3.58	4.15	
O1	-2.11	-2.07	-3.23	-2.3
O2	-2.07	-2.13	-3.41	
O3	-2.57	-2.57	-1.40	-2.2
O4	-2.63	-2.63	-1.34	

The nominal charges of Y, O and Mn in hexagonal $YMnO_3$ are +3, -2 and +3 respectively. We calculated Born effective charges of the magnetic ground state with Γ_3(I) symmetry. The zz components are anomalous for yttrium (Z^*_{zz}(Y1) = +4.21, Z^*_{zz}(Y2) = +4.15) and apical oxygen (Z^*_{zz}(O1) = -3.23, Z^*_{zz}(O2) = -3.41) as shown in TABLE 3.4, consistent with the values obtained from experimental results [94].

From the comparison of our results with Ref. [70], it appears that the SOC influences largely the zz component of Born effective charges but leaving the xx

and yy components close to the nominal values. The anomalous behavior of zz component is due to hybridization of Y $4d$ and O (apical oxygen) $2p$ orbitals (Y-O_{ap} bond lengths are smaller compared to Y-O_{eq} bond lengths as shown in TABLE 3.5) which has been observed in x-ray absorption spectroscopy [95]. Also, the drastic change in the electronic density of states projected onto $3d$ orbital of Mn atom near the Fermi level compared to the previous self-interaction corrected LSDA calculation [70] is notably reflected in the difference in two sets of calculated Born effective charges.

3.4.4 Spin-phonon coupling

A clear signature of nontrivial spin-phonon coupling is evident in our result that the structures of Γ_3(I) and Γ_3(II) magnetically ordered states differ as reflected in the changes in bond lengths and angles of the magnetic states of $YMnO_3$ (see TABLE 3.5). The difference in Y1-O3 and Y2-O4 bond lengths and Y1-O1-Mn bond angles of the two magnetically ordered state with Γ_3 symmetry is about 0.3 %.

To estimate the lowest order spin-phonon and magneto-structural coupling, we determine forces on atoms and stresses on the unit cell due to the change in magnetic ordering. We use a self consistent calculation with the magnetic ordering of Γ_3(II) representation, but at the relaxed structure of magnetic state with Γ_3(I) ordering. We find considerable Hellmann-Feynman forces (1-2 mRy/bohr) on yttrium (Y1, Y2) and apical oxygen (O1, O2) atoms and stresses (26 kbar) on the unit cell as compared to the (almost vanishing) forces and stresses on the relaxed structure of the magnetic state with Γ_3(I) ordering (see Figure 3.7a and Figure 3.7b). The magnetically induced forces on apical oxygen (O1, O2), Y1 and Y2 atoms are 2.13 mRy/bohr, 2.95 mRy/bohr and 1.46 mRy/bohr respectively, which have the symmetry of the basis vectors of Γ_1 irreducible representation (see Figures 3.7c, 3.7d

Table 3.5: Calculated bond lengths (in Å) and bond angles (in °) of several magnetic states of $YMnO_3$. Copyright (2015) by the American Physical Society [47].

Atoms	Γ_1	Γ_2	Γ_3(I)	Γ_4	Γ_3(II)
Mn - O1	1.88	1.88	1.88	1.88	1.88
Mn - O3	2.06	2.06	2.06	2.06	2.06
Y1 - O1	2.28	2.28	2.28	2.28	2.28
Y1 - O2	2.29	2.29	2.30	2.30	2.30
Y1 - O3	2.31	2.31	2.31	2.31	2.32
Y2 - O1	2.25	2.25	2.25	2.25	2.25
Y2 - O2	2.31	2.31	2.31	2.31	2.31
Y2 - O4	2.44	2.44	2.44	2.44	2.45
Mn - O3 - Mn	118.7	118.7	118.7	118.7	118.7
Mn - O4 - Mn	119.1	119.1	119.1	119.1	119.1
Y1 - O1 - Mn	129.1	129.2	129.2	129.1	128.8
Y2 - O2 - Mn	123.3	123.3	123.3	123.3	123.1

and 3.7e). Forces acting on yttrium and apical oxygen (O1 and O2) atoms are consistent with experimentally observed atomic displacements below Néel temperature according to the basis vectors of Γ_1 representation [66]. The changes in aa ($=bb$) components of stress (σ_{aa} and σ_{bb}) are about 26 kbar, while σ_{zz} remains unchanged. The spin-phonon coupling in the $\boldsymbol{ab}$ plane is more pronounced than that along the $\boldsymbol{c}$ axis, highlighting remarkable magneto-crystalline anisotropy. It has been observed experimentally that the components of elastic constant in the $\boldsymbol{ab}$ plane show unusual behavior near T_N [96].

To model the lowest order spin-phonon and magneto-structural coupling in the ferroelectric and antiferromagnetic phase, we write a Landau free energy as a function of atomic displacements (u) having Γ_1 symmetry, strain (e) of Γ_1 symmetry, magnetic ordering (A) of Γ_3(I) and (M) of Γ_3(II) symmetry. The antiferromagnetic

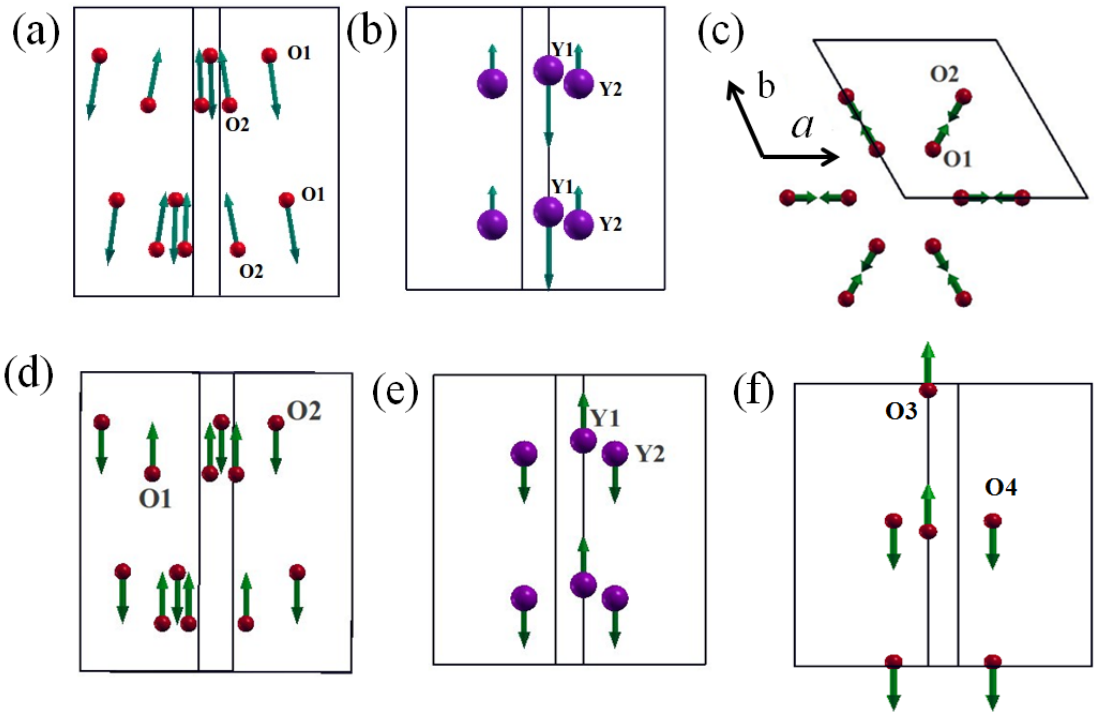

Figure 3.7: Due to the change of magnetic ordering from Γ_3(I) to Γ_3(II) forces (in the scale of mRy/bohr) acting on: (a) O1 and O2 atoms, (b) Y1 and Y2 atoms. Pictorial representation of independent atomic displacements with Γ_1 symmetry: (c) 1st basis vector, (d) 2nd basis vector for apical oxygen atoms (O1 and O2), (e) basis vector for yttrium atoms (Y1 and Y2) and (f) basis vector for equatorial oxygen atoms (O3 and O4). Copyright (2015) by the American Physical Society [47].

order parameters (A and M) are mathematically expressed as,

$$\begin{aligned} A &= \sum_{i=1}^{6} (-1)^i (\hat{r_i}.\hat{s_i}), \\ M &= \sum_{i=1}^{6} (-1)^i s_{i,z}, \end{aligned} \tag{3.10}$$

where $\hat{r_i}$ represents the in-plane projection of the position vector of ith Mn atom with respect to the centre ($\sum_{i=1}^{6} \hat{r_i}$=0, see Figure 3.14). $s_{i,z}$ is the z-component of $\hat{s_i}$ (spin vector of ith Mn^{3+} ion). The symmetry invariant form of free energy up to fourth order in u, e, A and M with reference to the ferroelectric-paramagnetic state

obtained using ISOTROPY [91]:

$$\begin{aligned} H(u,e,A,M,T) = H_0 &+ a_1(T-T_N)A^2 + a_2A^4 + b_1(T-T_{N_1})M^2 + b_2M^4 \\ &+ \frac{1}{2}ku^2 + dM^2u + cA^2u + \beta A^2u^2 + \gamma M^2u^2 + \frac{1}{2}Ce^2 \\ &+ c_1AM + c_2AMu + c_3A^2e + c_4M^2e + c_5AMe, \end{aligned} \tag{3.11}$$

where a_1, a_2, b_1, b_2, k, β, γ, d, c, C, c_1, c_2, c_3, c_4, c_5 are the temperature independent coefficients. H_0 is the energy of the reference ferroelectric-paramagnetic ($P6_3cm1'$) parent phase. c, d and c_2 represent third order (quadratic) spin-phonon coupling constant and β and γ denote fourth order (quadratic) spin-phonon coupling constant. T_N and T_{N_1} are the ordering temperatures of A and M respectively. c_3, c_4 and c_5 are the third-order (quadratic) magneto-structural coupling constant. The values of c_1, c_2 and c_5 are negligible due to very weak coupling between A and M order parameters in the low temperature phase.

At the relaxed structure of magnetic state with L ordering, forces on atoms:

$$F_u|_{u=u_{min},M=0} = -\frac{\partial H}{\partial u}|_{u=u_{min},M=0} = 0 \implies u_{min} \approx -\frac{c}{k}A^2. \tag{3.12}$$

Forces on the atoms and stresses on the unit cell due to the change in magnetic ordering from Γ_3(I) ($A \neq 0$, M=0) to Γ_3(II) ($M \neq 0$, A=0) at the relaxed structure of magnetic state with A ordering are given by,

$$F_u|_{u=u_{min},A=0} = -dM^2. \tag{3.13}$$

$$\sigma|_{e=0,A=0} = -\frac{\partial H}{\partial e}|_{e=0,A=0} = -c_4M^2. \tag{3.14}$$

Forces acting on atoms (-dM^2) and stresses on the unit cell (-c_4M^2) having Γ_1 symmetry arise from the third order spin-phonon and magneto-structural coupling,

given in Eq. 3.13 and Eq. 3.14 respectively, which are consistent with the experimentally observed atomic displacements according to Γ_1 representation and changes in lattice parameters below T_N [66]. For A type magnetic ordering the force is zero at the minimum energy whereas there are nonzero forces ($-dM^2$) acting on the atoms for M type magnetic ordering.

Next, we project the forces acting on the atoms due to the change in magnetic ordering from Γ_3(I) to Γ_3(II) on the phonon modes of magnetic state with Γ_3(I) ordering. Five optical zone-centre phonon modes (ω = 666 cm^{-1}, 484 cm^{-1}, 450 cm^{-1}, 236 cm^{-1} and 152 cm^{-1}) with Γ_1 symmetry (see Figure 3.8) show a strong overlap with the forces acting on atoms, given in TABLE 3.6.

Table 3.6: Coupling of force arising due to the change of magnetic ordering from Γ_3(I) to Γ_3(II) with the phonon modes of magnetic phase of $YMnO_3$ with Γ_3(I) ordering. Copyright (2015) by the American Physical Society [47].

Phonons with Γ_1 symmetry (ω in cm^{-1})	Spin-phonon coupling constant (mRy /bohr)
666	7.59
484	1.48
450	1.47
152	5.01
236	1.52

Thus, magnetic moments of Mn^{3+} couple strongly with the zone-centre phonon modes of Γ_1 symmetry with frequencies 666 cm^{-1} and 152 cm^{-1} at the third order (spin-phonon coupling in hexagonal $YMnO_3$ as shown by Eq. 3.13). In the temperature dependent Raman spectra, intensities of these two phonon modes involving displacement of yttrium and apical oxygen atoms increase drastically as the temperature reduces to T_N [77].

Below T_N, structure distorts through movement of atoms according to the Γ_1 phonon mode. The quasi-planar arrangement of equatorial oxygen and manganese ions of hexagonal $YMnO_3$ gives the major component of Dzyaloshinskii-Moriya (DM)

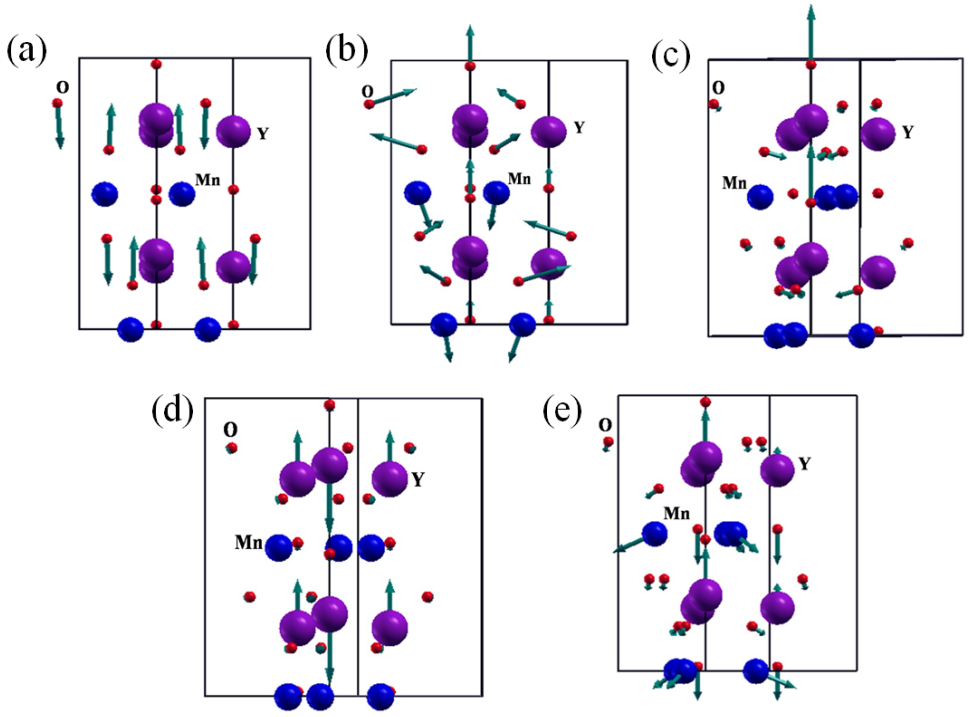

Figure 3.8: Visualization of the eigendisplacements of zone-centre phonon modes having Γ_1 symmetry of magnetic phases with Γ_3(I) ordering with frequencies: (a) 666 cm^{-1}, (b) 484 cm^{-1}, (c) 450 cm^{-1}, (d) 152 cm^{-1} and (e) 236 cm^{-1} show strong overlap with the forces acting on atoms which arises due to the change of magnetic ordering from Γ_3(I) to Γ_3(II). Copyright (2015) by the American Physical Society [47].

vector ($\propto \lambda \boldsymbol{x} \times r_{ij}$, λ is the strength of SOC, $\mathbf{r}_{ij}$ is the unit vector connecting i^{th} and j^{th} magnetic ions and $\boldsymbol{x}$ is the vector pointing towards oxygen ion from $\mathbf{r}_{ij}$ [4]) along $\boldsymbol{c}$ axis. It is the antisymmetric DM exchange interaction that forces confinement of spin moments in the $\boldsymbol{ab}$ plane in order to lower the energy of the system and hence magneto-crystalline anisotropy arises. Higher order spin-phonon coupling evident in the change in phonon frequency of the two magnetically ordered states with Γ_3 symmetry can also be quantified using Eq. 3.11). Phonon frequencies of the magnetically ordered states with Γ_3(I) (ω_A) and Γ_3(II) (ω_M) orderings are:

$$\begin{aligned} \mu\omega_A^2 &= \frac{\partial^2 H}{\partial u^2}|_{M=0} = k + 2\beta A^2, \\ \mu\omega_M^2 &= \frac{\partial^2 H}{\partial u^2}|_{A=0} = k + 2\gamma M^2, \end{aligned} \tag{3.15}$$

where μ is the reduced mass. This gives the temperature dependence of the Γ_1 modes arising from spin-phonon coupling (as A varies with temperature below T_N).

Calculating the overlap of phonon modes with Γ_1 symmetry of the two states with Γ_3 magnetic ordering we identify the phonons coupling strongly with spin and find $\Delta\omega$=15 cm^{-1} (1.86 meV), which quantifies the strength of fourth order spin-phonon coupling. The nonzero eigen-displacements of Mn and equatorial oxygen (O4) atoms (see Figure 3.9) according to the phonon mode (Γ_1 symmetry) of Γ_3(I) state which are not present in the phonon mode (Γ_1 symmetry) of Γ_3(II) state effectively modify the superexchange and Dzyaloshinskii-Moriya interactions between Mn^{3+} ions through the changes in bond length (Mn-O4) and bond angle (Mn-O4-Mn), which give rise to quadratic spin-phonon coupling in $YMnO_3$ and it can be observed experimentally.

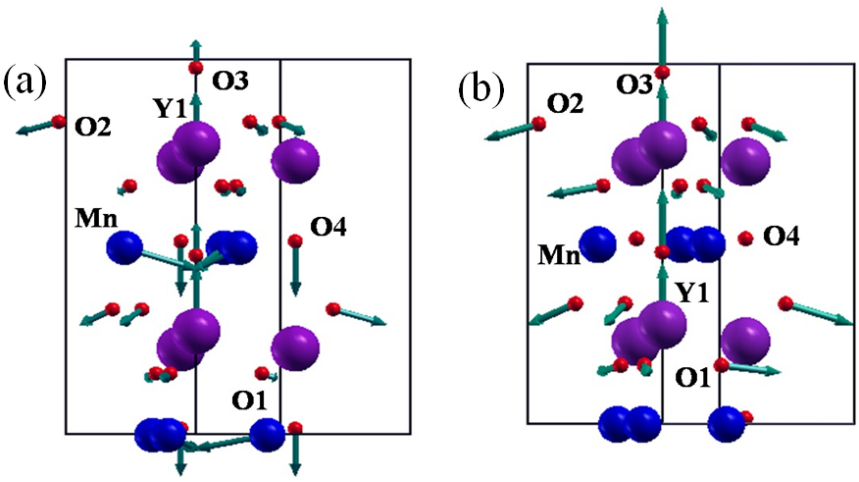

Figure 3.9: Visualization of the eigen-displacements of zone-centre phonon modes (side view) with Γ_1 symmetry having frequencies of (a) 264 cm^{-1} (Γ_3(I) phase) and (b) 279 cm^{-1} (Γ_3(II) phase). Copyright (2015) by the American Physical Society [47].

3.4.5 Properties at T>0 K

To determine the behaviours of primary (A and M) and secondary (u) order parameters of Néel transition as a function of temperature, we consider a model Hamiltonian

as described in Eq. 3.1 along with additional terms contributed by phonons (Eq. 3.11), given as:

$$\begin{aligned} H = J_p \sum_{\langle ij \rangle} \hat{s}_i.\hat{s}_j + J_{ip} \sum_{\langle ij \rangle} \hat{s}_i.\hat{s}_j + K_p \sum_i \sin^2\theta_i + K_a \sum_i (\hat{r}_i.\hat{s}_i)^2 \\ + \frac{1}{2}ku^2 + cA^2u, \end{aligned} \tag{3.16}$$

where k is the spring constant associated with Γ_1 phonon mode and c is the third-order spin-phonon coupling constant. We ignore fourth-order spin-phonon coupling terms in our model Hamiltonian as their contribution to total energy are not significant. Minimizing Eq. 3.16 with respect to u, the resulting u_{min} is expressed as,

$$\begin{aligned} u_{min} &= -\frac{c}{k}A^2 = -\frac{2\alpha}{c}A^2, \\ \text{where } \alpha &= \frac{c^2}{2k}. \end{aligned} \tag{3.17}$$

After substituting the value of u_{min} in Eq. 3.16 we get,

$$\begin{aligned} H = J_p \sum_{\langle ij \rangle} \hat{s}_i.\hat{s}_j + J_{ip} \sum_{\langle ij \rangle} \hat{s}_i.\hat{s}_j + K_p \sum_i \sin^2\theta_i + K_a \sum_i (\hat{r}_i.\hat{s}_i)^2 \\ - \alpha \sum_q (A_q^2)^2, \end{aligned} \tag{3.18}$$

where q and i (j) vary from 1 to total number of unit cells (P) and spins ($6P$) respectively. To evaluate the value of α (0.89 meV), we consider the spring constant (2.6 eV/bohr^2) and spin-phonon coupling constant (5.01 mRy/bohr) associated with the Γ_1 phonon mode with frequency 152 cm^{-1}. We consider this particular phonon mode (ω=152 cm^{-1}) as it strongly couples with spins, i.e., atomic positions get affected easily by the change of magnetic ordering. We renormalize the constant α (α_1=$\frac{\alpha \times 6P}{P^2}$) to make the energy (Eq. 3.18) proportional to total number of spins

$(6P)$.

3.4.5.1 Results of Monte Carlo simulations

We perform heating-up and cooling-down Monte Carlo simulations (with periodic boundary conditions) using the model Hamiltonian (Eq. 3.18) to estimate Néel temperature (T_N). The values of order parameters (A, M and u) at each temperature are estimated by using the expressions given as,

$$\begin{aligned} A &= \frac{1}{P \times N_{ave}} \sum_{j=1}^{N_{ave}} \sum_{q=1}^{P} |A_{q,j}|, \\ M &= \frac{1}{P \times N_{ave}} \sum_{j=1}^{N_{ave}} \sum_{q=1}^{P} |M_{q,j}| \text{ and} \\ u &= -\frac{\alpha_1 P}{3c \times N_{ave}} \sum_{j=1}^{N_{ave}} \left(\frac{1}{P} \sum_{q=1}^{P} |A_{q,j}| \right)^2. \end{aligned} \tag{3.19}$$

N_{ave} denotes the number of Monte Carlo steps used for averaging properties and P is the total number of unit cells. We observe a discontinuity or jump in the value of A at Néel temperature (T_N) whereas the value of M remains zero throughout the temperature range (see Figure 3.10). Presence of thermal hysteresis around T_N highlights the first-order nature of Néel transition. Amplitude of Γ_1 phonon mode (u) becomes finite below T_N and it facilitates the confinement of spins and their orderings in the ***ab*** plane according to Γ_3(I) symmetry (A). Thus, it explains the microscopic mechanism behind the experimentally observed giant magnetoelastic effect. Our estimated Néel temperature (51 K) is in close agreement with its experimental value (75 K) [67]. Magnetic susceptibility and specific heat associated with

phase transition are expressed as,

$$\begin{aligned} \chi_A &= \frac{\langle A^2\rangle - \langle A\rangle^2}{k_B T}, \\ \chi_M &= \frac{\langle M^2\rangle - \langle M\rangle^2}{k_B T}, \\ C_V &= \frac{\langle E^2\rangle - \langle E\rangle^2}{k_B T^2}, \\ \text{where } \langle E\rangle &= \frac{1}{N_{ave}} \sum_{j=1}^{N_{ave}} E_j. \end{aligned} \tag{3.20}$$

Magnetic susceptibility associated with A (χ_A) and specific heat (C_V) show a peak near T_N (see Figure 3.10). Absence of any peak in χ_M (see Figure 3.10) indicates that the ordering of M does not occur throughout the temperature range.

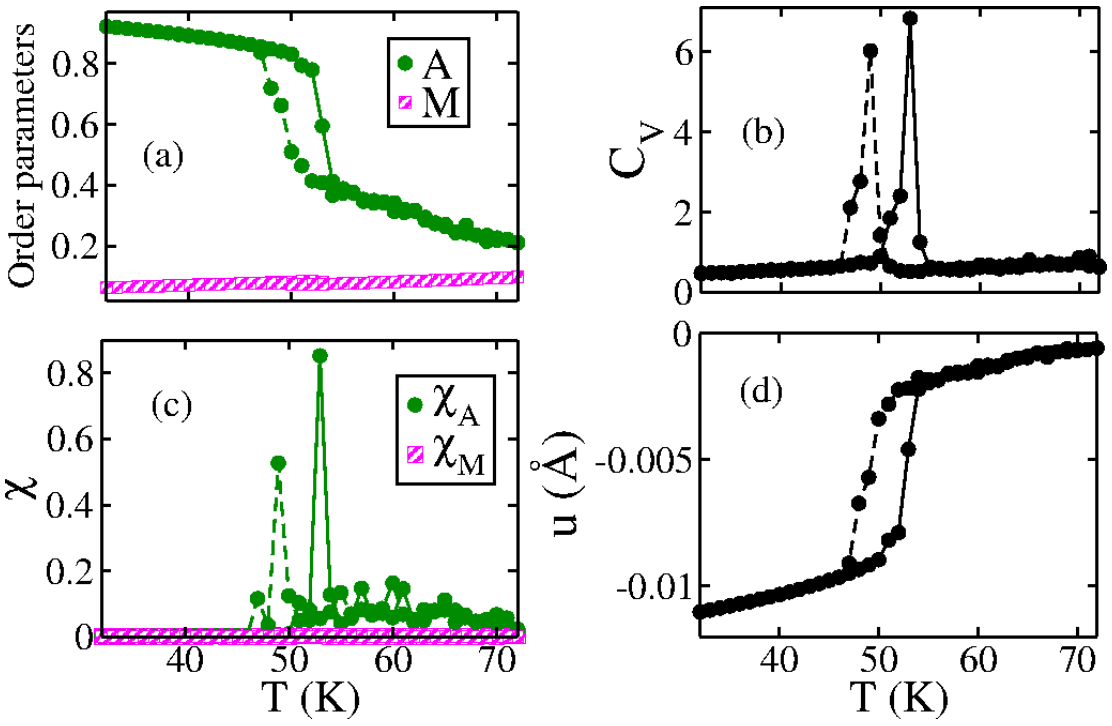

Figure 3.10: Temperature variations of (a) antiferromagnetic order parameters (A and M), (b) specific heat (C_V), (c) magnetic susceptibilities associated with A and M (χ_A and χ_M) and (d) amplitude of the phonon mode (u).

We evaluate the fourth-order Binder cumulant associated with order parameter,

which is defined as,

$$C_4 = \frac{\langle O^4 \rangle}{\langle O^2 \rangle^2}, \tag{3.21}$$

where O (= A and M) is the order parameter. The value of $C_4(A)$ is 1.0 in both low (below T_N) and high temperature (above T_N) phases (see Figure 3.11). However, the discontinuity in $C_4(A)$ at T_N indicates first-order nature of phase transition. Absence of discontinuity in $C_4(M)$ at T_N highlights that M does not order throughout the temperature range (see Figure 3.11). To understand the behaviour of $C_4(A)$ with temperature, we determine the distribution of A (see Figure 3.11) in both low (2 K) and high (68 K) temperature phase. At low temperature phase (below T_N), the distribution of A is a Delta function centered at A=1.0 (see Figure 3.11). This indicates that the value of fourth-order Binder cumulant ($C_4(A)$) will be 1 as the values of $\langle A^4 \rangle$ and $\langle A^2 \rangle$ become 1.0 in low temperature phase. In the high temperature phase, the distribution of A becomes Gaussian with its centre at A_0 (=0.19). The expression of $C_4(A)$ in the high temperature phase is given as,

$$C_4(A) = \frac{3\sigma^4 + 6A_0^2\sigma^2 + A_0^4}{(\sigma^2 + A_0^2)^2}, \tag{3.22}$$

where A_0 (=0.19) is the position of the peak and σ (=0.0127) is the standard deviation of Gaussian distribution. The value of $C_4(A)$ is approximated to 1.0 in high temperature phase (above T_N).

We now discuss formation of magnetic domains in the low temperature phase. The magnetic states with A and -A types of orderings are energetically equivalent states according to the model Hamiltonian (Eq. 3.18). These states are related to each other by time reversal symmetry. We define two angles θ_1 and θ_2 (see Figure 3.12) to distinguish the ordering of spins at the magnetic domain wall separating A (θ_1=θ_2=$\pi/2$) and -A (θ_1=θ_2=-$\pi/2$) states in the ***ab*** plane. There are two possibilities of orderings of spins at the magnetic domain wall (spins rotate by 180°) depending

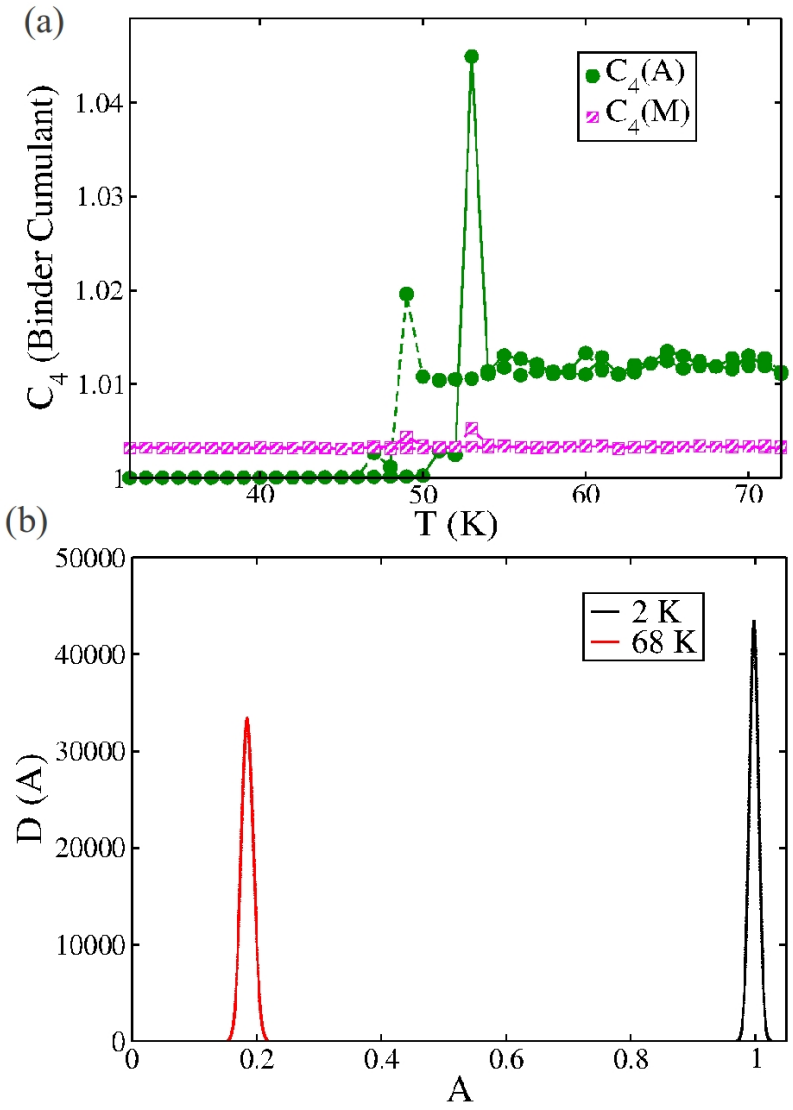

Figure 3.11: (a) Variations of Binder cumulants associated with A and M with temperature and (b) distribution of A at 2 K (low temperature phase) and 68 K (high temperature phase).

on the way of changing θ_1 and θ_2 in the ***ab*** plane. If θ_1 and θ_2 change in the same manner, magnetic ordering according to Γ_4 symmetry (see Figure 3.2e, θ_1=θ_2=0) arises at the domain wall. Antiferroagnetic ordering according to Γ_1 symmetry (see Figure 3.2a, θ_1=π and θ_2=0) arises at the domain wall when θ_1 and θ_2 change in the opposite manner. To determine the orderings of spins at the domain wall, we simulate the model Hamiltonian (Eq. 3.18) by considering a large supercell of system size 16×16×16 (24,576 spins). We observe a stripe domains of magnetic orderings

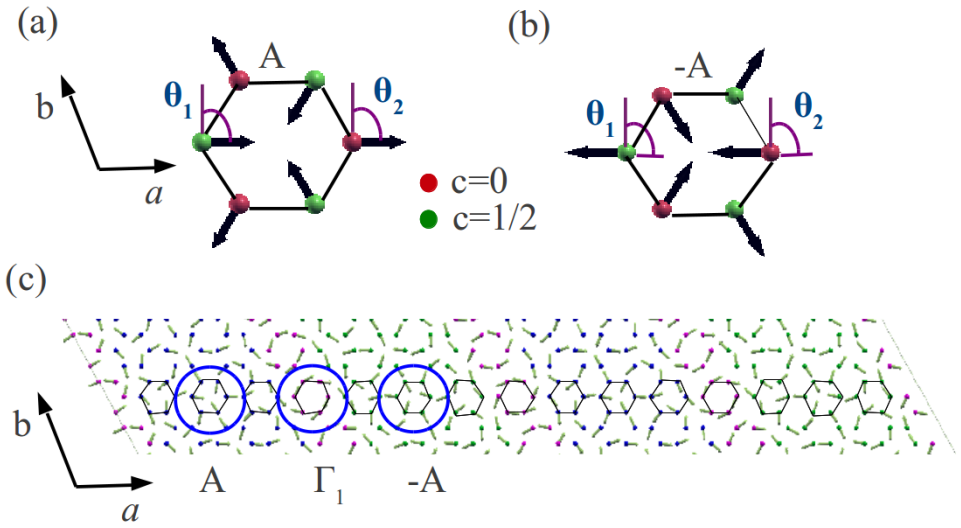

Figure 3.12: (a) A type, (b) -A type magnetic orderings are represented by θ_1 and θ_2 angles. (c) stripe domains of magnetic orderings and Γ_1 magnetic ordering at the 180° domain wall. Unit cells with blue, green and pink colored atoms represent A, -A and Γ_1 magnetic states in (c).

(A and -A) and presence of Γ_1 magnetic ordering at the 180° domain wall at 2 K (see Figure 3.12). Our estimated width of the magnetic domain wall is approximately about 18 Å (three unit cells thicker), which is comparable with the value calculated earlier for $LuMnO_3$ [62]. Next, we discuss magnetic states which are locked to the structural states.

3.4.5.2 Structural and magnetic states

An unstable K_3 phonon mode ($\sqrt{3}\times\sqrt{3}$ lattice distortion) of $P6_3/mmc$ phase (above T_C) is responsible for structural transition at T_C [61]. The trimerization angle associated with K_3 mode (Φ) is the azimuthal angle enclosed by the in-plane (***ab***) displacement of one apical oxygen (O1) atom (see Figure 3.13). Φ can take six different values (Φ=0, $\pi/3$, $2\pi/3$, $-\pi/3$, $-2\pi/3$, π) depending on the direction of displacement of one particular O1 atom (see Figure 3.13a, 3.13c and 3.13d). The six different values of Φ (energetically equivalent) suggest six possible ways of trimerizing the unit cell (six structural states) below T_C [62]. Ferroelectric polarization

emerges as a result of nonlinear coupling between trimerization (K_3) and soft polar mode (Γ_2^-) [62]. The sign of polarization (P_c) in the states with Φ=0, $2\pi/3$ and $-2\pi/3$ is positive, whereas it is negative for states with Φ=π, $\pi/3$ and $-\pi/3$.

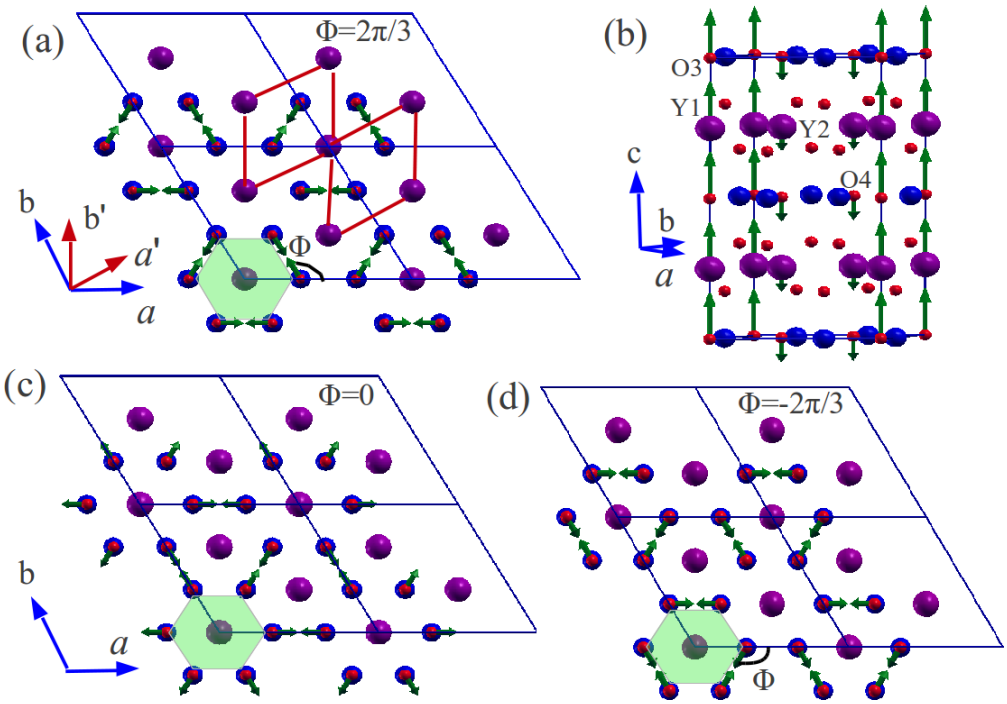

Figure 3.13: In-plane displacements of O1 atoms (red color) according to K_3 phonon mode with (a) Φ=$2\pi/3$, (c) Φ=0 and (d) Φ=$-2\pi/3$. (b) Displacements of yttrium (Y1 and Y2 in purple color) and equatorial oxygen (O3 and O4 in red color) atoms according to K_3 phonon mode. Blue colored atoms represent Mn atoms. a and b denote the lattice vectors of $P6_3cm$ structure (below T_C). b' and a' indicate the lattice vectors of $P6_3/mmc$ structure (above T_C). The green hexagon encloses six Mn atoms (blue color) and six O1 atoms (red color) in the $P6_3cm$ phase.

Below T_N, atoms move according to Γ_1 phonon mode to stabilize the Γ_3(I) magnetic ordering as discussed in previous subsection. The atomic displacements associated with K_3 phonon mode (with Φ=0, see Figure 3.13b and 3.13c) of $P6_3/mmc$ phase is equivalent to the atomic displacements according to Γ_1 phonon mode (see Figure 3.7) of $P6_3cm$ phase. The in-plane atomic displacements of O1 atoms according to Γ_1 phonon mode is presented in Figure 3.14. In the green hexagon (see Figure 3.14c), there can be u, u' and u'' types of structural orderings. The six structural states below T_N are defined as: (a) u (Φ=0), (b) $-u$ (Φ=π), (c) u' (Φ=$2\pi/3$), (d) $-u'$

(Φ=-π/3), (e) u'' (Φ=-2π/3), (f) -u'' (Φ=π/3).

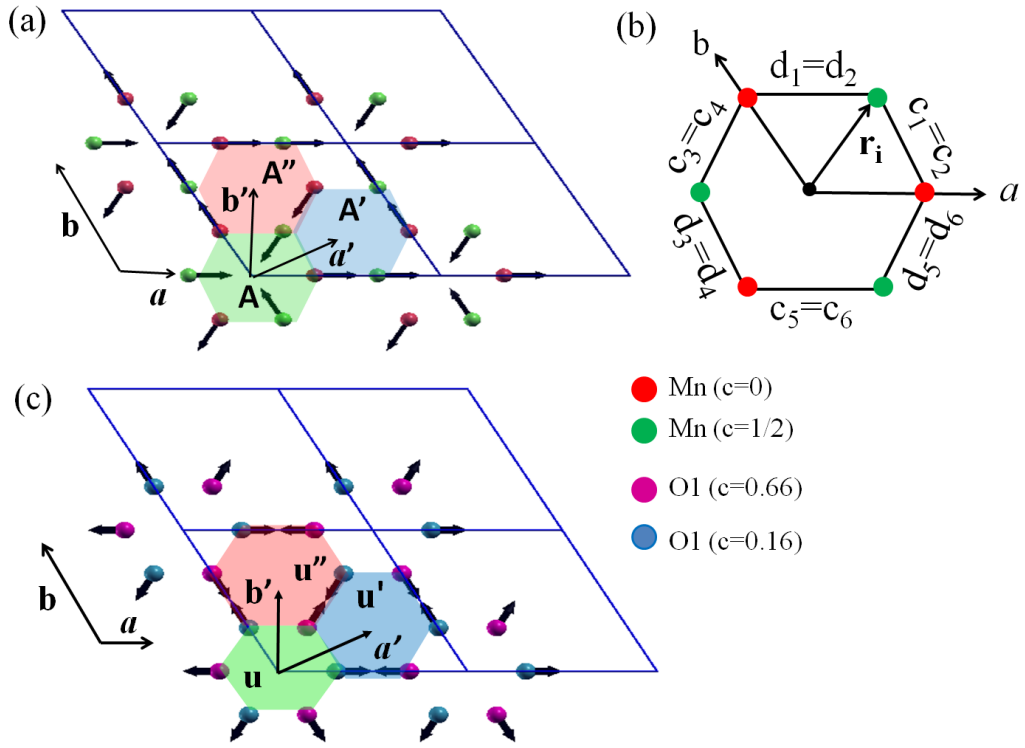

Figure 3.14: (a) Magnetic ordering (magnetic moments of Mn atoms) according to Γ_3 symmetry, (c) atomic displacements (O1 atoms) according to Γ_1 phonon mode. (b) Hexagon formed by six Mn atoms to define magnetic states (A, A' and A''). b' and a' indicate the lattice vectors of $P6_3/mmc$ structure (above T_C).

The coupling between ferroelectric (P_c) and structural orderings ({u}) is linear below T_N. The change in the in-plane displacements of apical oxygen atoms (O1) according to Γ_1 mode (u) changes the axes of in-plane magnetocrystalline anisotropy, i.e., magnetic ordering. The transformation of the structural, ferroelectric and an-

Table 3.7: Transformation of order parameters under the operations of symmetry elements of $P6_3/mmc$ space group.

Order parameter	$R_{a'}$ (Translation)	$R_{b'}$ (Translation)	I (Spatial inversion)	τ (Time reversal)
Φ	Φ+2π/3	Φ-2π/3	-Φ	Φ
A	A'	A''	A	-A
u	u'	u''	-u	u
P_c	P_c	P_c	-P_c	P_c

tiferromagnetic order parameters under the generators of $P6_3/mmc$ space group (above T_C) is summarized in Table 3.7. When u changes to u' and u'' (under the translation operation $R_{a'}$ and $R_{b'}$), A simultaneously changes to A' and A''. In the green hexagon (see Figure 3.14a and 3.14c), there can be A' and A'' types of magnetic orderings based on the structural orderings (u' and u''). The six magnetic states as an outcome of spin-phonon coupling are: (a) A, (b) -A, (c) A', (d) -A', (e) A'', (f) -A'' (see Figure 3.14). The coupling between structural, ferroelectric and antiferromagnetic order parameters is expressed as,

$$H_{coupling}(\{u\},\{A\},P_c) = cA^2u + c'A'^2u' + c''A''^2u'' + g(u+u'+u'')P_c, \qquad (3.23)$$

where c, c' and c'' are third-order spin-phonon coupling constant and their values are equal due to hexagonal symmetry. The six possible choices of orderings below T_N (according to Eq. 3.23) in one unit cell (e.g., green hexagon in Figure 3.14) are: (a) A, (u, -u), (P_c, -P_c), (b) A', (u', -u'), (P_c,-P_c), (c) A'', (u'', -u''), (P_c, -P_c), (d) -A, (u, -u), (P_c, -P_c), (e) -A', (u', -u'), (P_c, -P_c) and (f) -A'', (u'', -u''), (P_c, -P_c). The indirect coupling between antiferromagnetic and ferroelectric order parameters is mediated by structural order parameter. Thus, the structural and ferroelectric domain walls are also magnetic domain walls due to the third-order spin-phonon coupling. A' and A'' antiferromagnetic order parameters are mathematically expressed as,

$$\begin{aligned} A' &= \frac{1}{6}\sum_{i=1}^{6}(\hat{c}_i.\hat{s}_i), \\ A'' &= \frac{1}{6}\sum_{i=1}^{6}(\hat{d}_i.\hat{s}_i), \end{aligned} \qquad (3.24)$$

where $\hat{c}_i$ and $\hat{d}_i$ represent arms of the hexagon (see Figure 3.14). The modified model

Hamiltonian to capture these six possible magnetic orderings is given by,

$$\begin{aligned} H = {} & J_p \sum_{\langle ij \rangle} \hat{s}_i.\hat{s}_j + J_{ip} \sum_{\langle ij \rangle} \hat{s}_i.\hat{s}_j + K_p \sum_i \sin^2\theta_i \\ & + K_a \sum_i (\hat{r}_i.\hat{s}_i)^2 + K'_a \sum_i (\hat{c}_i.\hat{s}_i)^2 + K''_a \sum_i (\hat{d}_i.\hat{s}_i)^2 \\ & + \alpha_1 \sum_q (A_q^2)^2 + \alpha'_1 \sum_q (A'^2_q)^2 + \alpha''_1 \sum_q (A''^2_q)^2. \end{aligned} \tag{3.25}$$

K_a (α_1), K'_a (α'_1) and K''_a (α''_1) stabilize A, A' and A'' magnetic orderings respectively. The values of K_a, K'_a and K''_a (α_1, α'_1 and α''_1) are equal due to hexagonal symmetry. q and i (j) changes from 1 to total number of unit cells (P) and total number of spins ($6P$) respectively.

We execute heating-up and cooling-down simulations by considering a large supercell of system size 60×60×8 with periodic boundary conditions. For heating-up Monte Carlo simulations, we consider a mixture of three magnetic states (A, A' and A'') as initial state. We consider a configuration with spins are randomly oriented as initial state for cooling-down Monte Carlo simulations. We determine the values of magnetic and structural order parameters (A, A', A'', u, u' and u'') in one type of unit cell (green hexagon in Figure 3.14) at each temperature in a similar way of calculating A and u using Eq. 3.19. A, A' and A'' show discontinuity at T_N, whereas the value of M remains zero at all temperature (see Figure 3.15). The estimated value of T_N (62 K) increases by 11 K (see subsection 3.4.5.1) after considering the coupling between different structural and magnetic states (Eq. 3.25). u, u' and u'' also show discontinuity at T_N (See Figure 3.15) and their finite values below T_N stabilize A, A' and A'' magnetic states. Specific heat (C_V) and order parameter susceptibilities (χ_A, $\chi_{A'}$ and $\chi_{A''}$) show a peak near T_N (see Figure 3.15).

We notice a stripe domains of magnetic orderings at 2 K (with periodic boundary conditions). The observed sequence of six magnetic states in the stripe domain phase

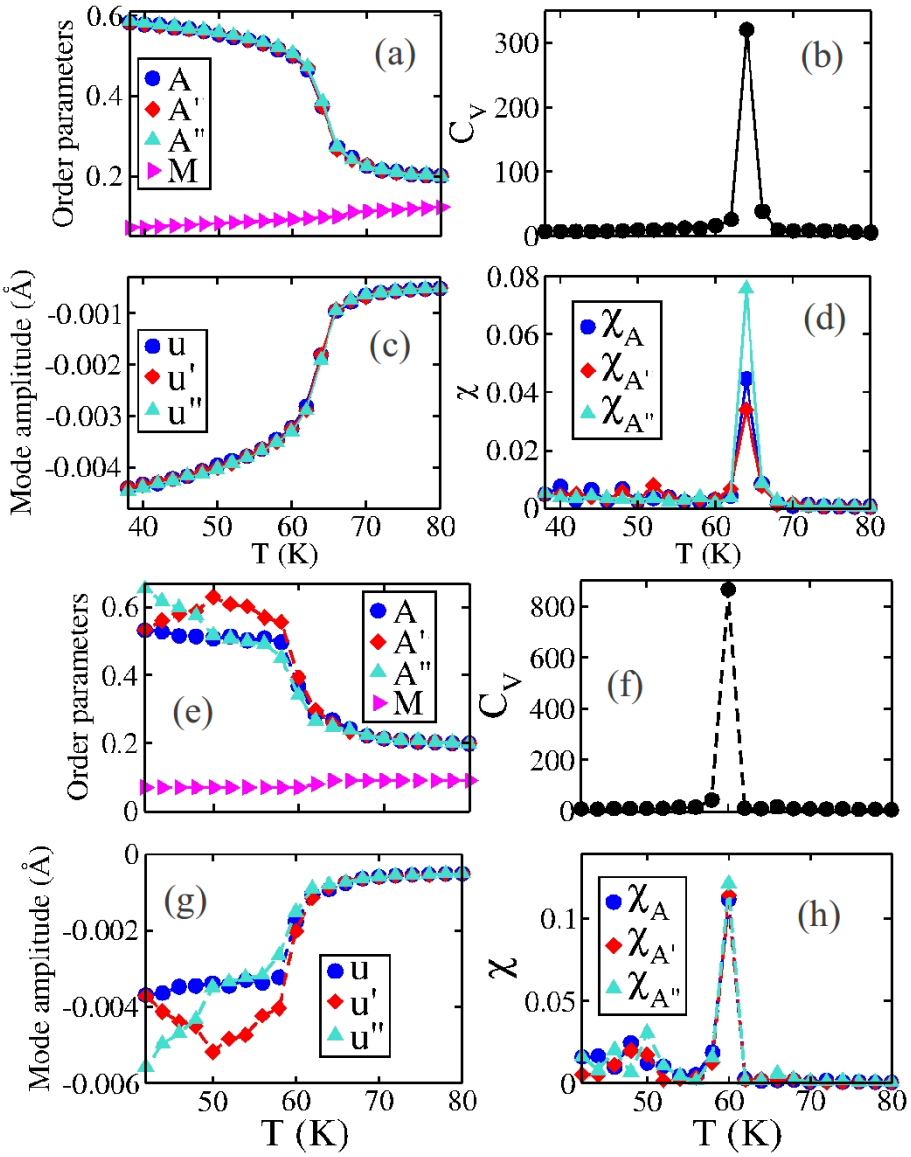

Figure 3.15: Temperature variations of (a) and (e) magnetic order parameters (A, A', A'' and M), (b) and (f) specific heat (C_V), (c) and (g) amplitude of the phonon mode (u, u' and u''), (d) and (h) magnetic susceptibilities associated with A, A', A''. Heating and cooling curves are represented by solid and dashed lines respectively.

in the ***ab*** plane at 2 K (see Figure 3.16) is (-A', A, -A'', A', -A and A''). Between the two consecutive magnetic domains, spins rotate by 60° in the anti-clockwise direction and this is different from the 180° magnetic domain wall as discussed in earlier subsection. The magnetic domain walls are much thicker ($\approx$ 30 Å) than structural domain walls (5-10 Å [62]). Another possible sequence of magnetic orderings is

(-A', A'', -A, A', -A'' and A), which is energetically equivalent to the previously mentioned sequence of magnetic orderings (-A', A, -A'', A', -A and A''). In this case, spins rotate by 60° in the clockwise direction at the domain wall. Depending on the interplay between structural, ferroelectric and magnetic orderings (Eq. 3.23), the unique choices of structural and ferroelectric orderings for the observed sequence of magnetic orderings (-A', A, -A'', A', -A and A'') in the stripe domain phase (see Figure 3.16) are: (a) -A': (-u', -P_c), A: (u, P_c), -A'': (-u'', -P_c), A': (u', P_c), -A: (-u, -P_c) and A'': (u'', P_c); (b) -A': (u', P_c), A: (-u, -P_c), -A'': (u'', P_c), A': (-u', -P_c), -A: (u, P_c) and A'': (-u'', -P_c). Atomic displacement vectors (O1 atoms) rotate by 60° either in the anti-clockwise (first choice) or clockwise (second choice) directions between two consecutive structural and magnetic domains. The sign of polarization (P_c) changes alternately in the structural (magnetic) domains in stripe domain phase as the structural domain wall has to be the ferroelectric domain wall due to the improper nature of ferroelectricity.

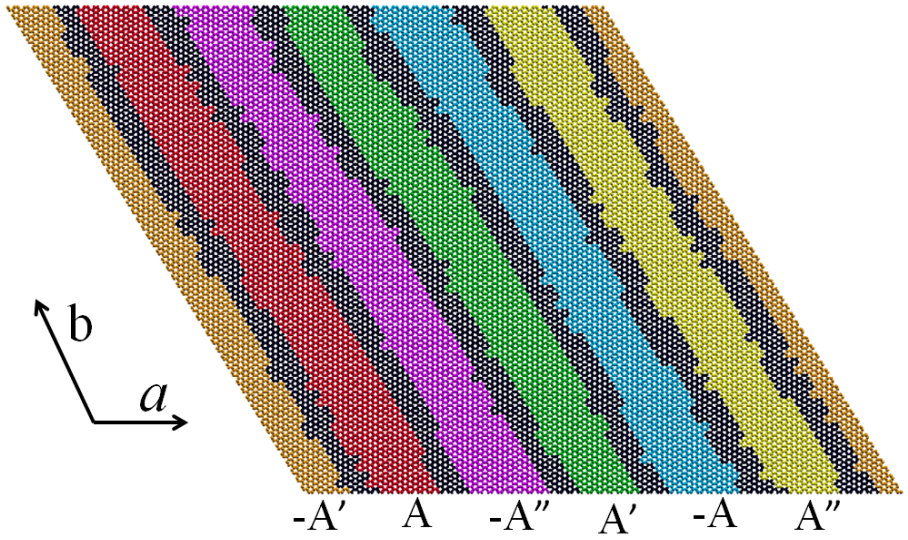

Figure 3.16: Stripe domains of magnetic orderings at 2 K in the ***ab*** plane. Black colored portion denotes magnetic domain wall.

In addition, we notice magnetic vortex state or topological defect state (see Figure 3.17) using both open and periodic boundary conditions, which is topologically

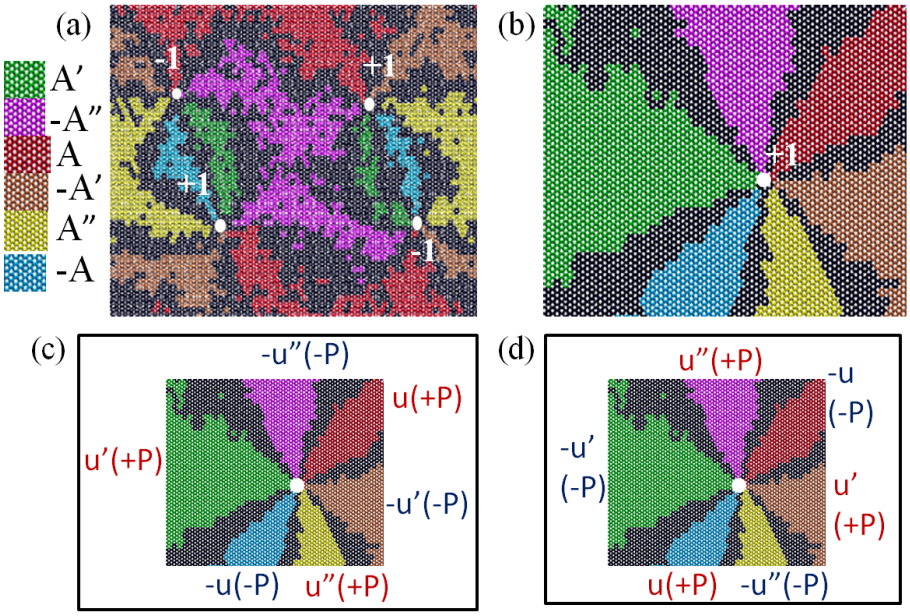

Figure 3.17: Magnetic vortex and antivortex states obtained with (a) periodic boundary condition and (b) open boundary condition. +1 (-1) are the topological charges associated with magnetic vortex (antivortex) state. (c) Structural vortex and (d) antivortex states originating from magnetic vortex state. Black colored portion denotes magnetic, structural and ferroelectric domain wall.

different from stripe domain phase. Magnetic vortex state (topological defects) arise at the intersection of six magnetic domain walls (see Figure 3.17). The topological charge (Q_T) associated with magnetic vortex state (antivortex state) is +1 (-1) as spins in the neighboring magnetic domains (see Figure 3.17) rotate by 60° in the clockwise (anticlockwise) direction. The net topological charge (Q_T) enclosed by the system is zero with periodic boundary condition and ±1 states with open boundary condition (see Figure 3.17). The magnetic vortex state (Q_T=+1) gives rise to structural vortex or antivortex states due to third-order spin-phonon coupling (see Figure 3.17). In the structural vortex (antivortex) state, atomic displacement vectors (O1 atoms) rotate in the clockwise (anticlockwise) direction by 60° between the neighboring domains (see Figure 3.17). Our predicted orderings of structural and ferroelectric domains from spin-phonon coupling below T_N are in agreement with earlier theoretical and experimental findings [62, 71, 72].

3.5 Summary

We have demonstrated using first-principles calculations that magnetic frustration and spin-orbit coupling give rise to (a) a remarkable magneto-crystalline anisotropy in the noncollinear ordering of magnetic moments of Mn^{3+} ions in $YMnO_3$ and (b) a consequent gap in the electronic spectrum even in the case of vanishing on-site electron correlations (Hubbard U=0). In the magnetic ground state, spins of Mn^{3+} ions are confined in the ***ab*** plane, and have the symmetry of Γ_3(I) representation. We showed how the crystal field, magnetic exchange and the spin-orbit coupling determine the splitting and ordering of energy levels of d orbitals of Mn^{3+} ion in $YMnO_3$ that result in the observed magnitude of its local magnetic moment. Forces and stresses arising from the change in magnetic ordering from Γ_3(I) to Γ_3(II) give the spin-phonon and spin-strain couplings, which are relevant to displacements of atoms and changes in lattice parameters during the change in magnetic state in $YMnO_3$ at T_N, *i.e.* the magneto-elastic effect. Estimating the spin-phonon and spin-strain couplings, and we showed using Landau theory that a strong and anisotropic coupling of spin with Γ_1 phonons and strain constitute the microscopic mechanism of the observed giant-magnetoelastic effect at Néel temperature. Our finding of strong coupling of the phonon modes (ω = 666 cm^{-1} and 152 cm^{-1}) of Γ_1 symmetry with spin is consistent with their strong dependence on T observed in Raman spectra at $T < T_N$. We find anomalies in the zz components of Born effective charges that originate from strong hybridization between Y $4d$ and oxygen (apical) $2p$ orbitals.

From ab-initio statistical mechanical analysis, we establish that ordering of spins in the ***ab*** plane according to Γ_3 symmetry below T_N is facilitated by freezing in of finite amplitude of the Γ_1 phonon mode. The Néel transition is first-order in nature and our estimates of T_N is in good agreement with its experimental value. We predict the presence of magnetic ordering according to Γ_1 symmetry at the 180°

magnetic domain wall. We have demonstrated that six magnetic domains order to form two topologically distinct states: (a) stripe domain phase and (b) magnetic vortex state (topological defects). We highlight the specific initial states that facilitate the formation of topological defects. The magnetic vortex and antivortex structures (topological defects) occur along the line defined by intersection of six magnetic domain walls, and the magnetic domains are locked to the structural or ferroelectric domains. Spins and atomic displacements rotate by 60° either in clockwise or in anticlockwise directions between two consecutive domains in stripe and vortex domain phases. Due to spin-phonon coupling, magnetic vortex state gives rise to structural vortex and antivortex states.

Chapter 4

Accuracy of first-principles interatomic interactions and predictions of ferroelectric phase transitions in perovskite oxides *

4.1 Introduction

Ferroelectrics are an important class of materials that exhibit a spontaneous macroscopic electric polarization that is switchable with application of an electric field, and hence have a wide range of technological applications [98, 99]. Perovskite oxides are the most interesting of ferroelectric materials, and have been studied enormously [27, 100] since the discovery of barium titanate in 1945 [12]. Perovskite oxides have a chemical formula ABO_3, with the A cation at the corner of the cube,

*This work has been published in Physical Review B and reprinted with permission from [97]. Copyright (2017) by the American Physical Society, URL: https://doi.org/10.1103/PhysRevB.95.054111.

and with the B and O atoms located at the body-centered and face-centered positions respectively. There is a remarkable diversity in the structural instabilities and phase transitions that these perovskites undergo: ferroelectric transitions (associated with polar distortion) in $BaTiO_3$[†], $PbTiO_3$ and $KNbO_3$, antiferroelectric transition (involving nonpolar distortion) in $PbZrO_3$ and antiferrodistortive transition (associated with tilting of oxygen octahedra) in $SrTiO_3$ [100, 101]. These phase transitions and competing instabilities have singularly important consequences to their properties relevant to technological applications. First-principles density functional calculations have been used extensively in microscopic studies of structural transitions via identifying the responsible phonon mode for structural transition, studying the stability of the intermediate phases and predicting transition temperatures (T_C) [28, 100, 102, 103]. It has been established that harmonic and anharmonic couplings between phonons and strain-phonon coupling constants are the most crucial parameters that govern the phase transitions in perovskites [28, 100, 104]. Accuracy in determination of these parameters and subsequent estimation of transition temperatures is naturally limited by the DFT errors in estimation of lattice constants.

Earlier all-electron calculations (FLAPW) within the local density approximation (LDA) predicted the cubic phases of $KNbO_3$ to be stable (in contradiction to experimental results), and $PbTiO_3$ and $BaTiO_3$ to be unstable at the optimized lattice constant [100, 105]. The discrepancies between experimental and theoretical results (using LDA) for cubic $KNbO_3$ have been removed by implementing ultrasoft pseudopotentials [100]. But, LDA is well known to underestimate the lattice constant by 1-2% as it neglects the effects of inhomogeneity in electron density [14, 100]. Such over-binding of the structure predicted within LDA results in underestimation of the difference in energies of cubic and distorted structures [106]. This is

[†]Rabe and Ghosez, Physics of Ferroelectrics, Springer Publications, 2007, Chapter 4

because the ferroelectric instability is a strong function of cell volume of those materials [106, 107].

While *ab initio* MD or MC simulations would be effective in estimation of the temperature-dependent transition properties, the size (length scale) of a system needed to capture the phase transition and corresponding computational cost make them presently impractical. Instead, an approximate approach is adopted that uses an effective Hamiltonian, which focuses on the low-energy structural configurations in MD or MC simulations [28, 102]. Thus, there are two sources of errors in first-principles description of ferroelectric transitions: (a) ones arising from the choice of DFT functional, and (b) ones arising from the truncation of the set of configurations through the effective Hamiltonian.

As an example, the too-shallow potential well in $BaTiO_3$ underestimates the transition temperature (T_C) determined using a parametrized effective Hamiltonian based on LDA [102]. However, this problem was resolved by applying a negative pressure to the system [102]. Also, the value of T_C of $PbTiO_3$ using interaction parameters (calculated using LDA) at the experimental lattice constant is underestimated [28]. On the other hand, the gradient density approximation (GGA) mostly overestimates the lattice constants and gives supertetragonal structures of $PbTiO_3$ and $BaTiO_3$ [107]. By including the density gradient, GGAs can predict accurate structures or energies, but not both together [34, 108]. This suggests an important avenue for further functional development which can correctly capture structural properties, i.e., lattice constant, anharmonic coupling between phonon modes and strain-phonon coupling parameters, which are relevant to the structural transition. The GGA functional proposed by Wu and Cohen (WC-GGA) has been known to accurately calculate the ferroelectric properties of $BaTiO_3$ and $PbTiO_3$ [109]. However, the WC-GGA fails to precisely determine the properties of atoms and molecules, as it was constructed for solids (slowly varying electron density) [109].

The recently developed nonempirical strongly constrained and appropriately normed semilocal density functional (SCAN) has been shown to estimate accurate structures and energetics of diversely bonded molecules and materials (for slowly as well as rapidly varying electron densities) and to improve the band gap, which was underestimated by LDA and GGA [37–40]. The SCAN meta-GGA satisfies all the 17 known exact constraints (about 6 for exchange, 6 for correlation and 5 for the sum of two) appropriate to semilocal functionals by including the orbital kinetic energy densities [37]. The calculations are computationally more expensive using SCAN meta-GGA than normal GGA or LDA, but SCAN is more efficient than hybrid functionals due to its semilocal nature.

In this chapter, we present the ground-state properties of eight perovskites, i.e., $BaTiO_3$, $CaTiO_3$, $SrTiO_3$, $PbTiO_3$, $KNbO_3$, $NaNbO_3$, $PbZrO_3$ and $BaZrO_3$ using the SCAN meta-GGA functional, and notice a significant improvement of lattice constants and band gaps of eight oxides compared to earlier theoretical results using LDA [100]. We then estimate T_C's of $BaTiO_3$, $PbTiO_3$ and $KNbO_3$ using the parametrized effective Hamiltonian based on the SCAN meta-GGA functional, calculate the lowest-order coupling between soft mode and higher energy modes, and determine the consequences of approximations in construction of the effective Hamiltonian for finite-temperature properties.

4.2 Methods

First-principles calculations based on density functional theory have been performed here on eight perovskites using the SCAN meta-GGA exchange-correlation functional as implemented in the VASP code [37, 110, 111]. For calculations, we use projector augmented wave (PAW) potentials containing a contribution from kinetic energy density of core electrons [112]. We have considered eight oxides, i.e., $BaTiO_3$,

$SrTiO_3$, $PbTiO_3$, $CaTiO_3$, $KNbO_3$, $NaNbO_3$, $PbZrO_3$ and $BaZrO_3$, for determining ground-state properties. We use $5s$ and $5p$ states of Ba, $3s$ state ($3s$ and $3p$ states) of K (Ca), $4s$ and $4p$ states of Sr, Zr and Nb, $2p$ state of Na and $5d$ state of Pb as valence states. An energy cutoff of 560 eV has been used to truncate the plane-wave basis used to represent wave functions. Integrations over Brillouin zone were sampled on an $8 \times 8 \times 8$ uniform mesh of k-points.

MD simulations for studying the phase transitions of $BaTiO_3$, $PbTiO_3$ and $KNbO_3$ (considering the effective Hamiltonian from Ref. [102]) are performed using the FERAM code [102, 113, 114]. At each temperature in our simulation within the canonical ensemble, temperature is kept fixed using the Nose-Poincare thermostat [115]. The time step was set to Δt=2 fs. We use a supercell of system size $L_x \times L_y \times L_z = 16 \times 16 \times 16$ and temperature step $\pm$ 5 K in heating-up and cooling-down simulations. We use 20,000 thermalization steps and 40,000 steps for averaging properties of the system at each temperature. The initial configuration used in cooling-down simulations of all three compounds is a paraelectric state with $\langle u_\alpha \rangle$=0.0 (α=x,y,z) and $\langle u_\alpha^2 \rangle$-$\langle u_\alpha \rangle^2$=(0.12 Å)^2. In the heating-up simulation, we choose ferroelectric states of three compounds ($\langle u_z \rangle$=0.33 Å and $\langle u_x \rangle$=$\langle u_y \rangle$=0.0 for $PbTiO_3$ and $\langle u_\alpha \rangle$=0.11 Å for $BaTiO_3$ and $KNbO_3$) as initial configurations.

4.3 Results and discussion

4.3.1 Ground-state properties

4.3.1.1 Structural and electronic properties

We optimized lattice parameters of cubic perovskite structures of eight ABO_3 compounds, i.e., $BaTiO_3$, $SrTiO_3$, $CaTiO_3$, $PbTiO_3$, $KNbO_3$, $NaNbO_3$, $PbZrO_3$ and $BaZrO_3$, using the SCAN meta-GGA functional. Our results in comparison with

LDA are shown in Figure 4.1 [100]. The lattice constants of cubic $SrTiO_3$, $CaTiO_3$, $PbZrO_3$ and $BaZrO_3$ are overestimated slightly by 0.1-0.5% (see Figure 4.1) whereas for other compounds lattice constants are underestimated at the most by 0.8% relative to the experimental values [100]. Lattice constants optimized using SCAN are better compared to the earlier theoretical results obtained from calculations considering all-electron (FLAPW) and ultrasoft pseudopotentials with LDA [100]. Lattice parameters of cubic $BaTiO_3$, $PbTiO_3$ and $SrTiO_3$ are overestimated by 0.2% from the values obtained using the WC-GGA functional [102].

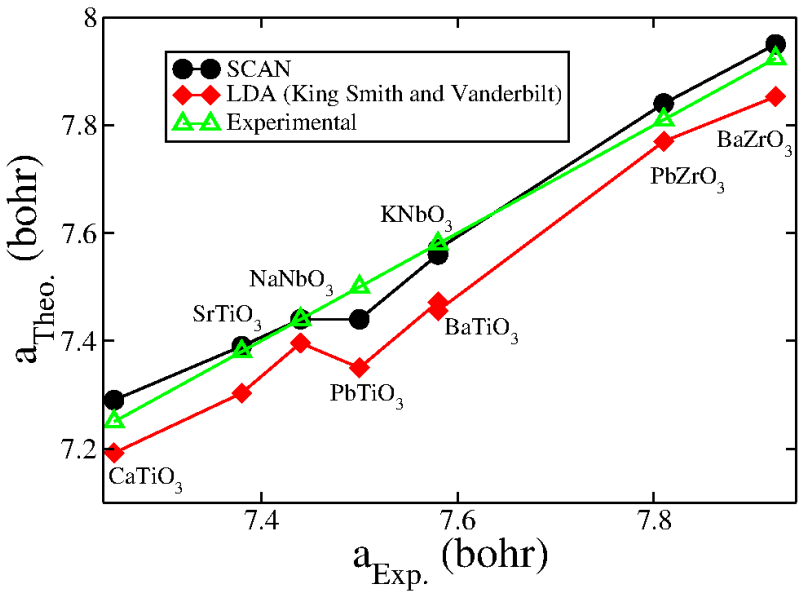

Figure 4.1: Optimized lattice constants of eight cubic oxides using the SCAN meta-GGA functional in comparison with experimental and earlier theoretical (using LDA) lattice parameters [100]. Lattice constants (experimental and SCAN metaGGA) of cubic $KNbO_3$ and $BaTiO_3$ are close to each other.

We then optimized lattice constants of the tetragonal phases of $BaTiO_3$ and $PbTiO_3$ (as shown in TABLE 4.1). The SCAN-based calculated values of $\boldsymbol{a}$ of tetragonal phases of $BaTiO_3$ and $PbTiO_3$ are within 0.025% of experimental values and are better than earlier theoretical results using LDA, PBE-GGA and hybrid functionals [107]. The generalised gradient approximation (GGA) in the PBE

Table 4.1: Optimized tetragonal lattice parameters (in Å) and z component of atomic displacements (from cubic to tetragonal phase) for $BaTiO_3$ and $PbTiO_3$ using the SCAN meta-GGA functional in comparison with earlier theoretical and experimental results [107]. Atomic displacements are given as a fraction of the c parameter.

Compound	Property	LDA [107]	PBE [107]	WC-GGA [107]	B3LYP [107]	SCAN	Expt. [107]
$BaTiO_3$	a	3.954	4.013	3.982	3.996	3.985	3.986
	$\boldsymbol{c/a}$	1.006	1.035	1.012	1.066	1.027	1.010
	d_z^{Ti}	0.011	0.018	0.013	0.019	0.016	0.015
	$d_z^{O_I}$	-0.014	-0.039	-0.022	-0.057	-0.029	-0.023
	$d_Z^{O_{II}}$	-0.009	-0.022	-0.013	-0.031	-0.017	-0.014
$PbTiO_3$	a	3.872	3.834	3.870	3.819	3.881	3.88
	$\boldsymbol{c/a}$	1.041	1.221	1.086	1.277	1.110	1.063 (300 K)
	d_z^{Ti}	0.037	0.062	0.044	0.076	0.029	0.040
	$d_z^{O_I}$	0.090	0.189	0.121	0.223	0.118	0.112
	$d_Z^{O_{II}}$	0.106	0.178	0.133	0.198	0.120	0.112

parametrized form overestimates lattice constants and gives supertetragonal structures of $BaTiO_3$ and $PbTiO_3$ (see TABLE 4.1). In addition, the differences in the z components of atomic positions between cubic and tetragonal phases of $BaTiO_3$ (ferroelectric distortion) are slightly overestimated compared to experimental values and are better than earlier theoretical results using LDA, PBE-GGA and hybrid functionals [107]. For $PbTiO_3$, the level of agreement between experiment and our estimates of these differences in atomic positions is not that good. This overestimation of atomic displacements is caused by the slight overestimation of $\boldsymbol{c/a}$ ratios of $PbTiO_3$ (see TABLE 4.1). We analyzed this in depth, and found that the energy surface of $PbTiO_3$ is very flat (shallow) and small energy differences result in large changes in structural parameters. However, our estimates of $\boldsymbol{c/a}$ ratios of tetragonal $BaTiO_3$ and $PbTiO_3$ are better than those of other functionals (LDA, PBE-GGA and hybrid) [107]. Our results for $BaTiO_3$ and $PbTiO_3$ are comparable to the earlier results obtained using the WC-GGA functional and treating Ti and O atoms at the all-electron level (HF pseudopotentials for Pb and Ba) [107]. For $KNbO_3$, the $\boldsymbol{c/a}$ ratio (1.034) is slightly overestimated with SCAN compared to the experimental

value (1.017) [116]. In addition, we optimized lattice parameters of orthorhombic (a, b and c) and rhombohedral (a and α) structures of $BaTiO_3$ and $KNbO_3$ using SCAN metaGGA functional (see TABLE 4.2). Our SCAN metaGGA-based estimates of lattice parameters of orthorhombic and rhombohedral phases are within 0.4% of experimental values [117–119]. The agreement with experiment is much better than that obtained with PBE-GGA and WC-GGA functionals [120]. Elastic

Table 4.2: Optimized lattice parameters of orthorhombic and rhombohedral phases of $BaTiO_3$ and $KNbO_3$ using the SCAN meta-GGA functional in comparison with earlier theoretical and experimental results [117–120].

Compound	Phase	Lattice parameters	PBE-GGA	WC-GGA [120]	SCAN	Expt. [117–119]
$BaTiO_3$	Rhombo	a (Å)	4.073		4.029	4.003
		α (°)	89.76		89.83	89.84
	Ortho	a (Å)	4.110		4.047	4.041
		b (Å)	3.996		3.983	3.982
		c (Å)	4.113		4.051	4.065
$KNbO_3$	Rhombo	a (Å)	4.071	4.041	4.032	4.016
		α (°)	89.81	89.85	89.82	89.83
	Ortho	a (Å)	4.111	4.141	4.055	4.080
		b (Å)	3.988	3.980	3.969	3.973
		c (Å)	4.119	4.179	4.057	4.116

constants of cubic perovskites have been determined from the stress-strain relationship. The elastic constants of $BaTiO_3$ using SCAN are comparable to the value obtained using LDA (see TABLE 4.3). The values of bulk modulus of $KNbO_3$ and $PbTiO_3$ are 197 GPa and 203 GPa respectively, which agree to about 2% with the values obtained earlier using LDA [100]. For $SrTiO_3$, elastic constants are within 16% of the experimental values [121]. It has been observed experimentally that C_{11}, C_{12} and C_{44} of $SrTiO_3$ are strong functions of temperature, and decrease by 4% when temperature drops from 30°C to -160°C [122]. The dependence of elastic constant on temperature has also been noticed experimentally for $BaTiO_3$ and $PbTiO_3$ [123]. As first-principles based DFT calculations do not include the effect of temperature, we consider this deviation of elastic constants from the experimental

values as acceptable. The exchange-correlation functional influences mostly C_{11} and C_{12} parameters for all materials. SCAN-based estimates of C_{11} are overestimated compared to experimental values whereas other elastic constants are close to experimental values (see TABLE 4.3) [121, 124]. Our calculated direct band gaps at the

Table 4.3: Elastic constants (in GPa) of cubic perovskites using the SCAN meta-GGA functional in comparison with earlier theoretically-calculated values using LDA [100] and experimentally-measured values [121, 124].

		Method		
Compound	Elastic constant	SCAN	LDA [100]	Expt. [121, 124]
$BaTiO_3$	C_{11}	328	329	206
	C_{12}	118	117	140
	C_{44}	131	130	126
$SrTiO_3$	C_{11}	374	389	316
	C_{12}	113	105	101
	C_{44}	120	155	119
$CaTiO_3$	C_{11}	399	407	
	C_{12}	110	96	
	C_{44}	104	102	
$PbTiO_3$	C_{11}	340	335	229
	C_{12}	135	146	101
	C_{44}	108	100	100
$KNbO_3$	C_{11}	427	465	232
	C_{12}	83	67	90
	C_{44}	103	96	75
$NaNbO_3$	C_{11}	472	482	230
	C_{12}	84	70	90
	C_{44}	77	78	76
$PbZrO_3$	C_{11}	332	371	
	C_{12}	94	86	
	C_{44}	67	67	
$BaZrO_3$	C_{11}	325	335	
	C_{12}	88	95	
	C_{44}	93	89	

X point (of $PbTiO_3$ and $PbZrO_3$) and at the Γ point (of other compounds) of cubic

perovskites (at optimized lattice constant) in comparison with earlier theoretical and experimental results are presented in Figure 4.2 [100, 121, 125–129]. SCAN gives a better estimation of band gaps of perovskites and other materials [39, 40] compared to LDA [37, 38, 100]. LDA underestimates the band gaps by 40-50%. The band gaps in SCAN are also underestimated, but are modestly improved over LDA.

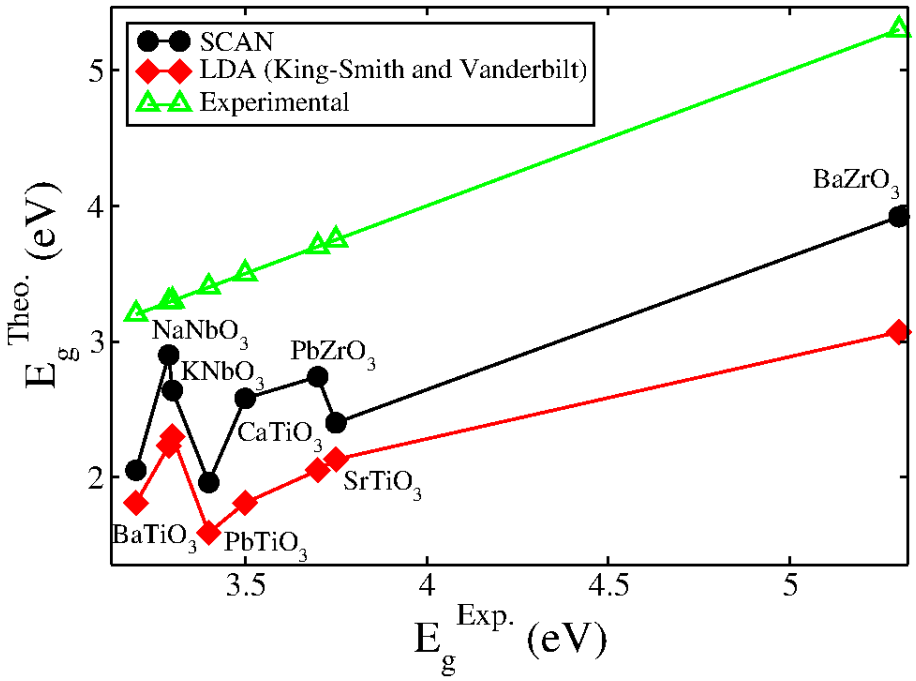

Figure 4.2: Direct band gaps of eight perovskites in comparison with earlier theoretical results using LDA [100] and experimentally measured band gaps [121, 125–129]. Experimentally measured band gaps of cubic $KNbO_3$ and $NaNbO_3$ are nearly equal.

Next, we determine the effect of the exchange-correlation functional on vibrational properties which have important consequences for the finite-temperature properties of perovskites.

4.3.1.2 Vibrational properties

For the five-atom unit cell of cubic phase of perovskites, there are twelve optical phonon modes at Γ point. Out of twelve optical modes, three triply-degenerate

phonon modes have Γ_{15} symmetry and one triply-degenerate mode has Γ_{25} symmetry. The eigenvector of the phonon mode with Γ_{25} symmetry involves atomic displacements along the z direction as (v_z^A=0, v_z^B=0, $v_z^{O_I}$=$\frac{1}{\sqrt{2}}$, $v_z^{O_{II}}$=-$\frac{1}{\sqrt{2}}$ and $v_z^{O_{III}}$=0). Phonon modes with Γ_{15} symmetry are relevant to the ferroelectric transition [100]. One of the eigenvalues of the phonon modes with Γ_{15} symmetry of the cubic phase becomes negative (for the five-atom unit cell as experimental ground state), which indicates the cubic phase to be unstable. We have compared the optical phonon frequencies (see TABLE 4.4) obtained at the optimized lattice constant with earlier theoretical calculations based on LDA, GGA and hybrid functionals and experimentally-measured frequencies [107, 130, 131]. Our estimated zone-centre optical phonon frequencies (TO1, TO2, TO3 and TO4) of $BaTiO_3$ and $SrTiO_3$ using SCAN are in excellent agreement (within 3% for $BaTiO_3$ and 8% for $SrTiO_3$) with experimental values and are better compared to earlier estimates calculated using LDA, GGA and hybrid functionals [107]. For $PbTiO_3$, our calculated phonon frequencies differ by 19% from earlier theoretical results (using LDA, GGA and hybrid functionals) [107]. Phonon frequencies of cubic $PbTiO_3$ can not be readily compared with experimental values, as the literature is not available. SCAN predicts phonon frequencies much closer to the experimental values for cubic $KNbO_3$ compared to earlier LDA calculations [130]. Moreover, our predicted phonon frequencies (of $BaTiO_3$, $SrTiO_3$ and $KNbO_3$) are better than earlier theoretically-calculated values using different functionals [107, 130, 131].

We now examine the eigenvalues of unstable phonon modes (TO1) with Γ_{15} symmetry (see TABLE 4.5). We find that the value of the harmonic coupling parameter κ is positive (see TABLE 4.5) for cubic $BaZrO_3$, which assumes the cubic phase at all temperature, and is consistent with the earlier LDA result and experimental findings [100]. The positive value of κ for $SrTiO_3$ is consistent with the antiferrodistortive transition associated with phonon mode at q$\neq$0. In contrast, earlier LDA

Table 4.4: Predicted zone-centre optical phonon frequencies (in cm^{-1}) of $BaTiO_3$, $PbTiO_3$, $SrTiO_3$ and $KNbO_3$ at theoretical lattice constants in comparison with earlier theoretically-calculated and experimentally-measured frequencies [107, 130, 131].

Compound	Symmetry	Functional								
		LDA [107, 131]	WC-GGA [107]	B1-WC [107]	PBE [131]	HSE [131]	LDA-LAPW [130]	SCAN	Exp. [107, 130, 131]	
$BaTiO_3$	Γ_{15} (TO1)	75i	128i	145i				196i		
	Γ_{15} (TO2)	193	186	195				182	182	
	Γ_{15} (TO3)	480	469	482				478	482	
	Γ_{25} (TO4)	286	282	299				297	306	
$PbTiO_3$	Γ_{15} (TO1)	127i	132i	146i				147i		
	Γ_{15} (TO2)	145	141	138				140		
	Γ_{15} (TO3)	515	510	513				530		
	Γ_{25} (TO4)	219	211	231				227		
$SrTiO_3$	Γ_{15} (TO1)	80			115i	74i		86	91 (297 K)	
	Γ_{15} (TO2)	177			147	162		173	169 (297 K)	
	Γ_{15} (TO3)	563			512	533		553	544 (297 K)	
	Γ_{25} (TO4)	226			234	250		244	265 (297 K)	
$KNbO_3$	Γ_{15} (TO1)	143i					197i	247i		
	Γ_{15} (TO2)	188					170	207	198	
	Γ_{15} (TO3)	506					473	483	521	
	Γ_{25} (TO4)						243	272	280	

results gave a negative value of κ for $SrTiO_3$ [100], while another LDA calculation with high plane-wave kinetic energy cutoff (50 Ry) predicts a positive value (0.096 $eV/Å^2$) of κ of $SrTiO_3$. For other compounds, the value of κ is found to be negative which is in agreement with earlier theoretical results using LDA (see TABLE 4.5). Overall, our calculated values of κ's are more negative for $BaTiO_3$, $KNbO_3$ and $NaNbO_3$ compared to earlier LDA results whereas they are more positive for other compounds, which are relevant for defining the potential energy surface [100].

The eigenvector of the soft mode of the cubic structure and its amplitude in the ferroelectric phase of $BaTiO_3$ (see TABLE 4.6) are comparable to the eigenvector obtained earlier using LDA [100] although the lattice constants obtained using the two functionals are quite different. On the other hand, the displacement of the Pb atom associated with the soft mode is large compared to the value obtained using

Table 4.5: Harmonic (κ in eV/Å^2), anharmonic (α and γ in eV/Å^4) and strain-phonon coupling parameters (B_{1xx}, B_{1yy} and B_{4yz} in eV/Å^2) in comparison with earlier theoretically-calculated values using LDA [100]. κ is the harmonic and α and γ are the anharmonic coupling coefficients (estimated by fitting the fourth-order polynomial in soft mode amplitude) in the on-site energy.

		Coupling coefficients							
Compound	Functional	κ	α	γ	B_{1xx}	B_{1yy}	B_{4yz}	α'	γ'
$BaTiO_3$	SCAN	-1.92	112.73	-158.93	-225.76	-18.04	-20.93	57.92	-36.54
	LDA [100]	-1.68	110.32	-163.07	-210.32	-19.29	-7.72	60.68	-42.75
$SrTiO_3$	SCAN	0.49	21.37	-22.06	-64.64	-39.94	46.41	16.89	-44.47
	LDA [100]	-0.086	51.72	-65.85	-136.04	5.78	-10.61	32.06	-3.45
$CaTiO_3$	SCAN	-0.47	4.14	1.89	-49.97	-30.01	-10.81	2.59	2.52
	LDA [100]	-1.11	7.93	-2.07	-56.92	5.78	-9.65	4.48	21.03
$PbTiO_3$	SCAN	-0.77	6.79	-4.41	-66.37	-2.99	-23.25	1.59	1.79
	LDA [100]	-1.24	15.17	-15.51	-75.25	0.00	-2.89	7.58	8.62
$KNbO_3$	SCAN	-3.14	110.67	-149.97	-257.21	15.53	-3.28	57.58	-14.82
	LDA [100]	-1.49	130.32	-211.34	-290.40	31.84	-0.96	63.43	-38.27
$NaNbO_3$	SCAN	-1.53	28.27	-31.37	29.14	-44.96	6.66	24.82	-22.07
	LDA [100]	-1.19	57.92	-88.26	-164.98	48.24	0.00	32.06	-14.14
$PbZrO_3$	SCAN	-1.36	2.41	-0.17	33.67	5.49	-18.52	1.45	-3.75
	LDA [100]	-1.51	3.79	-4.48	-21.22	6.75	-0.96	3.10	-1.03
$BaZrO_3$	SCAN	1.82	1.69	2.41	16.98	29.62	19.39	0.55	-1.52
	LDA [100]	0.75	5.52	0.00	-45.34	6.75	-10.61	3.10	18.62

LDA, although amplitudes of soft modes using the two different functionals are similar [100]. Eigenvectors of the soft modes of $NaNbO_3$ and $CaTiO_3$ obtained using the two functionals (SCAN and LDA) are slightly different from each other [100]. For other compounds, eigenvectors and amplitudes of the soft modes are comparable with the results estimated earlier using LDA [100]. Our calculated eigenvector of the soft mode of $BaTiO_3$ is similar to the eigenvector obtained using the WC-GGA functional [102].

Anharmonic coupling coefficients α and γ in the on-site energy are determined from the expressions for energy as a function of soft mode amplitude (u) along [001]

Table 4.6: Computed eigenvectors (ξ_z^{atom} (unitless)) and amplitudes of the soft modes of eight perovskites in comparison with earlier LDA results [100, 132].

Compound	Method	ξ_z^A	ξ_z^B	$\xi_z^{O_{1,2}}$	$\xi_z^{O_3}$	Amplitude (bohr)
$BaTiO_3$	SCAN	0.15	0.77	-0.18	-0.56	0.24
	LDA [100]	0.20	0.76	-0.21	-0.53	0.25
$PbTiO_3$	SCAN	0.65	0.43	-0.40	-0.27	0.56
	LDA [100]	0.57	0.51	-0.41	-0.27	0.54
$KNbO_3$	SCAN	0.12	0.80	-0.21	-0.50	0.30
	LDA [100]	0.18	0.80	-0.31	-0.37	0.22
$SrTiO_3$	SCAN	0.52	0.57	-0.39	-0.30	0.0
	LDA [132]	0.49	0.60	-0.41	-0.27	
$CaTiO_3$	SCAN	0.74	0.27	-0.42	0.17	0.38
	LDA [132]	0.68	0.36	-0.44	-0.17	
$NaNbO_3$	SCAN	0.35	0.70	-0.38	-0.31	0.38
	LDA [132]	0.43	0.64	-0.43	-0.21	
$PbZrO_3$	SCAN	0.81	0.09	-0.41	-0.09	1.06
	LDA [132]	0.77	0.15	-0.44	-0.04	
$BaZrO_3$	SCAN	0.75	0.23	-0.43	-0.13	0.0
	LDA [132]	0.70	0.27	-0.46	-0.05	

and [111] directions (up to fourth-order terms in u) [100]:

$$E_{001}(u) = \kappa u^2 + \alpha u^4, \tag{4.1a}$$

$$E_{111}(u) = 3\kappa u^2 + (9\alpha + 3\gamma)u^4. \tag{4.1b}$$

The energies of unstrained cubic $PbTiO_3$ and $BaTiO_3$ as a function of soft mode displacements are shown in Figure 4.3. When strain is not applied, the rhombohedral phase has minimum energy for $BaTiO_3$ and $PbTiO_3$ (as shown in Figure 4.3), consistent with earlier LDA results [100]. The depth of the double-well (as shown in Figure 4.3) is larger for $PbTiO_3$ compared to $BaTiO_3$ as the values of α and γ (obtained using SCAN) of $PbTiO_3$ are small (see TABLE 4.5).

We compute strain-phonon coupling parameters to find the ground state of each

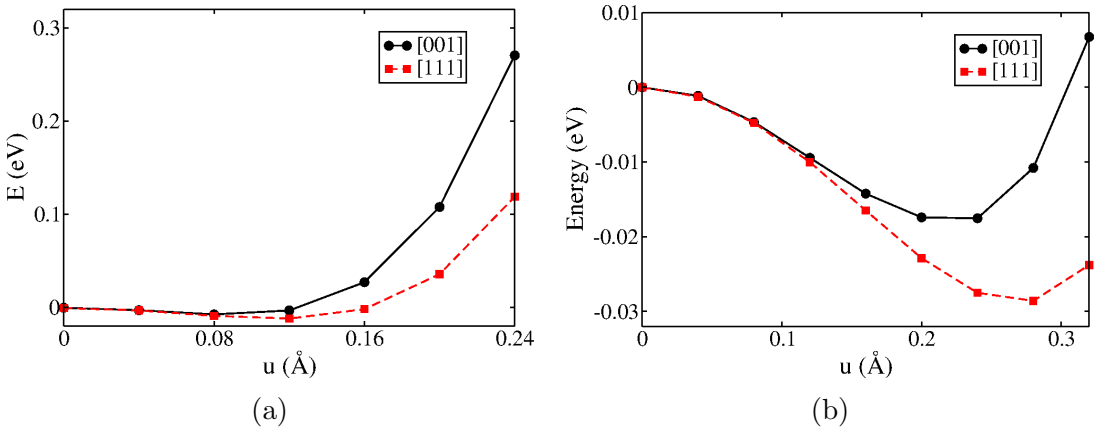

Figure 4.3: Variations of total energies of unstrained (a) $BaTiO_3$ and (b) $PbTiO_3$ as a function of polar structural distortions (u) along [001] and [111] directions respectively, from SCAN.

oxide. Strain-phonon coupling parameters (B_{1xx}, B_{1yy} and B_{4yz}) of the eight perovskites are determined by calculating the change in the values of κ with strain. Changes in the eigenvalues of an x-polarized soft mode (κ_x) with the applications of strains along x (η_1) and y directions (η_2) give B_{1xx} and B_{1yy} respectively (as shown in see Figure 4.4). To find the value of B_{4yz}, we calculate the change in the value of κ of the soft mode distortion along [111] direction with the change of shear strain (η_4). We notice that strain-phonon coupling parameters are sensitive to the exchange-correlation functional (see TABLE 4.5). B_{1yy} and B_{4yz} coupling parameters of $BaTiO_3$ and $PbTiO_3$ mostly get affected by the exchange-correlation functional. For $NaNbO_3$, $PbZrO_3$ and $BaZrO_3$, B_{1xx} even changes its sign with the change of exchange-correlation functional. We consider these calculated parameters to obtain the ground state of every compound, as discussed below.

Using the fourth-order expansion of energy as a function of soft mode amplitude and strain, the energy differences between cubic (E_C), tetragonal (E_T), orthorhombic (E_O) and rhombohedral (E_R) phases are [100]:

$$E_C - E_T = -\frac{\kappa^2}{4\alpha'}, \tag{4.2a}$$

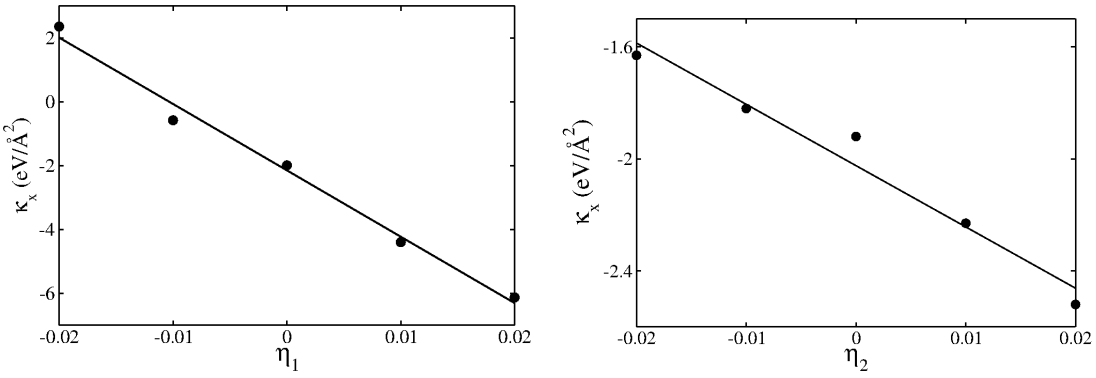

(a) (b)

Figure 4.4: Eigenvalue (κ_x) of x-polarized soft mode (with Γ_{15} symmetry) of $BaTiO_3$ as functions of strains applied (a) along x (η_1) and (b) y (η_2) directions, from SCAN.

$$E_C - E_O = -\frac{\kappa^2}{4\alpha' + \gamma'}, \tag{4.2b}$$

$$E_C - E_R = -\frac{\kappa^2}{4(\alpha' + \gamma'/3)}. \tag{4.2c}$$

α' and γ' are renormalized anharmonic coupling constants (as given in Eq. 11b, 12b and 13b in Ref. [100]) which depend on elastic constants, strain-phonon coupling parameters and bare anharmonic coupling constants (α and γ).

We find that the value of γ is typically negative as shown in TABLE 4.5. The introduction of strain switches the sign of γ in some cases, which highlights the importance of strain-phonon coupling. If κ is less than zero, stability of tetragonal and rhombohedral ground states require γ' to be greater and less than zero respectively (using Eq. 4.2). Negative values of γ' of $BaTiO_3$, $KNbO_3$, $NaNbO_3$ and $PbZrO_3$ mean that the ground state is rhombohedral, which is consistent with earlier theoretical results using LDA [100]. For $PbTiO_3$ and $CaTiO_3$, the tetragonal state is the ground state as γ' is positive (consistent with earlier LDA results [100]). In addition, cubic phases of $SrTiO_3$ and $BaZrO_3$ have minimum energy as κ is positive. The experimentally-observed ground states for $SrTiO_3$, $CaTiO_3$ and $NaNbO_3$

are tetragonal (antiferrodistortive transition associated with oxygen octahedra rotation), orthorhombic (with 20 atoms in the unit cell) and monoclinic phase (20 atoms per unit cell) respectively [100]. Hence, these can not be explained using the fourth-order expansion of energy, which considers only the soft mode at the Γ point.

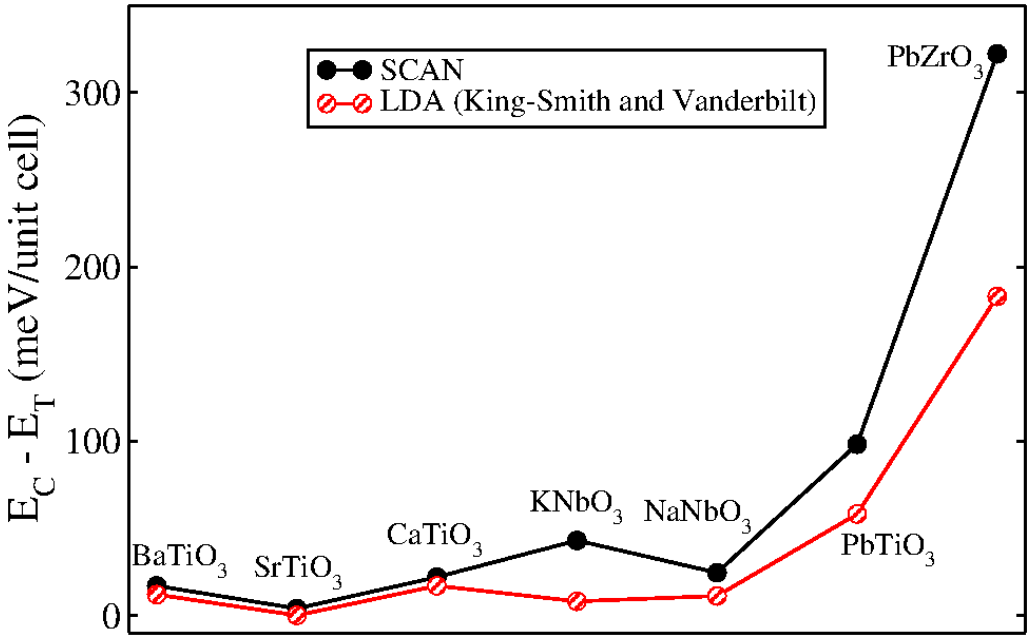

Figure 4.5: Calculated energy difference (using fourth-order expansion of energy as a function of soft mode amplitude) between cubic (E_C) and tetragonal (E_T) phases of perovskites in comparison with earlier theoretical results using LDA [100]. For $CaTiO_3$, we employ the result of another theoretical calculation using LDA from Ref. [132].

The calculated energy difference between cubic and tetragonal phases (using Eq. 4.2a) of $BaTiO_3$, $PbTiO_3$ and $KNbO_3$ are 16 meV/unit cell (12 meV/unit cell, LDA), 95 meV/unit cell (58 meV/unit cell, LDA) and 43 meV/unit cell (8 meV/unit cell, LDA) respectively (as shown in Figure 4.5). For $BaZrO_3$, the energy difference between cubic and tetragonal phase is 1.3 eV/unit cell which is much larger compared to the value (45 meV/unit cell) obtained using the parameters from earlier theoretical calculations using LDA [100]. For comparison of energy difference between cubic and tetragonal phases of $CaTiO_3$, we use parameters from another calculations (with LDA) with a high plane-wave kinetic energy cutoff (50

Ry) [132]. SCAN produces deeper potential wells (energy as a function of soft mode amplitude and strain) for all compounds, in comparison with earlier theoretical results using LDA [100, 132]. Depths of the potential well along the [110] and [111] directions (using Eq. 4.2b and 4.2c) are (19 meV/unit cell, 20 meV/unit cell) for $BaTiO_3$ and (46 meV/unit cell, 47 meV/unit cell) for $KNbO_3$ respectively. Our calculated energy differences (orthorhombic and rhombohedral) are larger compared to the depth obtained using LDA-based parameters ($BaTiO_3$: 14 meV/unit cell and 15 meV/unit cell, $KNbO_3$: 9 meV/unit cell and 10 meV/unit cell). As the depths of double-well energy surfaces are believed to be underestimated in the LDA framework, the description of total energy surfaces gets improved by the accurate estimation of lattice constants using SCAN.

4.3.2 Finite temperature properties

We now investigate the effect of the exchange-correlation functional on finite-temperature properties, i.e., transition temperatures of three compounds ($BaTiO_3$, $PbTiO_3$ and $KNbO_3$) whose ferroelectric transitions are associated with the soft mode at the Γ point.

4.3.2.1 Effective Hamiltonian

To predict the finite-temperature properties using MD simulation, we use an effective Hamiltonian [102, 113]:

$$H^{eff} = \frac{M^*_{dipole}}{2}\sum_{\boldsymbol{R},\alpha}\dot{u}^2_\alpha(\boldsymbol{R}) + \frac{M^*_{acoustic}}{2}\sum_{\boldsymbol{R},\alpha}\dot{\mathrm{w}}^2_\alpha(\boldsymbol{R}) + V^{self}(\{\boldsymbol{u}\}) + V^{dpl}(\{\boldsymbol{u}\}) + V^{short}(\{\boldsymbol{u}\}) + V^{elas,homo}(\eta_1,...,\eta_6) + V^{elas,inho}(\{\mathrm{w}\}) + V^{coup,homo}(\{\boldsymbol{u}\},\eta_1,...,\eta_6) + V^{coup,inho}(\{\boldsymbol{u}\},\{\mathrm{w}\}) - Z^*\sum_{\boldsymbol{R}}\mathcal{E}.\boldsymbol{u}(\boldsymbol{R}), \tag{4.3}$$

where **u** and **w** are the local soft mode amplitude vector (soft mode displacement vector) and acoustic mode displacement vector (lattice Wannier mode [133]) of the unit cell at position R respectively (α=x,y,z). η_1, ..., η_6 are the homogeneous strain components. M^*_{dipole} and $M^*_{acoustic}$ are effective masses associated with polar soft and acoustic modes respectively. Z^* is the Born effective charge associated with the soft mode, and $\mathcal{E}$ is the external electric field.

The third term in Eq. 4.3 represents local-mode self energy ($V^{self}(\mathbf{u})$) [102]:

$$V^{self}(\{\boldsymbol{u}\}) = \sum_{\boldsymbol{R}}\kappa_2 u^2(\boldsymbol{R}) + \alpha u^4(\boldsymbol{R}) + \gamma(u^2_x(\boldsymbol{R})u^2_y(\boldsymbol{R}) + u^2_y(\boldsymbol{R})u^2_z(\boldsymbol{R}) + u^2_z(\boldsymbol{R})u^2_x(\boldsymbol{R})) + k_1u^6(\boldsymbol{R}) + k_2(u^4_x(\boldsymbol{R})[u^2_y(\boldsymbol{R}) + u^2_z(\boldsymbol{R})] + u^4_y(\boldsymbol{R})[u^2_z(\boldsymbol{R}) + u^2_x(\boldsymbol{R})] + u^4_z(\boldsymbol{R})[u^2_x(\boldsymbol{R}) + u^2_y(\boldsymbol{R})]) + k_3u^2_x(\boldsymbol{R})u^2_y(\boldsymbol{R})u^2_z(\boldsymbol{R}) + k_4u^8(\boldsymbol{R}), \tag{4.4}$$

where $u^2(\mathbf{R}) = u^2_x(\mathbf{R}) + u^2_y(\mathbf{R}) + u^2_z(\mathbf{R})$.

Eq. 4.1a and 4.1b can be obtained from Eq. 4.4 by taking $\mathbf{u}(\mathbf{R})$=(0,0,u) and $\mathbf{u}$ ($\mathbf{R}$)=(u,u,u) and replacing κ_2 to κ and truncating the polynomial in u at the fourth-order terms. The fourth and fifth terms in Eq. 4.3 represent long-range dipole-dipole interaction and short-range harmonic interaction between optical displacements ($\mathbf{u}(\mathbf{R})$) up to third nearest neighbors. Terms containing acoustic mode displacement vector ($\mathbf{w}(\mathbf{R})$) have been integrated out by minimizing Eq. 4.3 with

respect to ($\mathbf{w}(\mathbf{R})$) [113]. Sixth and eighth terms in Eq. 4.3 are the elastic energy and coupling between homogeneous strain and optical mode ($\mathbf{u}$), which have been determined here by using the coupling constants (elastic constant ($C_{\alpha\beta\gamma\delta}$) and strain-phonon coupling ($B_{i\alpha\beta}$) parameters) as discussed in the earlier section. We did not include the effect of external electric field.

The short-range and long-range interaction parameters determine the energy (or frequency) of the soft mode at high symmetry points other than Γ. We determine phonon spectra at X, M and R points of the Brillouin zone of $BaTiO_3$, $PbTiO_3$ and $KNbO_3$ to calculate the short-range interaction parameters. These phonon calculations (at X, M and R points) were performed with (1×1×2), ($\sqrt{2} \times \sqrt{2}$×1) and ($\sqrt{2}\times\sqrt{2}\times\sqrt{2}$) supercells containing 10 atoms each respectively. In addition, we calculate phonon modes at the centre of the Σ axis (q=(110)$\frac{\pi}{2a}$) by considering $2\sqrt{2}\times 1 \times \sqrt{2}$ supercell with 20 atoms for $PbTiO_3$. We should note that these calculations use the cubic structure of these compounds. The long-range dipole-dipole interaction is proportional to Z^{*2}/ϵ_∞, where Z^* is the mode effective charges associated with the soft mode and ϵ_∞ is the dielectric constant [104]. Our calculated values of Z^* are 10.16 ($BaTiO_3$), 9.37 ($PbTiO_3$) and 11.52 ($KNbO_3$), M^* are 37.5 amu ($BaTiO_3$), 102.6 amu ($PbTiO_3$), 65.4 amu ($KNbO_3$) and ϵ_∞ are 6.27 ($BaTiO_3$), 7.95 ($PbTiO_3$) and 5.492 ($KNbO_3$). While the SCAN meta-GGA estimates of Z^{*2}/ϵ_∞ are within 10% of the LDA estimates, they are closer (within 5%) to the Wu-Cohen functional based estimates available for $KNbO_3$ and $BaTiO_3$ [102, 120]. We consider local modes with Ti and Nb centered atomic displacements (at Γ, X, M and R points) to study the phase transitions in $BaTiO_3$ and $KNbO_3$ [133]. However, Pb centered local modes (at Γ, X, M and R points) have been used here to study the phase transition in $PbTiO_3$ [28]. For studying phase transitions, we use the eigenvalues of doubly-degenerate modes with X_5 (X_5' mode for $PbTiO_3$) and M_5' (M_5' mode for $PbTiO_3$) symmetries, nondegenerate modes with X_1 (X_2' mode for $PbTiO_3$) and M_3' (M_2'

mode for $PbTiO_3$) symmetries and triply-degenerate mode with R_{25}' (R_{15} mode for $PbTiO_3$) symmetry of $KNbO_3$ and $BaTiO_3$. We also take into account one Pb-based optical phonon mode at $(110)\frac{\pi}{2a}$ point of $PbTiO_3$. The local (κ_2) and short-range interaction parameters (j_1,...,j_7) are determined by using the eigenvalues (ω's) of these selected phonon modes and solving the linear Eq. as given in Refs. [28,102,104].

The total harmonic interaction (long- and short-range) matrix $\tilde{\Phi}^{quad}(k)$ is analyzed using FERAM [102, 114] to get the model phonon dispersion of $BaTiO_3$ (see Figure 4.6), which is similar to the dispersion obtained in earlier simulations using WC-GGA-based parameters [102]. The short-range interaction gives the most unstable mode at the X point (see Figure 4.6a). The dipole-dipole long-range interaction term results in a cell-doubling state due to the strongest instability at the M point [113]. The long-range dipole-dipole interaction splits the longitudinal and transverse optical phonon modes at the Γ point (see Figure 4.6b) and the splitting in ω is proportional to Z^{*2}/ϵ_∞. However, the competing short and long-range interactions together give the strongest instability at the Γ point. The short-range interaction parameters of $BaTiO_3$, $PbTiO_3$ and $KNbO_3$ are given in TABLE 4.7. For $BaTiO_3$, the short-range interaction parameters are comparable to the parameters based on earlier calculations using WC-GGA. As LDA underestimates lattice constants, the local (κ_2) and short-range interaction parameters (j_2, j_5 and j_7) calculated earlier using LDA are different from our estimates. The short-range interaction parameters of $PbTiO_3$ obtained using SCAN are similar to the values obtained using LDA at the experimental lattice constant (partly justifying this approximation in Ref. [28]) [28, 134]. For $KNbO_3$, local (κ_2) and short-range interaction parameters (j_1, j_2 and j_4) are different from earlier theoretical results using WC-GGA [114].

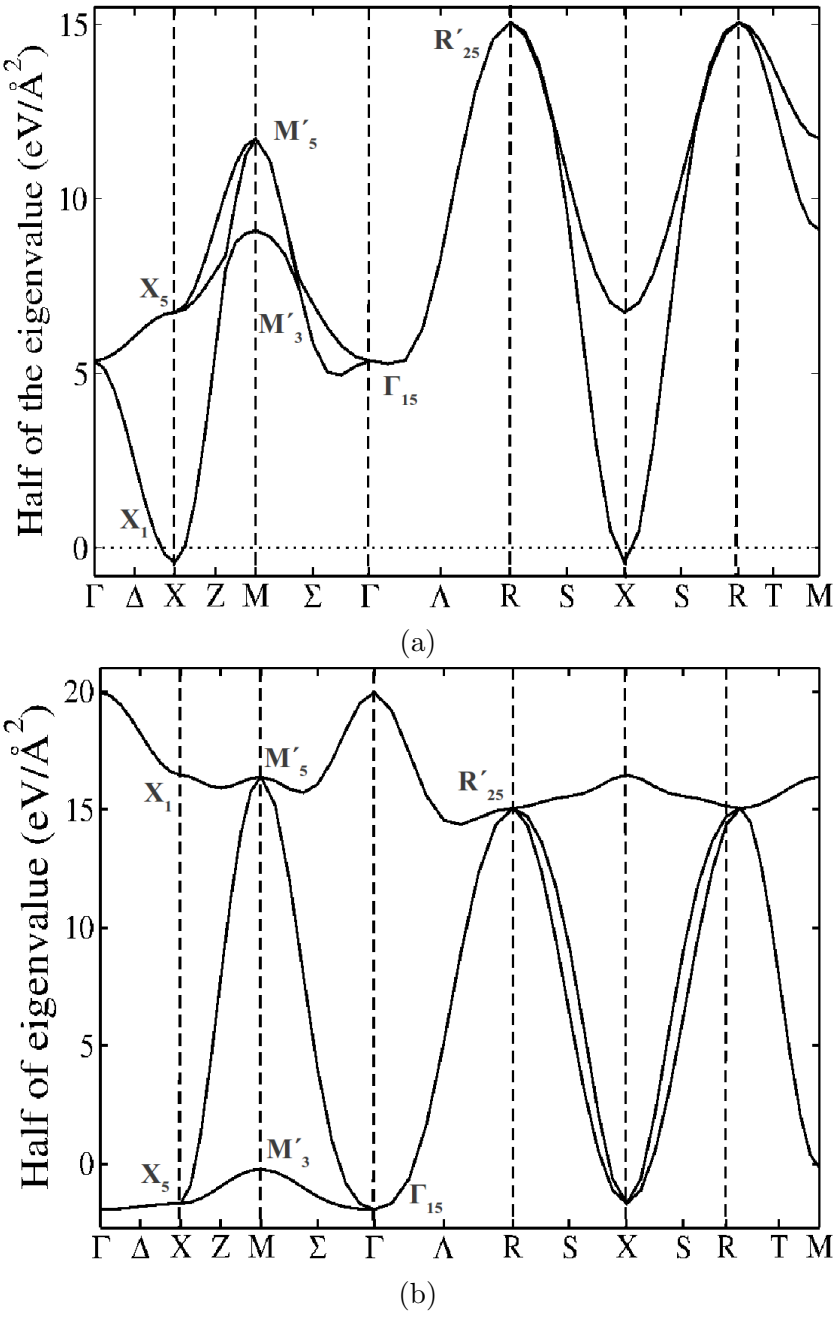

Figure 4.6: Half of the eigenvalues of (a) short-range interaction matrix and (b) total (long- and short-range) interaction matrix (Eq. (12) and (13) in Ref. [113]) along the high symmetry directions of $BaTiO_3$.

4.3.2.2 MD simulations

Using a SCAN-based parametrized effective Hamiltonian (truncating the local-mode self energy up to fourth-order terms in u in Eq. 4.4) [104,113], we perform heating-up

Table 4.7: Calculated local and short-range interaction parameters (in eV/Å^2) of $BaTiO_3$, $PbTiO_3$ and $KNbO_3$ in comparison with earlier theoretical results determined using LDA [28, 102, 134] and WC-GGA functionals [102, 114].

Compound	parameter	SCAN	LDA [28, 102, 134]	WC-GGA [102, 114]
$BaTiO_3$	κ_2	8.31	5.52	8.53
	j_1	-2.54	-2.65	-2.08
	j_2	-0.82	3.906	-1.12
	j_3	0.78	0.90	0.68
	j_4	-0.52	-0.79	-0.61
	j_5	0.0	0.56	0.0
	j_6	0.32	0.36	0.27
	j_7	0.0	0.18	0.0
$PbTiO_3$	κ_2	1.36	1.17	
	j_1	-1.36	1.17	
	j_2	4.84	-1.35	
	j_3	0.45	4.98	
	j_4	-0.11	0.22	
	j_5	0.60	-0.018	
	j_6	-0.09	-0.083	
	j_7	-0.05	-0.204	
$KNbO_3$	κ_2	10.06		11.42
	j_1	-5.06		-3.27
	j_2	1.87		-1.15
	j_3	1.09		1.10
	j_4	0.07		-0.66
	j_5	0.0		0.0
	j_6	0.43		0.30
	j_7	0.0		0.0

and cooling-down molecular dynamics simulations for $BaTiO_3$, $PbTiO_3$ and $KNbO_3$ to estimate T_C's. We define T_C for the phase transition P↔Q to be the mean of the transition temperatures for P→Q and Q→P. Simulated lattice parameters of these compounds as a function of temperature are presented in Figure 4.7. For $BaTiO_3$ and $KNbO_3$, we find three transitions: from cubic (C) to tetragonal (T), from tetragonal (T) to orthorhombic (O) and from orthorhombic (O) to rhombohedral

(R), which are consistent with the experimental observations [130, 135]. We find a single structural transition from cubic to tetragonal phase in $PbTiO_3$.

Our predicted transition temperatures of $BaTiO_3$ (see TABLE 4.8) are T_C (C↔T) = 213 K, T_C (T↔O)=141 K and T_C (O↔R)=111 K (see Figure 4.7a). T_C's of $BaTiO_3$ are underestimated by up to 65% with respect to the experimental transition temperatures [135]. However, our T_C's are 45% higher than earlier results obtained using LDA at zero pressure [102]. The accurate determination of total energy surfaces using SCAN gets reflected in the estimates of the transition temperatures. The rhombohedral to orthorhombic transition temperature is improved compared to earlier LDA and WC-GGA results at zero pressure [102]. The T_C's of the transitions from orthorhombic phase to tetragonal phase and tetragonal to cubic phase are 29% lower than the T_C's obtained with parameters obtained using the WC-GGA functional at zero pressure [102]. The $\boldsymbol{c/a}$ ratio of the tetragonal phase obtained using the SCAN-based parametrized effective Hamiltonian is 1.009 at 150 K which agrees very well with the experimental value (1.01) [107]. Earlier MD simulations using the WC-GGA-based parameters gave $\boldsymbol{c/a}$ ratio of the tetragonal phase (1.017 at 155 K) higher than the experimental value [102, 107]. It has been observed from earlier results that the tetragonal to cubic transition temperature changes drastically by the application of negative pressure, whereas the two other T_C's do not depend strongly on pressure. As our calculated strain-phonon coupling parameters are distinct from these in earlier works (B_{1xx}=-185.33 eV/Å^2 and B_{1yy}=-3.28 eV/Å^2) using the WC-GGA functional, the transition temperatures estimated with these two functionals are different [102].

Our estimated three transition temperatures (see TABLE 4.8) of $KNbO_3$ (O↔R =160 K, T↔O=225 K and C↔T=540 K) using the SCAN-based parameters (see Figure 4.7b) are underestimated compared to the experimental T_C's (O↔R=210 K, T↔O=488 K and C↔T=701 K) with largest error for T↔O transition [130].

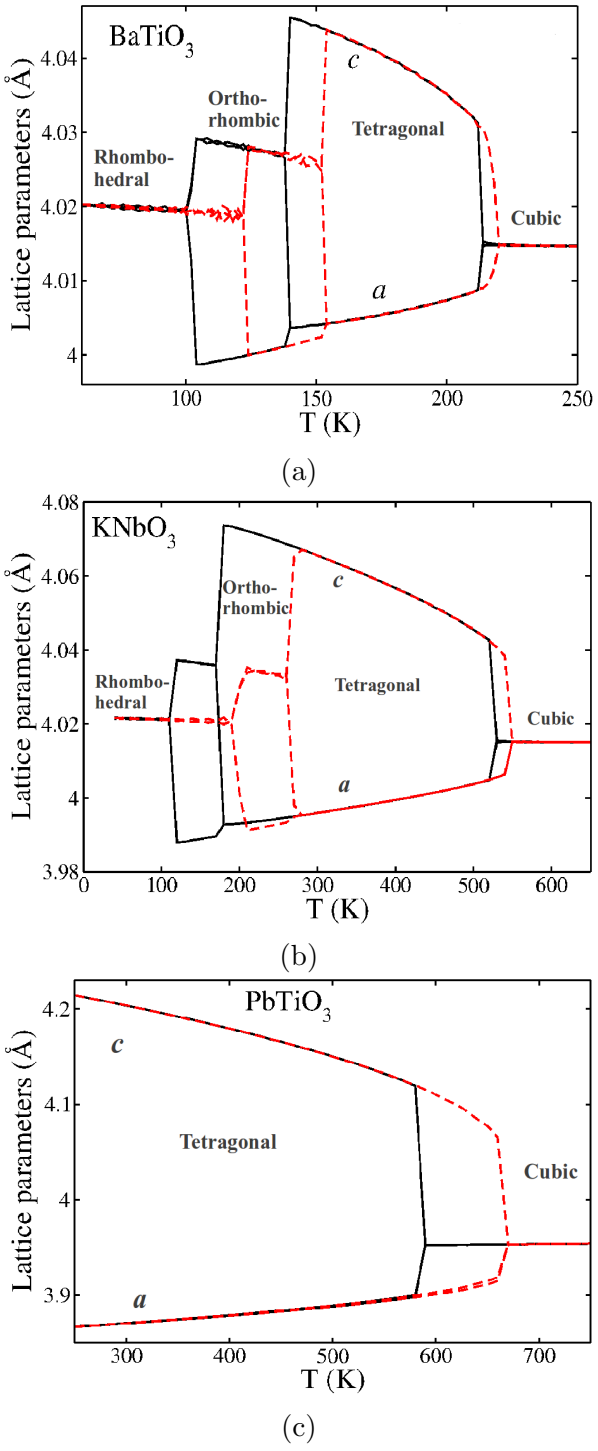

Figure 4.7: Simulated temperature dependence of lattice parameters of (a) $BaTiO_3$, (b) $KNbO_3$ and (c) $PbTiO_3$ at zero pressure. Red (dashed) and black (solid) lines represent heating and cooling curves respectively.

Values of T_C (T↔O) and T_C (O↔R) calculated here are slightly underestimated compared to earlier LDA results at the experimental lattice constant [136]. However, our calculated T_C (C↔T) is much larger compared to earlier LDA results at the experimental lattice constant [136]. On the other hand, our predicted transition temperatures are lower than the calculated T_C's using the WC-GGA functional at zero pressure [114]. The optimized lattice parameter of cubic $KNbO_3$ using SCAN is similar to the earlier computed value using the WC-GGA functional [114]. However, the inclusion of higher-order (greater than 4) on-site anharmonic coupling parameters, drastically different strain-phonon coupling parameters (B_{1xx}=-220.45 eV/Å^2 and B_{1yy}=31.35 eV/Å^2) in earlier WC-GGA calculations result in different values of T_C's compared to our estimated values [114]. We must note that application of negative pressure (using WC-GGA based effective Hamiltonian for $BaTiO_3$ and $KNbO_3$) does not affect the two lowest structural transition temperatures (O↔R and T↔O), whereas only T_C (C↔T) is a strong function of pressure [102,114]. The WC-GGA functional has been constructed with a particular focus on ferroelectric materials [102,109]. On the other hand, the SCAN meta-GGA functional is universal as it is applicable for all diversely bonded materials but might fail to determine precisely one specific property of a particular type of material. However, SCAN removes the typical error in estimating T_C's arising from the underestimation of lattice constant.

For $PbTiO_3$, we find a cubic to tetragonal phase transition at 630 K (see Figure 4.7c), which is slightly lower than the experimental T_C = 763 K (see TABLE 4.8). However, our predicted T_C is close to earlier calculated[‡] T_C (635 K) based on LDA parameters at the experimental lattice constant [28]. The tetragonal $\boldsymbol{c/a}$ ratio at 0 K (obtained by extrapolating lattice parameters) is 1.104 which is overestimated

[‡]Model Hamiltonian based on LDA parameters (at theoretical lattice constant) gives ferroelectric T_C of 510 K. Wojdel *et al.*, Journal of Physics: Condensed Matter 25, 305401 (2013)

compared to the experimental value (1.071 at 0 K) [107]. It is clear that SCAN-based predictions of the transition temperatures of the three oxides improve over those of LDA-based parameters [28, 134].

Table 4.8: Estimated T_c's of $BaTiO_3$, $PbTiO_3$ and $KNbO_3$ in comparison with earlier theoretical [28, 102, 134] and experimental T_C's [114, 130, 135–137].

Compound	exchange-correlation functional	R↔O	O↔T	T↔C
$BaTiO_3$	SCAN	111 K	141 K	213 K
	SCAN (including anharmonic coupling between phonons)	230 K	278 K	375 K
	LDA, 0.0 GPa [102]	95 K	110 K	137 K
	LDA, -5.0 GPa [102]	210 K	245 K	320 K
	WC-GGA, 0.0 GPa [102]	102 K	160 K	288 K
	WC-GGA, -2.0 GPa [102]	117 K	218 K	408 K
	WC-GGA, -0.005T GPa [102]	103 K	187 K	411 K
	Exp. [135]	183 K	278 K	403 K
$KNbO_3$	SCAN	160 K	225 K	540 K
	SCAN (including anharmonic coupling between phonons)	160 K	230 K	565 K
	LDA (experimental lattice constant) [136]	210 K	260 K	370 K
	WC-GGA [114], 0.0 GPa	177 K	310 K	660 K
	WC-GGA [114], -0.001T GPa	175 K	323 K	703 K
	Exp. [130]	210 K	488 K	701 K
$PbTiO_3$	SCAN			630 K
	SCAN (including anharmonic coupling between phonons)			675 K
	LDA (experimental lattice constant) [28, 134]			635 K
	Exp. [137]			763 K

The discrepancies between our calculated T_C's and experimental T_C's have a contribution from the neglect of the anharmonic coupling between the soft mode and higher energy phonon modes, as the error in lattice constant has been minimized using the SCAN meta-GGA functional. The effect of including anharmonic coupling between soft and higher-energy modes on finite temperature properties will be discussed in the following section.

4.3.3 Anharmonic coupling between phonons

We find that the depths of the double-well potentials of $BaTiO_3$, $PbTiO_3$ and $KNbO_3$ (along the [001] direction) obtained directly from DFT calculations (E_{cubic}-$E_{tetragonal}$=25 meV/unit cell for $BaTiO_3$, 123 meV/unit cell for $PbTiO_3$ and 47 meV for $KNbO_3$) and from the effective Hamiltonian (Eq. 4.2a) written as a fourth-order expansion (16 meV/unit cell for $BaTiO_3$, 95 meV/unit cell for $PbTiO_3$ and 43 meV for $KNbO_3$) are different. This difference in energies highlights the presence of anharmonic coupling between the soft mode and other higher-energy optical phonon modes.

To identify higher-energy optical modes responsible for the phase transition, we define a vector given as:

$$\vec{S} = \vec{f} - (\vec{f}.\hat{e}_{soft})\hat{e}_{soft}, \tag{4.5}$$

where $\hat{e}_{soft}$ is the soft mode eigenvector and $\vec{f}$ is the ferroelectric distortion given as atomic displacement vector from the cubic to tetragonal phase. Phonon modes having Γ_{15} symmetry with frequencies 182 cm^{-1} (for $BaTiO_3$), 140 cm^{-1} (for $PbTiO_3$) and 207 cm^{-1} (for $KNbO_3$) show strong overlap (0.79 for $BaTiO_3$, 0.55 for $PbTiO_3$ and 0.52 for $KNbO_3$) with $\hat{S}$. We find higher-energy optical phonon modes with Γ_{15} symmetry (478 cm^{-1} for $BaTiO_3$, 530 cm^{-1} for $PbTiO_3$ and 483 cm^{-1} for $KNbO_3$) contributing sizably to the ferroelectric distortion of the cubic phase.

To model the lowest-order coupling between these Γ_{15} modes, we write the total energy (along the [001] direction) as a function of soft mode (u), higher-energy modes v_1 (182 cm^{-1} for $BaTiO_3$, 140 cm^{-1} for $PbTiO_3$ and 207 cm^{-1} for $KNbO_3$) and v_2 (478 cm^{-1} for $BaTiO_3$, 530 cm^{-1} for $PbTiO_3$ and 483 cm^{-1} for $KNbO_3$) by expanding it as a symmetry-invariant Taylor series expansion up to eighth-order in u

and second-order in v_1 and v_2 with respect to the cubic phase using ISOTROPY [91]:

$$E(u, v_1, v_2) = \kappa u^2 + \alpha' u^4 + k_1 u^6 + k_4 u^8 + \kappa_{v_1} v_1^2 + e_1 u^3 v_1 + f_1 u^2 v_1^2 + \kappa_{v_2} v_2^2 + e_2 u^3 v_2 + f_2 u^2 v_2^2. \tag{4.6}$$

We have not considered the cubic coupling terms in higher energy phonon modes as their contributions to the energy are less significant. e_1 and e_2 have been determined by projecting forces (arising due to the freezing of the soft mode) on v_1 and v_2 as shown in Figure 4.8a and Figure 4.8b respectively. f_1 and f_2 coupling terms have been evaluated by calculating the eigenvalues of v_1 and v_2 modes as a function of amplitude of the soft mode (u), shown in Figure 4.8c and Figure 4.8d respectively. Such anharmonic coupling between the soft mode and higher-energy optical phonon modes was ignored in the earlier model Hamiltonian (Eq. 4.4).

Minimizing the total energy (Eq. 4.6) with respect to v_1 and v_2, the resulting $v_{1,min}$ and $v_{2,min}$ are:

$$v_{1,min} \approx -\frac{e_1 u^3}{2k_{v_1}}(1 - \frac{f_1}{\kappa_{v_1}} u^2), \tag{4.7a}$$

$$v_{2,min} \approx -\frac{e_2 u^3}{2k_{v_2}}(1 - \frac{f_2}{\kappa_{v_2}} u^2). \tag{4.7b}$$

The renormalized form of the total energy as a function of u is obtained by substituting $v_{1,min}$ and $v_{2,min}$ in Eq. 4.6:

$$\begin{aligned} E(u) &= \kappa u^2 + \alpha' u^4 + (k_1 - \frac{e_1^2}{4\kappa_{v_1}} - \frac{e_2^2}{4\kappa_{v_2}}) u^6 + (k_4 - \frac{e_1^2 f_1}{4\kappa_{v_1}^2} - \frac{e_2^2 f_2}{4\kappa_{v_2}^2}) u^8, \\ &= \kappa u^2 + \alpha' u^4 + k_1' u^6 + k_4' u^8. \end{aligned} \tag{4.8}$$

The fourth-order coupling terms between phonon modes modify the terms associated with sixth- and eighth-order in soft-mode displacement.

The expressions for total energies as a function of u along [110] and [111] directions are [102]:

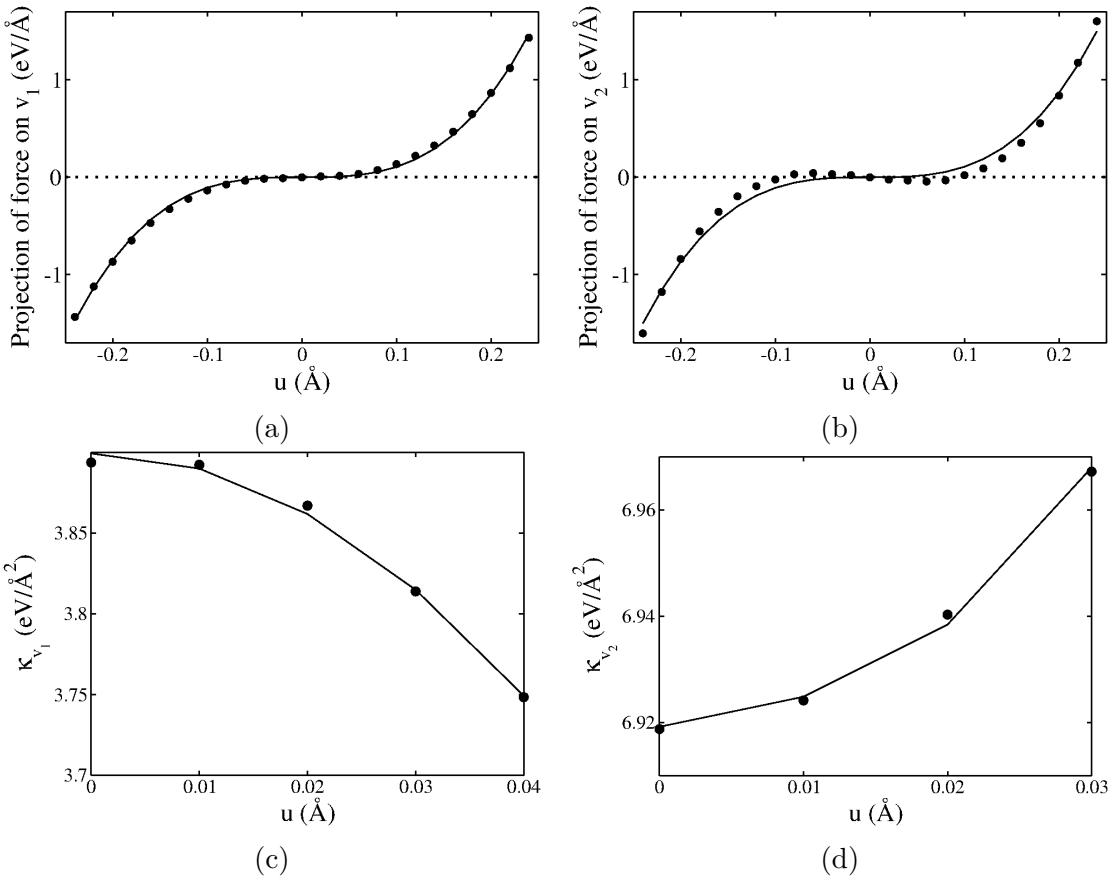

Figure 4.8: Projection of forces arising due to the freezing of soft mode (a) on v_1 and (b) v_2 modes of $BaTiO_3$. Eigenvalues of (c) v_1 and (d) v_2 modes as a function of soft mode amplitude (u).

$$E_{110}(u) = \kappa u^2 + (\alpha' + \frac{1}{4}\gamma')u^4 + (k_1' + \frac{1}{4}k_2)u^6 + k_4' u^8, \tag{4.9a}$$

$$E_{111}(u) = \kappa u^2 + (\alpha' + \frac{1}{3}\gamma')u^4 + (k_1' + \frac{2}{9}k_2 + \frac{1}{27}k_3)u^6 + k_4' u^8. \tag{4.9b}$$

For $BaTiO_3$, the values of the coupling constants are 3.95 eV/Å^2 (k_{v_1}), 6.85 eV/Å^2 (k_{v_2}), 107.91 eV/Å^4 (e_1), 107.22 eV/Å^4 (e_2), -92.74 eV/Å^4 (f_1), 52.75 eV/Å^4 (f_2), -325.24 eV/Å^6 (k_1) and 2196.59 eV/Å^8 (k_4). We have also determined the sixth-order terms k_2 (407.79 eV/Å^6) and k_3 (1286.21 eV/Å^6) to define the potential energy surface for distortions along [110] and [111] directions (using Eq. 4.9a and 4.9b). When the double-well energy functions (along [111] and [001] directions) are fitted

with an eighth-order polynomial, the values of α and γ change to 126.18 eV/Å^4 and -171.69 eV/Å^4 respectively. However, the addition of sixth- and eighth-order terms (without including coupling between soft polar and higher energy modes) does not affect the well depth and transition temperatures. The calculated energy difference between cubic and tetragonal phases using Eq. 4.8 is 24 meV, which is closer to the value obtained from DFT calculations (25 meV).

To investigate the effect of changing the depth of double-well potential energy on finite temperature properties, we calculate the transition temperatures of $BaTiO_3$ considering our generalised effective Hamiltonian (Eq. 4.8, 4.9a and 4.9b). Our simulated three transition parameters (see TABLE 4.8) using the new parameters (k_1' and k_4') are 230 K (O↔R), 278 K (R↔T) and 375 K (T↔C) as shown in Figure 4.9a. The tetragonal to cubic transition temperature increases by 57% from the value (217 K) obtained without including the coupling between soft mode and higher energy modes. The simulated value of $\boldsymbol{c/a}$ ratio at 300 K of the tetragonal phase is 1.014 which is slightly overestimated compared to the experimental value (1.010), as expected [107]. Here, we did not include the anharmonic coupling between phonons to modify k_2 and k_3 parameters, which will precisely determine the depth of the energy well along [111] and [110] directions. This leads to the slight overestimation of two lower T_C's.

Similarly, the depth of the potential well of the tetragonal state in the model of $KNbO_3$ increases by 9 meV (from the value of 43 meV obtained using Eq. 4.2a) after including the effects of anharmonic coupling between soft-mode and higher-energy phonons (k_{v_1}=3.27 eV/Å^2, k_{v_2}=7.17 eV/Å^2, e_1=0.2 eV/Å^4, e_2=-139.2 eV/Å^4, f_1=-135.5 eV/Å^4, f_2=-138.3 eV/Å^4, k_1=-464.3 eV/Å^6 and k_4=1658 eV/Å^8, k_2=550 eV/Å^6, k_3=1347 eV/Å^6). It is slightly overestimated compared to the energy well depth calculated using DFT calculations (47 meV). The values of α and γ changes to 127 eV/Å^4 and -166 eV/Å^4 (which does not affect T_C's when anharmonic coupling

between phonons is not included), when the double-well energy functions are fitted with an eighth-order polynomial. The calculated values of T_C's of $KNbO_3$ using our generalised model Hamiltonian with SCAN-based parameters are T_C (C↔T) = 565 K, T_C (T↔O)=230 K and T_C (O↔R)=160 K (see TABLE 4.8 and Figure 4.9b). We notice an increase in the tetragonal to cubic transition temperature by 25 K from the value (540 K) calculated earlier here, while the other two T_C's almost remain unaltered.

Furthermore, we have calculated anharmonic coupling parameters between soft mode and other two optical phonon modes (ω_{v_1}=140 cm^{-1} and ω_{v_2}=530 cm^{-1}) with Γ_{15} symmetry (κ_{v_1}=2.70 eV/Å^2, κ_{v_2}=7.91 eV/Å^2, e_1=41.02 eV/Å^4, e_2=28.61 eV/Å^4, f_1=-12.75 eV/Å^4, f_2=-18.27 eV/Å^4, k_1=-1.97 eV/Å^6 and k_4=13.64 eV/Å^8) of $PbTiO_3$. The value of α changes slightly (6.52 eV/Å^4), when the potential energy surface along [001] direction is fitted with an eighth-order polynomial and it does not affect the well depth and transition temperature. The evaluated energy difference between cubic and tetragonal phases using Eq. 4.8 is 151 meV, which is slightly overestimated compared to the value (123 meV) obtained using DFT calculation. After including anharmonic couplings between soft and higher-energy modes, We find an increase in T_C to 675 K (see Figure 4.9c) from the value (630 K) calculated earlier here (see TABLE 4.8). The $\boldsymbol{c/a}$ ratio at 0 K (obtained by extrapolating lattice parameters) is 1.053, which is in close agreement with the experimental value (1.071 at 0 K), but some errors are expected from approximately integrating out the higher-energy optic phonons [107]. Overall, our model based on the parameters calculated using SCAN precisely determines the depth of the potential well along the [001] direction, and gives a better estimation of T_C's and $\boldsymbol{c/a}$ ratios of the tetragonal phases of $BaTiO_3$ and $PbTiO_3$.

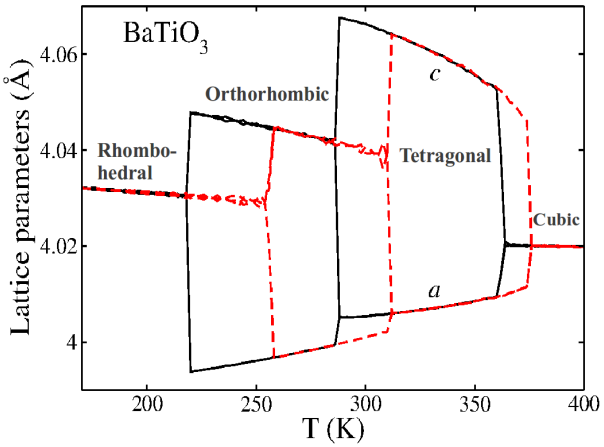

(a)

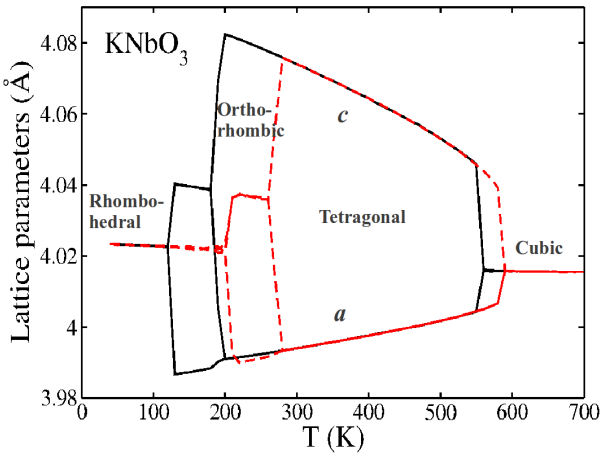

(b)

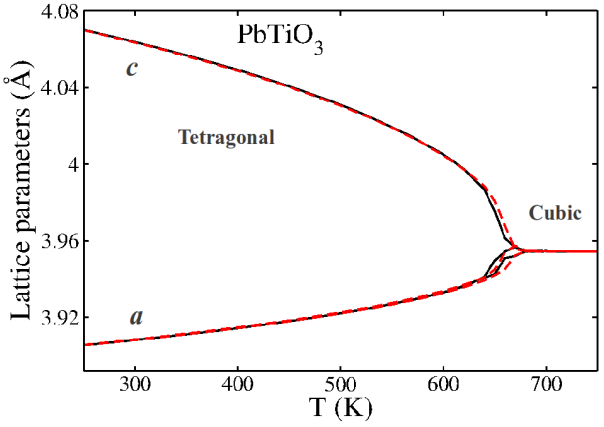

(c)

Figure 4.9: Estimated T_C's of (a) $BaTiO_3$, (b) $KNbO_3$ and (c) $PbTiO_3$ including the fourth-order coupling between soft and higher energy phonon modes. Heating and cooling curves are indicated by red (dashed) and black (solid) lines respectively.

4.4 Summary

We demonstrated consistent improvement in theoretical prediction of structural parameters of the eight cubic perovskite oxides using the SCAN meta-GGA functional relative to LDA or GGA. In addition, estimates of band gaps of perovskite oxides typically increase and modestly improve over the earlier estimates of band gaps obtained with LDA. Accurate structural parameters given by the SCAN meta-GGA functional allow estimation of more realistic total energy surfaces of cubic perovskites as a function of soft-mode amplitude, which are relevant to the temperature-dependent structural phase transition. Our predicted zone centre optical phonon (stable modes) frequencies using the SCAN meta-GGA functional are in better agreement with the experimentally observed frequencies compared to the values using other functionals. Elastic constants and eigenvectors of soft modes are weakly dependent on the choice of exchange-correlation energy functional. For $BaTiO_3$, $PbTiO_3$ and $KNbO_3$, the strain phonon coupling parameter B_{4yz} and anharmonic coupling terms and eigenvalues of soft modes get significantly altered by the SCAN meta-GGA exchange-correlation functional. The depths of the double-well energy surfaces of the polar distortions along [001], [110] and [111] directions determined using the SCAN meta-GGA functional are notably enhanced relative to the depth obtained earlier using LDA.

As a consequence of these improvements, estimates of T_C's of all the structural transitions in $BaTiO_3$ and $PbTiO_3$ are closer to experiment than those of the earlier LDA results. In particular, analysis of temperature-dependent transitions can be carried out with the SCAN meta-GGA based energy surface without having to use negative pressure to compensate for error in lattice constants (e.g., in LDA). We have quantified the consequences of truncation of the subspace of the effective Hamiltonian using the lowest-order coupling between soft and higher energy optic

modes with Γ_{15} symmetry to estimation of T_C's. The fourth-order anharmonic coupling between the soft polar mode and higher-energy optical modes in $BaTiO_3$ and $PbTiO_3$ causes the increase in the depth of the potential well, and consequently enhances the estimated T_C's (Figure. 4.7, 4.9 and TABLE 4.8). At the interfaces in hetero-structures or superlattices based on perovskite oxides, details of atomic-scale structure depend on the mismatch between lattice constants, and electronic band offsets depend on band-gaps. Since estimates of both lattice constants and band-gap are consistently improved with SCAN meta-GGA calculations, we expect SCAN meta-GGA to be very effective in simulations of perovskite hetero-structures.

Chapter 5

Lanthanide ruthenium perovskite oxides: electronic properties

5.1 Introduction

Transition metal oxides exhibit a variety of electronic properties such as superconductivity, colossal magnetoresistance, charge, orbital and spin orderings [138]. Transition metals drawn from the $4d$ series are particularly interesting as $4d$ orbitals are spatially extended than $3d$ orbitals and emergent behaviors arise as a result of competition between Coulomb, magnetic exchange and spin-orbit interactions. The extensively studied oxides with $4d$ electrons are Ru-based oxides due to their unusual electronic and magnetic properties [139]. The layered perovskite Sr_2RuO_4 is a p-wave superconductor [140]. A magnetic field induced quantum criticality in itinerant metamagnet $Sr_3Ru_2O_7$ has been observed experimentally [141]. $SrRuO_3$ is an itinerant ferromagnet* whereas Ca_2RuO_4 is a Mott insulator [140,142]. These oxides contain Ru atom in the +4 oxidation state. However, Ru can also exist in +5 (double perovskite Ln_2LiRuO_6, rutheno-cuprate superconductors $RuSr_2(Ln,Ce)_2Cu_2O_{10}$ and

*Miao *et al.*, Journal of Physics: Condensed Matter 26, 035401 (2014) and Journal of Physical Chemistry C 120, 9112 (2016)

pyrochlores $A_2Ru_2O_7$ (A=Cd and Hg)), +6 (hexagonal perovskite $Ba_3NaRu_2O_9$) and +7 ($KRuO_4$) oxidation states [143–147]. In contrast, the existence of oxides with Ruthenium in +2 and +3 oxidation states has been scarce or almost unknown.

However, it has been observed recently in experiments that Ru exists in +3 state in $LnRuO_3$ orthorhombic perovskites (Ln=La, Pr, Nd, Sm, Eu, Gd, Tb and Y), which have been synthesized and characterized using X-ray and neutron diffraction experiments [148]. $LaRuO_3$ is accessible through synthesis at ambient pressure, whereas the other perovskites stabilize at high pressure [148]. Ru site in $LnRuO_3$ has 7-11% vacancies and all lanthanide ruthenium oxides are semiconducting in nature [148]. The Ru deficient orthorhombic perovskites ($LnRu_{1-\delta}O_3$) contain a mixture of Ru^{3+} and Ru^{4+} states with an average ruthenium oxidation state in the range from +3.3 to +3.5. The presence of cation vacancies highlights the tendency of Ru^{3+} to disproportionate in oxide environments into Ru^{4+} and Ru metal [148]. Experimentally, spin ordering transitions in $LnRu_{1-\delta}O_3$ perovskites are not observed down till 2 K [148]. It has been predicted from experiments that the paramagnetic behavior and semiconductivity of $LnRu_{1-\delta}O_3$ is a consequence of disorder induced by cation vacancy [148]. First-principles density functional calculations are effective in capturing the local changes in electronic and structural properties introduced by cation vacancies. However, validations and understanding of the experimental findings on Ru deficient $LnRuO_3$ perovskites using first-principles theoretical analysis have not been done so far.

In this chapter, we determine electronic structures and energetics of stoichiometric and nonstoichiometric $LaRuO_3$ and $YRuO_3$ using first-principles calculations based on density functional theory that includes Hubbard U and the spin-orbit coupling.

5.2 Methods

We determined electronic structure of lanthanide ruthenium oxides ($LaRuO_3$ and $YRuO_3$) from first-principles calculations within density functional theory as implemented in QUANTUM ESPRESSO package [86]. We treated exchange-correlation energy functional within a generalized gradient approximation (GGA) in the Perdew-Burke-Ernzerhof parametrized form [34] and included on-site correlations with Hubbard U parameters of 2.0 eV and 3.0 eV [149]. We used ultrasoft pseudopotentials [150]. To introduce 12% vacancies at La (in $LaRuO_3$) and Ru (in $LaRuO_3$ and $YRuO_3$) sites, we considered a doubled unit cell ($\sqrt{2} \times 1 \times \sqrt{2}$ supercell) with cell vectors ($\boldsymbol{a}$,0,-$\boldsymbol{c}$), (0,$\boldsymbol{b}$,0) and ($\boldsymbol{a}$,0,$\boldsymbol{c}$), where $\boldsymbol{a}$,$\boldsymbol{b}$ and $\boldsymbol{c}$ are the orthrhombic cell parameters of $LaRuO_3$ and $YRuO_3$. Brillouin Zone integrations were sampled on 6×4×6 and 6×6×6 uniform meshes of k-points in calculations on bulk and supercell structures respectively. We used an energy cut-off of 30 Ry to truncate the plane wave basis used in the wavefunction representation and of 240 Ry in representation of charge density.

Electronic structure calculations of $LaRuO_3$ (without any cation vacancy) that include the spin-orbit coupling (SOC) and Hubbard U correction were carried out with VASP package [110]. We treated valence and core electrons here using the PAW method [112]. A plane wave energy cutoff of 400 eV and 6×4×6 uniform mesh of k-points were used. Exchange correlation energy functional was treated with a GGA functional in the Perdew-Burke-Ernzerhof parametrized form [34].

5.3 Results and discussion

5.3.1 Stoichiometric $LnRuO_3$

The orthorhombic unit cell of lanthanide ruthenium oxides ($LaRuO_3$ and $YRuO_3$) contains four formula units, i.e., 20 atoms. Ru atom is surrounded by two apical oxygen atoms (O2) and four equatorial oxygen atoms (O1) forming an octahedral coordination (see Figure 5.1). These RuO_6 octahedra are linked with the corner sharing

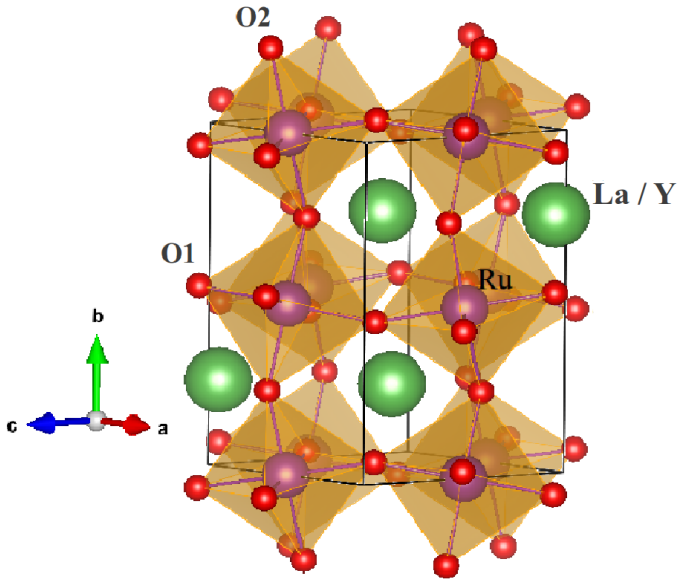

Figure 5.1: Crystal structure of lanthanide (La/Y) ruthenium oxide.

apical (O2) and equatorial (O1) oxygen atoms along the $\boldsymbol{b}$ axis and in the $\boldsymbol{ac}$ plane respectively. We consider orthorhombic $LaRuO_3$ and $YRuO_3$ with ferromagnetic and antiferromagnetic (G-type) ordering of spins at Ru sites in our electronic structure calculations. We used experimental lattice parameters ($\boldsymbol{a}(LaRuO_3)$=5.621 Å, $\boldsymbol{b}(LaRuO_3)$=7.866 Å, $\boldsymbol{c}(LaRuO_3)$=5.546 Å, $\boldsymbol{a}(YRuO_3)$=5.8057 Å, $\boldsymbol{b}(YRuO_3)$=7.5406 Å and $\boldsymbol{c}(YRuO_3)$=5.2008 Å) in all our calculations and relaxed the atomic positions to minimize the total energy [148].

5.3.1.1 Effect of Hubbard U

Our first-principles calculations with Hubbard U=0 show that ferromagnetic state of $LaRuO_3$ is energetically lower than the antiferromagnetic state by 28 meV/f.u., corresponding to the exchange coupling strength of -4.6 meV. Ferromagnetic state of $LaRuO_3$ is half-metallic with a band gap of 1.06 eV in the up-spin channel (see Figure 5.2). The valence band in both spin channels is contributed mainly by Ru 4d, O 2p orbitals, while the conduction bands are contributed by La 5d and Ru 4d orbitals. The electronic states at the Fermi level in the down-spin channel are composed of mainly Ru 4d orbitals. Our estimation of the magnetic moment of Ru atom is 0.97 μ_B, confirming its oxidation state of 3+. In contrast, electronic structure of antiferromagnetic phase of $LaRuO_3$ has a metallic character. The electronic states (in both spin channels) in energy range between -7.1 eV and -2.3 eV is composed of Ru 4d, O 2p orbitals (see Figure 5.2). The conduction band is contributed by La 5d and Ru 4d orbitals, and the states at the Fermi level are contributed by Ru 4d orbitals. The estimated value of magnetic moment of Ru atom is 0.0 μ_B, which indicates essentially no exchange splitting, and need for a more refined analysis.

To get a realistic magnetic moment of Ru atom in the antiferromagnetic phase, we included the on-site correlations with Hubbard U parameter (U=2.0 eV and 3.0 eV). Upon inclusion of Hubbard U, the energy difference between the ferro- and antiferromagnetic states first increases to 38 meV/f.u. (U=2.0 eV) and decreases to 0.7 meV/f.u. (U=3.0 eV) as mentioned in TABLE 5.1. We find that the half-metallic character (see Figure 5.2) of ferromagnetic state remains unaltered upon introduction of on-site correlations U (U=2.0 eV and U=3.0 eV). However, the band gap in electronic spectrum of up-spin channel of the ferromagnetic state increases slightly to 1.13 eV (U=2.0 eV) and 1.19 eV (U=3.0 eV). Other features of the electronic structure of ferromagnetic phase remain the same.

The local magnetic moment of Ru atom in the ferromagnetic state of $LaRuO_3$

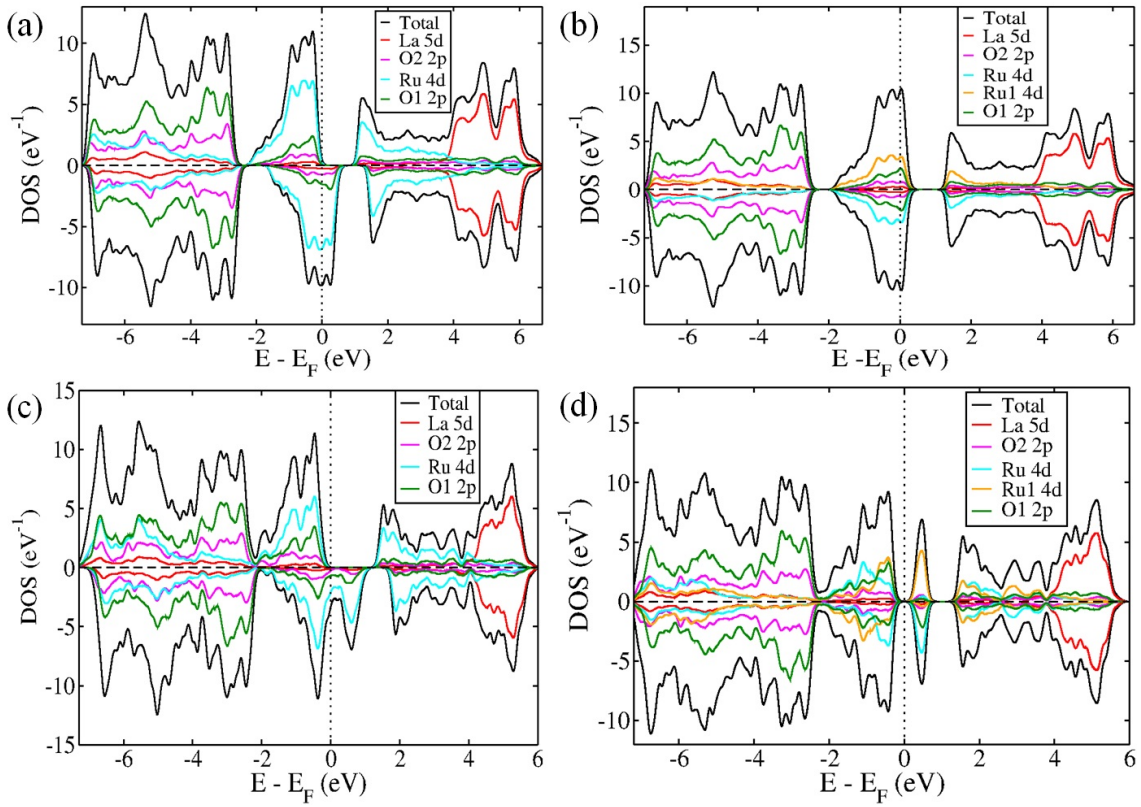

Figure 5.2: Spin-resolved electronic density of states of $LaRuO_3$: (a) with ferromagnetic ordering, (b) antiferromagnetic ordering in the absence of Hubbard U and (c) ferromagnetic and (d) antiferromagnetic orderings in the presence of Hubbard U parameter (U=3.0 eV). Ru1 atom has electrons with opposite spins compared to Ru in the antiferromagnetic state.

is not affected by Hubbard U parameter. Inclusion of on-site correlation (U=3.0 eV) results in semiconducting antiferromagnetic $LaRuO_3$, with a band gap of 0.42 eV (see Figure 5.2 and TABLE 5.1). The valence bands in both the spin channels are contributed mainly by O $2p$ and Ru $4d$ orbitals. Conduction band in up- and down-spin channels is contributed by La $5d$ and Ru $4d$ orbitals. The local magnetic moment of Ru atom is estimated to be 0.89 μ_B (U=3.0 eV), close to the experimental estimate [148].

For $YRuO_3$, we used the Hubbard U parameter of 3.0 eV to get a realistic magnetic moment of Ru atom. The antiferromagnetic state of $YRuO_3$ is energetically

lower than the ferromagnetic state by 3.2 meV/f.u. (see TABLE 5.1). Ferromagnetic state shows a "half-semiconducting" character with bandgaps of 1.48 eV and 0.27 eV in the up and down-spin channels (see Figure 5.3) respectively. The valence

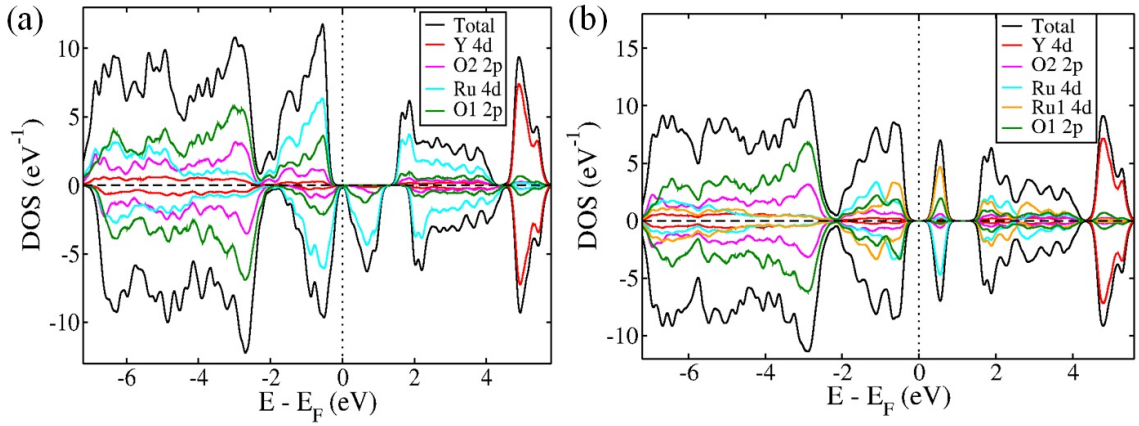

Figure 5.3: Spin-resolved electronic density of states of $YRuO_3$: (a) with ferromagnetic and (b) antiferromagnetic orderings with using Hubbard U parameter (U=3.0 eV). Ru1 atom has electrons with opposite spins compared to Ru in the antiferromagnetic state.

band in both the spin channels is contributed mainly by O $2p$ and Ru $4d$ orbitals, while the conduction band in both spin channels is contributed by Y $4d$ and Ru $4d$ orbitals. The local magnetic moment of Ru atom in the ferromagnetic state is 0.99 μ_B, confirming its oxidation state of 3+. Similar to the ferromagnetic state, antiferromagnetic state of $YRuO_3$ is semiconducting with a bandgap of 0.62 eV (see Figure 5.3). The valence band in both spin channels is contributed mainly by Ru $4d$ and O $2p$ orbitals and conduction band in both spin channels is contributed by Y $4d$ and Ru $4d$ orbitals. The local magnetic moment of Ru atom in the antiferromagnetic state is 0.94 μ_B, slightly larger than that in $LaRuO_3$ (0.89 μ_B). This is because Y^{3+} is more ionic than La^{3+} ion, as can be seen from the electronic density of states (see Figure 5.2 and Figure 5.3).

Next, we investigate the effect of spin-orbit coupling on the electronic properties of $LaRuO_3$.

Table 5.1: Our estimated bandgaps and energies (with respect to ferromagnetic state) and local magnetic moment of Ru atom (μ in the unit of μ_B) of ferromagnetic and antiferromagnetic states of lanthanide ruthenium oxides. The value of Hubbard U parameter is given inside the parenthesis.

Compounds	Methods	State	E (meV/f.u.)	$E_{g,\uparrow}$ (eV)	$E_{g,\downarrow}$ (eV)	μ
$LaRuO_3$	GGA	FM	0.0	1.06	0.0	0.99
		AFM	28.0	0.0	0.0	0.0
	GGA+U (2.0 eV)	FM	0.0	1.13	0.0	0.99
		AFM	38.0	0.095	0.095	0.79
	GGA+U (3.0 eV)	FM	0.0	1.16	0.0	0.99
		AFM	0.7	0.42	0.42	0.89
$YRuO_3$	GGA+U (3.0 eV)	FM	0.0	1.48	0.27	0.99
		AFM	-3.2	0.62	0.62	0.94

5.3.1.2 Effect of spin-orbit coupling

Inclusion of SOC in a calculation is found not to change the ordering of energies of magnetically ordered states (E_{AFM}-E_{FM}=16.2 meV/f.u.) in the absence of Hubbard U. However, the electronic structure changes: ferromagnetic and antiferromagnetic states of $LaRuO_3$ exhibit metallic character (see Figure 5.4). The valence band is contributed mainly by Ru 4d and O 2p orbitals, while the conduction band is contributed by La 5d and Ru 4d orbitals. The states at the Fermi level are contributed by Ru 4d orbitals. The local magnetic moments of Ru atom in the ferromagnetic and antiferromagnetic states are 0.71 μ_B and 0.32 μ_B respectively.

Including both SOC and Hubbard U (U=2.0 eV) in our calculations, we find that ferromagnetic state remains lower in energy by 32 meV/f.u. than the antiferromagnetic state. The antiferromagnetic state is semiconducting with a bandgap of 0.38 eV and the local magnetic moment of Ru atom increases to 0.68 μ_B (see Figure 5.4). On the other hand, ferromagnetic state remains metallic and the local magnetic moment of Ru atom increases to 0.76 μ_B (see Figure 5.4), which is more realistic and closer to the experimentally observed value [148]. Thus, SOC alone

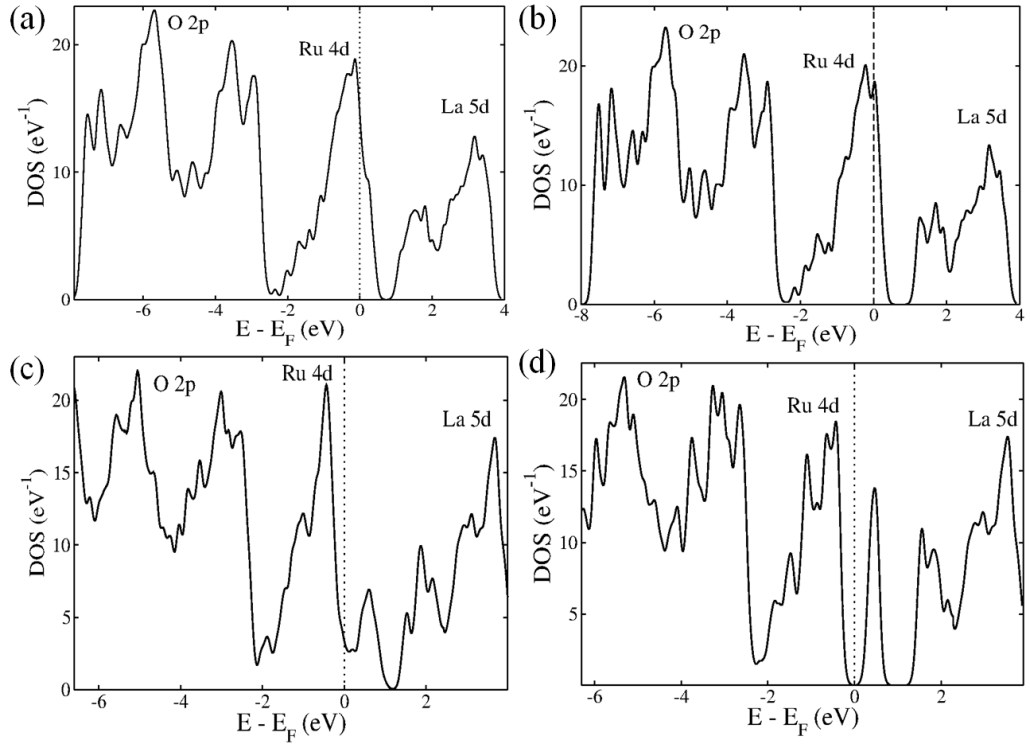

Figure 5.4: Electronic density of states of $LaRuO_3$ in the presence of spin-orbit coupling: (a) ferromagnetic, (b) antiferromagnetic states without using Hubbard U and (c) ferromagnetic and (d) antiferromagnetic states with using Hubbard U (U=2.0 eV).

does not give a realistic estimation of magnetic moment of Ru atom in the antiferromagnetic state. Hubbard U parameter is necessary in a calculation to capture the local magnetic moments correctly.

5.3.2 $LnRu_{1-\delta}O_3$

To explain the experimental finding of semiconducting properties [148], we introduce 12% Ru vacancies in $YRuO_3$ and $LaRuO_3$. We determined the electronic structure of $YRu_{0.88}O_3$ and $LaRu_{0.88}O_3$ using Hubbard U parameter as 3.0 eV (without including the spin-orbit coupling). In the presence of 12% Ru vacancies, the ferromagnetic state of $LaRuO_3$ remains lower in energy by 9.2 meV/f.u. (see TABLE 5.2) compared to the antiferromagnetic state. With weaker relative of stability of the ferromagnetic

state, Ru vacancies change the half-metallic character of the ferromagnetic state of $LaRuO_3$ to "half-semiconducting" phase by opening up a gap in the down-spin channel (0.19 eV) (see Figure 5.5). Antiferromagnetic state of $LaRu_{0.88}O_3$ also has a "half-semiconducting" character with a bandgap of 0.78 eV in the up-spin channel and 0.15 eV in the down-spin channel. In the spin-resolved electronic structure of these magnetic states, the valence band is contributed mainly by Ru 4*d*, O 2*p* orbitals, while the conduction band is contributed by La 5*d* and Ru 4*d* orbitals (see Figure 5.5).

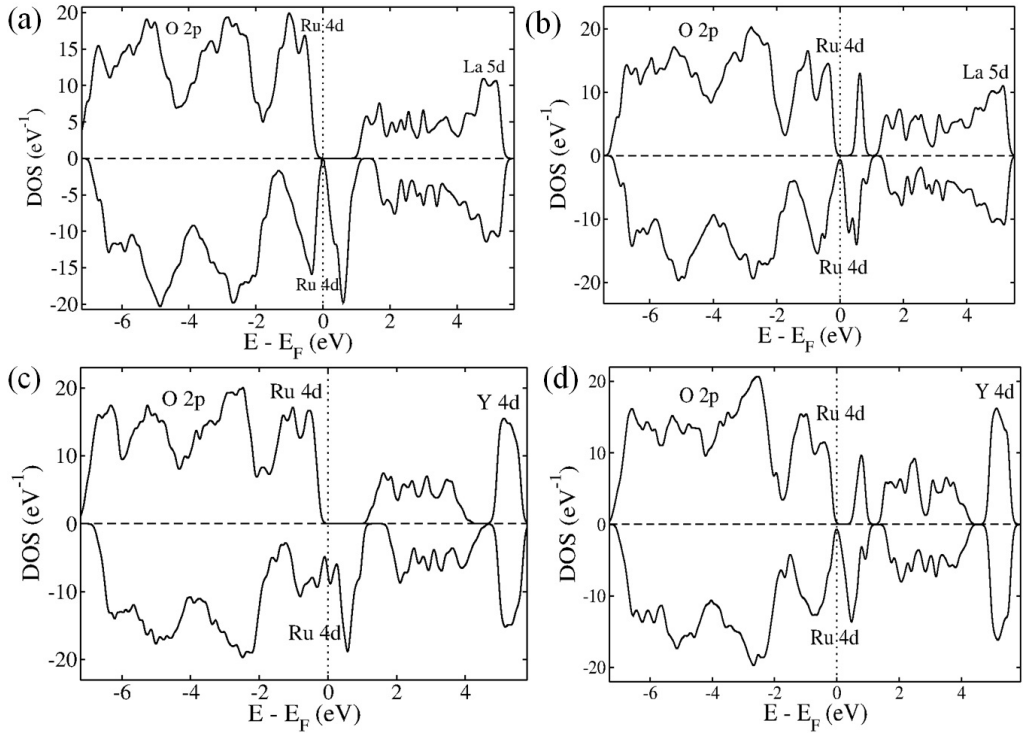

Figure 5.5: Spin-resolved electronic density of states with using Hubbard U (U=3.0 eV): (a) ferromagnetic $LaRu_{0.88}O_3$, (b) antiferromagnetic $LaRu_{0.88}O_3$, (c) ferromagnetic $YRu_{0.88}O_3$ and (d) antiferromagnetic $YRu_{0.88}O_3$.

Similarly, we determined electronic structure of $YRu_{0.88}O_3$ with ferromagnetic and antiferromagnetic ordering with including Hubbard U (U=3.0 eV). Ferromagnetic state is marginally lower in energy than the antiferromagnetic state by 0.5 meV/f.u. (see TABLE 5.2). "Half-semiconducting" ferromagnetic $YRuO_3$ becomes

half-metallic ferromagnetic state (E_g (up)=1.08 eV) upon introduction of 12% Ru vacancies (see Figure 5.5) in our calculations. On the other hand, the antiferromagnetic state remains semiconducting with bandgaps of 0.76 eV and 0.18 eV in the up- and down-spin channels respectively.

Table 5.2: Our estimated bandgaps and energies (with respect to ferromagnetic state) of ferromagnetic and antiferromagnetic states of nonstoichiometric $LnRuO_3$. The value of Hubbard U is given inside the parenthesis.

Compounds	Method	State	E (meV/f.u.)	$E_{g,\uparrow}$ (eV)	$E_{g,\downarrow}$ (eV)
$LaRu_{0.88}O_3$	GGA+U (3.0 eV)	FM	0.0	1.21	0.19
		AFM	9.2	0.78	0.15
$YRu_{0.88}O_3$	GGA+U (3.0 eV)	FM	0.0	1.08	0.0
		AFM	0.5	0.76	0.18

To determine the effect of cation vacancy on the oxidation and spin states of Ru atom, we project the electronic density of states on the $4d$ orbitals (see Figure 5.6). As the radial extent of $4d$ orbital is larger compared to $3d$ orbital, the crystal field effect is stronger in the former case. In the octahedral crystal field, five-fold degenerate d levels split into one triply degenerate (t_{2g}: d_{xy}, d_{yz}, d_{zx}) and one doubly degenerate (e_g: d_{z^2}, $d_{x^2-y^2}$) states, in the order of increasing energy. The crystal field splitting energy (for $4d$ orbitals) is larger than the exchange splitting (see Figure 5.6). For d^5 configuration (Ru^{3+}: $t_{2g}^5 e_g^0$), three electrons occupy $t_{2g,\uparrow}$ state and two electrons occupy $t_{2g,\downarrow}$ state (see Figure 5.6). Similarly, three electrons occupy $t_{2g,\uparrow}$ state and one electron occupies $t_{2g,\downarrow}$ state (see Figure 5.6) in the d^4 (Ru^{4+}: $t_{2g}^4 e_g^0$) configuration. Ru atoms near to the vacant site adopts +4 oxidation (S=1) state as compared to other Ru atoms with +3 oxidation (S=1/2) state (see Figure 5.6).

We measure the distortion (static Jahn-Teller distortion) of RuO_6 octahedra before and after introducing Ru vacancies in $LnRuO_3$ by defining a parameter Δ_d,

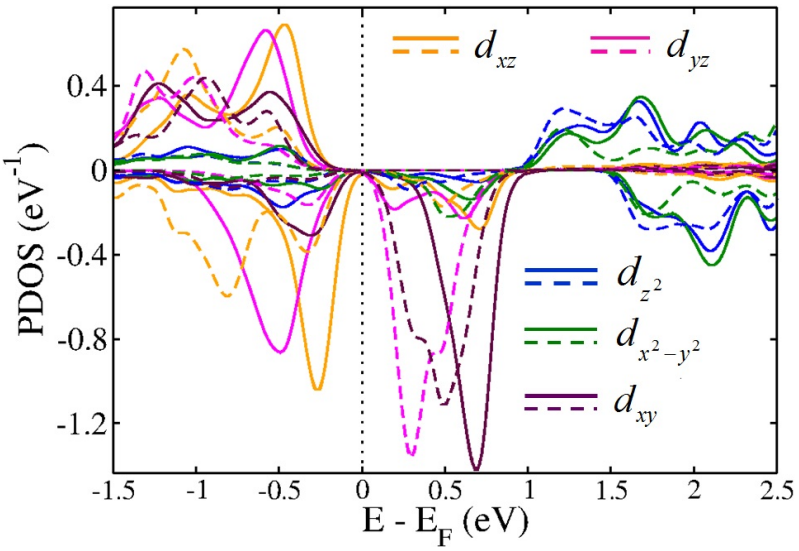

Figure 5.6: Spin resolved density of states projected on Ru $4d$ orbitals of $LaRuO_3$ and $YRuO_3$. Solid and dashed lines represent d levels of Ru atoms, which are far from and adjacent to the vacant site respectively.

given as,

$$\Delta_d = \frac{1}{\langle d \rangle} \sqrt{\frac{1}{6} \sum_{n=1}^{6} (d_n - \langle d \rangle)^2}, \tag{5.1}$$

where $\langle d \rangle$ is the average Ru-O bond length and d_n is the length of each Ru-O bond in RuO_6 octahedron. The estimated value of average Ru-O bond length in stoichiometric $LaRuO_3$ ($YRuO_3$) with ferromagnetic ordering is 2.062 Å (2.076 Å). For stoichiometric $LaRuO_3$ with ferromagnetic ordering, RuO_6 octahedra are 0.57% (0.53% for antiferromagnetic ordering) distorted compared to the ideal octahedra with vanishingly small Δ_d (see TABLE 5.3). This distortion increases by 0.27% (0.29% for antiferromagnetic ordering) as La atom is replaced by comparatively smaller Y atom (see TABLE 5.3). As Y atom is more electronegative than La atom, the relative strength of electron-lattice coupling (Δ_d) increases. It has been also observed in $RNiO_3$ perovskites (R=rare earth atom) that the strength of electron-lattice coupling (distortions of NiO_6 octahedra) is closely related to the electronegativity of rare earth atom [18]. After introducing Ru vacancies, the values of $\langle d(Ru-O) \rangle$

Table 5.3: Distortions of RuO_6 octahedra in stoichiometric and nonstoichiometric $LnRuO_3$ with ferromagnetic ordering in presence of Hubbard U (=3.0 eV) parameter.

Compund	Δ_d (%)
$LaRuO_3$	0.57
$YRuO_3$	0.84
$LaRu_{0.88}O_3$	0.7-1.1 (far from vacant site)
	1.6 (near to vacant site)
$YRu_{0.88}O_3$	0.58-1.1 (far from vacant site)
	1.4-1.8 (near to vacant site)

associated with RuO_6 octahedra near to the vacant site in both oxides with ferromagnetic ordering decrease by 1.1-1.3% (same for antiferromagnetic ordering) compared to the values of $\langle d(Ru-O)\rangle$ of stoichiometric oxides. On the other hand, the values of $\langle d(Ru-O)\rangle$ associated with RuO_6 octhedra ($LaRu_{0.88}O_3$ and $YRu_{0.88}O_3$ with ferromagnetic ordering) far from the vacant site increase by 0.4-0.6% (same for antiferromagnetic ordering) compared to their values in stoichiometric oxides. In nonstoichiometric oxides (with ferromagnetic ordering), distortions of RuO_6 octahedra near to the vacant site increase by 2-3 times (same for antiferromagnetic ordering) compared to the distortions of RuO_6 octahedra far from the vacant site (see TABLE 5.3). The distortion of RuO_6 octahedra surrounding Ru^{4+} and the value of $\langle d(Ru-O)\rangle$ are larger compared to their corresponding values associated with the octahedra surrounding Ru^{3+} ion. These findings suggest that the charge disproportionation (Ru^{3+} and Ru^{4+}) phenomenon induced by Ru vacancies in both oxides. Charge disproportionation has also been observed in $YNiO_3$ ($CaFeO_3$) where Ni^{3+} (Fe^{4+}) state disproportionate into Ni^{2+} ($Fe^{4-\delta}$) and Ni^{4+} ($Fe^{4+\delta}$) states by distorting (electron-lattice coupling) the NiO_6 (FeO_6) octahedra [18, 151].

Next, we estimate the change in cohesive energy (ΔE_{Coh}) for creating one Ru

vacancy in $LnRuO_3$ (Ln=La and Y) using:

$$\Delta E_{Coh} = E_{Coh}(Ln_8Ru_7O_{24}) + E_{Coh}(Ru) - E_{Coh}(Ln_8Ru_8O_{24}), \tag{5.2}$$

where E_{Coh}(Ru) is the total energy per Ru in the hexagonal close-packed (hcp) structure. First and third terms in the right hand side of Eq. 5.2 are total energies (eight f.u.) of nonstoichiometric and stoichiometric $LnRuO_3$. For $LaRuO_3$, the calculated value of ΔE_{Coh} (11.2 meV/f.u. for ferromagnetic state and 11.4 meV/f.u. for antiferromagnetic state) is quite small and is consistent with the experimentally observed chemical instability of $LaRuO_3$ with respect to Ru loss. We expect charge disproportionation to stabilize this system to a lower energy state. On the other hand, the value of ΔE_{Coh} (132 meV/f.u. for ferromagnetic state and 133 meV/f.u. for antiferromagnetic state) is larger for $YRuO_3$ compared to its value for $LaRuO_3$. Due to higher stability of Ru^{3+} state (finite gap in the electronic spectrum, Figure 5.3a and 5.3b) and electronegativity of Y atom compared to La atom, more energy is required to create a Ru vacancy in $YRuO_3$.

5.4 Summary

We have shown that the stoichiometric $LaRuO_3$ is a half metallic ferromagnet with a band gap of 1.06 eV in one of the spin channels. Its antiferromagnetic state is higher in energy and metallic in nature. The former conclusion is insensitive to specific values of Hubbard U parameter of the on-site correlation (U=2.0 and 3.0 eV). Inclusion of Hubbard U (U=3.0 eV) transforms metallic antiferromagnetic state to semiconducting state with a bandgap of 0.42 eV and also give realistic magnetic moment of Ru atom as 0.89 μ_B close to its experimental estimate. Hubbard U is important in getting a reasonable local magnetic moment of Ru atom (close to its experimental value). Experimentally observed bandgap of $LnRuO_3$ can be explained

with our simulations with Ru vacancies and Hubbard U as 3.0 eV. While the energy ordering of the magnetic states is unaltered with Ru vacancies, the ferromagnetic state becomes "half-semiconducting" with a gap of 0.19 eV in the down-spin channel. $LaRu_{1-\delta}O_3$ with antiferromagnetic ordering is also "half-semiconducting" with a bandgap of 0.78 eV in the up-spin channel and 0.15 eV in the down-spin channel. Stoichiometric $YRuO_3$ is semiconducting in both ferromagnetic (E_g (up)=1.48 eV and E_g (down)=0.27 eV) and antiferromagnetic (E_g=0.62 eV) ordering (Hubbard U as 3.0 eV). Ru vacancies in $YRuO_3$ alter the ordering of energy of magnetic states. $YRu_{0.88}O_3$ with ferromagnetic ordering is half-metallic in nature whereas with antiferromagnetic ordering it is "half-semiconducting" with bandgaps of 0.76 eV and 0.18 eV in up- and down-spin channels. Our calculations corroborate the simultaneous occurance of Ru^{4+} (S=1, d^4) and Ru^{3+} ions (S=1/2, d^5) observed in $LnRu_{1-\delta}O_3$. The small value of cohesive energy for creating one Ru vacancy in $LaRuO_3$ is consistent with the experimentally observed chemical instability with respect to Ru loss. Charge disproportionation in $LnRuO_3$ drives the system into a lower energy state.

Chapter 6

Competing electronic orders in ferromagnetic superconductor $Sr_{0.5}Ce_{0.5}FBiS_2$ *

6.1 Introduction

Within the extent of BCS theory (Bardeen, Cooper and Schriefer) of superconductivity, ferromagnetism and superconductivity are the two antagonistic states of mater that tend to avoid each other [153–156]. In a compound, they interact with each other through magnetic exchange and electromagnetic interactions. The magnetic exchange field in the ferromagnetically ordered state aligns the spin of the Cooper pair and eventually destroy the superconductivity. Surprisingly, the superconducting pairing is mediated via spin fluctuations rather than the usual electron-lattice coupling in high T_C superconductors and superconductivity competes with magnetism in those materials [157, 158]. For example, the superconducting transition

*This work is published in Journal of Physics: Condensed Matter [152]. URL: http://dx.doi.org/10.1088/0953-8984/28/19/195701.

temperature (T_C) increases as the magnetic ordering is suppressed with chemical doping or pressure in cuprate supercoductors [158–161]. The coexistence of ferromagnetism and superconductivity is observed in few compounds (UGe_2, URhGe and $EuFe_2(As_{0.7}P_{0.3})_2$) [162–164].

Recently, a novel BiS_2-based superconductor $Bi_4O_4S_3$ with a superconducting T_C of 8.6 K has been discovered [165]. Like in cuprate and ferro-pnictide superconductors, BiS_2 based superconductor have layered crystal structure with superconducting BiS_2 layers intercalated with block layers [162, 163, 165–167]. By changing the intercalating block layers, a varieties of superconductors are obtained [168–171]. The newly discovered ferromagnetic superconductor $Sr_{0.5}Ce_{0.5}FBiS_2$ belonging to the family of BiS_2-based superconductors has superconducting T_C of 2.5 K and Ce ions order ferromagnetically below 7.5 K [167]. $Sr_{0.5}Ce_{0.5}FBiS_2$ is generated by doping Ce atom at the Sr cites of the parent compound $SrFBiS_2$, which is superconducting [167].

Aslam *et. al.* [152] performed temperature and magnetic field dependent point contact spectroscopy measurements on polycrystalline sample of $Sr_{0.5}Ce_{0.5}FBiS_2$ and observed a double peak structure (see Figure 6.1), which is a signature of Andreev reflection in ballistic normal metal-superconductor point contacts. The value of the superconducting energy gap (2.4 meV in Figure 6.1a and 6 meV in Figure 6.1b) has been estimated from the position of the peak in such spectra [152]. An anisotropy in superconducting energy gap has been observed when currents are injected along different momentum directions of the Fermi surface [152]. From the temperature dependent point contact spectra, it has been noticed that all spectral features associated with superconductivity disappear around 5 K (see Figure 6.1c) and this temperature is two times larger than the value of superconducting T_C of bulk (2.5 K). The reason behind the two-fold enhancement of superconducting T_C in the point contact geometry is not properly understood. The value of mean field

T_C estimated from the superconducting energy gap (Δ) within the formalism of BCS theory of superconductivity is 40 K for Δ=6 meV [152], which is very large compared to superconducting T_C of bulk (2.5 K). It has been proposed that the

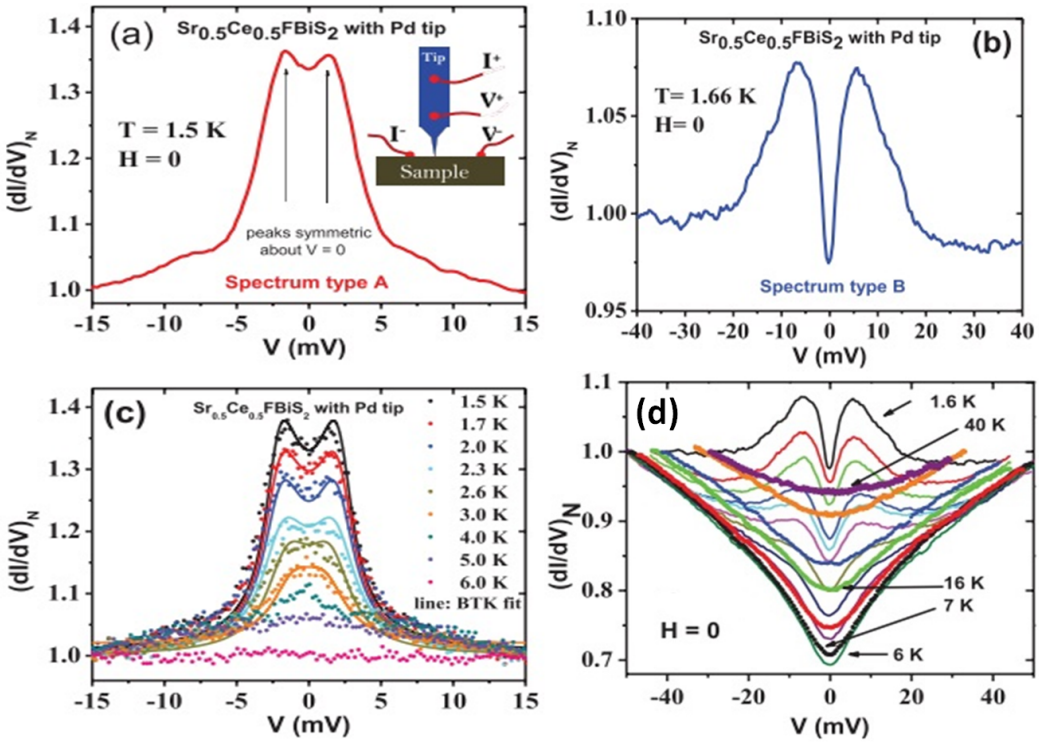

Figure 6.1: Different types of point-contact spectra obtained on $Sr_{0.5}Ce_{0.5}FBiS_2$: (a) a representative spectrum of **type A**. The double peaks structure symmetric about $V = 0$ indicated by arrows is a hallmark of Andreev reflection in NS point-contacts. (b) a representative spectrum of **type B**. (c) Temperature dependence of a spectrum of **type A** with BTK fits (indicated by solid lines) of each spectra. (d) Temperature dependence of a representative spectrum of **type B**. The spectra of **type A** and **type B** are obtained with injecting current in different directions of the Fermi surface [152].

fluctuations of the phase of superconducting order parameter persist upto 40 K (see Figure 6.1d) and a global phase coherence occur when the system is cooled down to 2.5 K [152]. The mean field T_C estimated from the energy gap associated with the spectra of type A (16 K) is also high compared to the superconducting T_C of bulk (2.5 K). Proximity of ferromagnetic fluctuations is not responsible for the pseudogap like feature (fluctuations of superconducting order parameter) observed

at high temperature as ferromagnetic transition also takes place at low temperature (7.5 K) [152]. Thus, it hints about the presence of other competing order that is responsible for the suppression of superconducting T_C.

In this work, we give evidence of competing order using first-principles which suppresses superconducting T_C in $Sr_{0.5}Ce_{0.5}FBiS_2$. We unfold the mechanism behind the two-fold enhancement of T_C after forming the contact between Pd tip and $Sr_{0.5}Ce_{0.5}FBiS_2$.

6.2 Crystal structure and computational details

The tetragonal unit cell ($P4/nmm$ symmetry) of bulk $Sr_{0.5}Ce_{0.5}FBiS_2$ contains two formula units, i.e. 10 atoms (See Figure 6.2a) with Sr, Ce, Bi and S atoms at Wyckoff position c and F atoms at Wyckoff position a [166]. The lattice parameters of unit cell of bulk $Sr_{0.5}Ce_{0.5}FBiS_2$ are a=4.0662 Å and c=13.3198 Å [152]. $SrCeF_2Bi_2S_4Pd_4$ superlattice has been constructed by adding two layers consisting of four Pd atoms on top of Bi-S layer along c direction (see Figure 6.2j).

Electronic structure calculations of bulk and superlattice are performed using density functional theory (DFT) based on full potential linearly augmented plane wave method (FP-LAPW) [172] as implemented in the WIEN2k package [173]. The spin dependent exchange correlation energy functional is treated within the framework of local density approximation. We use Hubbard U parameter of 4.59 eV to include on-site correlation to f electrons of Ce in all calculations. The muffin tin radii for Sr, Ce, F, Bi, S and Pd atoms are chosen as 2.31, 2.41, 2.14, 2.28 and 1.93 and 2.23 bohr respectively. Inside the muffin-tin sphere, the wave functions are expanded in spherical harmonics with l_{max}=10. In the interstitial region, plane wave expansion of the wave function is truncated at $R_{MT}^{min}K_{max}$=7, where K_{max} is is the cut off on wave vector of a plane wave and R_{MT}^{min} is the smallest of the atomic sphere

radii. The separation between core and valence electrons is chosen to be -7 Ry. Fourier expansion of charge density is made up to G_{max}=12 $Ry^{1/2}$. Brillouin zone (BZ) integrations in the self consistent calculations are evaluated using 300 and 338 k points in the irreducible Brillouin zone of bulk $Sr_{0.5}Ce_{0.5}FBiS_2$ and superlattice $SrCeF_2Bi_2S_4Pd_4$ respectively.

To perform linear response calculation at the zone centre (Γ point), we use norm conserving pseudo-potentials [44] with local spin density approximation for exchange correlation energy functional of Perdew-Zunger parametrized form [85] as implemented in QUANTUM ESPRESSO package [86]. We use energy cut off of 80 Ry to truncate the plane wave basis used to represent the wave functions and 320 Ry in the representation of charge density. Brillouin zone integrations are sampled on $6 \times 6 \times 2$ mesh of k-points.

We use experimental lattice parameters for the simulations of bulk $Sr_{0.5}Ce_{0.5}FBiS_2$. The optimized value of c parameter (18.13486 Å) of superlattice is obtained by minimizing the total energy while keeping a parameter fixed at its bulk value.

6.3 Results and discussions

6.3.1 Electronic structure

Within an LDA+U treatment of electronic structure, $Sr_{0.5}Ce_{0.5}FBiS_2$ is metallic in nature as there is finite electronic density of states at the Fermi level (See Figure 6.2b). The density of states in the energy range between -7.8 eV and -6 eV are composed of F $2p$ orbitals. S $3p$ and Ce $4f$ orbitals contribute to the density of states in the energy range between -6 eV and -1.5 eV constituting valence band similar to that in oxides. The states at the Fermi level of the conduction band are constituted of Bi $6p$ orbital. Ce $4f$, $5d$ and Sr $5s$ orbitals contribute to the conduction band. Up and down spin energy level of Ce $4f$ orbitals are separated

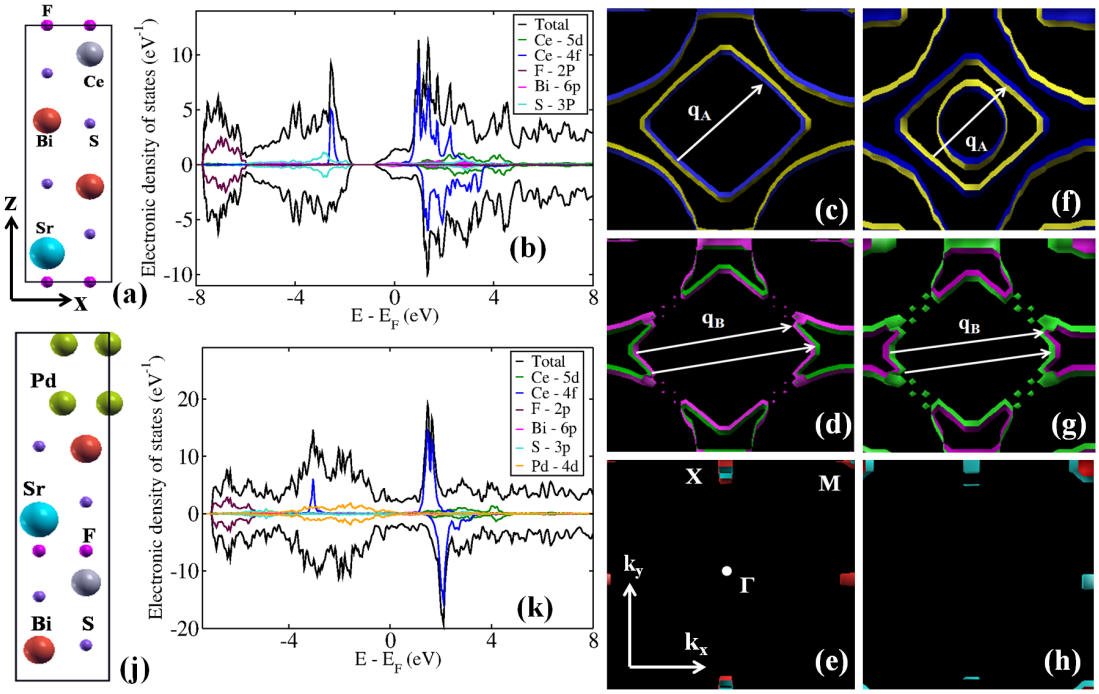

Figure 6.2: (a) Crystal structure of bulk $Sr_{0.5}Ce_{0.5}FBiS_2$. (b) spin resolved electronic density of states of bulk $Sr_{0.5}Ce_{0.5}FBiS_2$. Spin resolved Fermi surface contributed by three bands crossing Fermi level: (c) band **A** for majority spin, (d) band **B** for majority spin, (e) band **C** for majority spin, (f) band **A** for minority spin, (g) band **B** for minority spin and (h) band **C** for minority spin. Superlattice $SrCeF_2Bi_2S_4Pd_4$: (j) crystal structure and (k) spin resolved electronic density of states.

by 4 eV due to magnetic exchange coupling. One electron of Ce^{3+} ion occupies the lowest lying f level and gives local magnetic moment per Ce^{3+} as 1 μ_B, which is close to its experimental value of 0.88 μ_B (measured at 2.5 K) [152]. Three bands (A, B and C) are crossing the Fermi level in the spin resolved band structure (See Figure 6.3).

The Fermi velocity (See TABLE 6.1) is estimated from the first derivative of energy associated with an electronic band with respect to the wave vector evaluated at E_F. Our estimates of Fermi velocities are in the range of 4-6 $\times 10^5$ m/s^{-1} (as seen in TABLE 6.1).

The Fermi surface contributed by the three bands (A, B and C) are all electron-like (Figure 6.2) and involve Bi-6p orbitals. The elliptical part of the Fermi surface

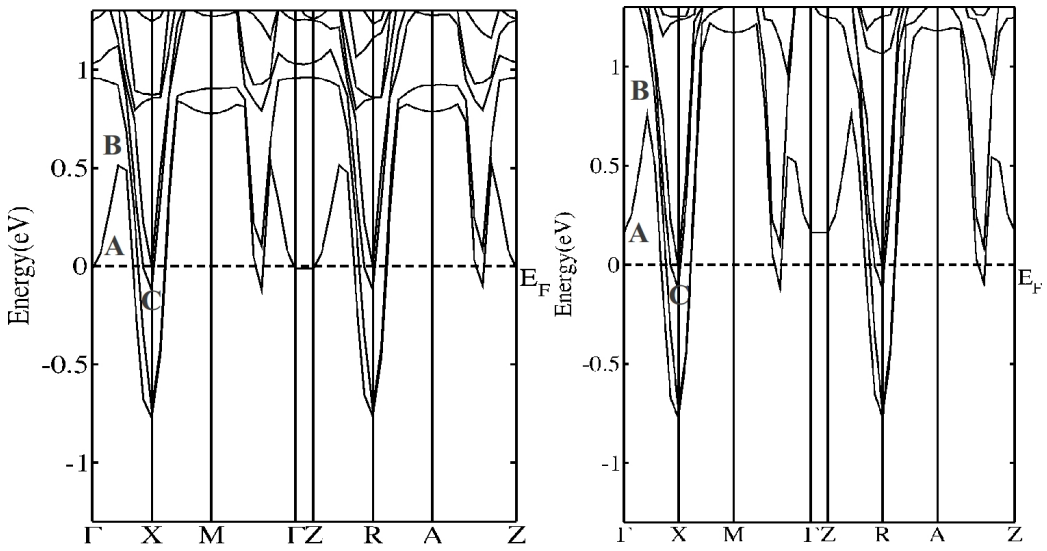

Figure 6.3: Spin resolved electronic structure of bulk $Sr_{0.5}Ce_{0.5}FBiS_2$: (a) band structure for majority spin and (b) band structure for minority spin.

Table 6.1: Fermi velocities in the bands crossing Fermi level of bulk $Sr_{0.5}Ce_{0.5}FBiS_2$.

Up spin band	v_F (10^5 m/s)	Down spin band	v_F (10^5 m/s)
A	5.96	A	5.63
B	5.75	B	5.41
C	4.31	C	4.19

(centered at Γ point of the Brillouin zone) associated with band A of the minority spin distinguishes itself from that of the majority spin. The spin-resolved Fermi surfaces contributed by bands B and C are similar. The nonzero nesting wave vectors connecting the parallel flat parts of the spin resolved Fermi surfaces are q_A=0.392 $Å^{-1}$ for band A and q_B=0.506 $Å^{-1}$ for band B. Through a strong electron-phonon coupling, they are responsible for creating charge density waves as competing instability in the system. This is consistent with the observed pseudogap-like feature in the experimental data at higher temperatures.

Next, we determine the phonon spectrum of $Sr_{0.5}Ce_{0.5}FBiS_2$ at Γ point to identify the phonon mode, which shows strong electron-phonon coupling.

6.3.2 Electron phonon coupling

Using linear response calculation, we determined the zone-centre phonons (see Figure 6.4) of bulk $Sr_{0.5}Ce_{0.5}FBiS_2$. Its 27 optical modes are decomposed into $4A_{1g} + B_{1g} + 4\ A_{2u} + 5\ E_g + 4\ E_u$ [174,175]. Out of three acoustic mode, two have E_u symmetry and one has A_{2u} symmetry. The phonon modes with A_{1g}, B_{1g} and E_g symmetry are Raman active and modes with A_{2u} and E_u symmetry are IR active [174,176]. One Raman active A_{1g} phonon mode with frequency 46 cm^{-1} (See Figure 6.4), which involves the displacement of Bi and S atoms, shows strong electron phonon coupling (λ=0.34), which can be understood from the fact that electronic density of states at the Fermi level arise from Bi 6p orbitals. After freezing the A_{1g} phonon mode with frequency 46 cm^{-1}, we see a notable change in the electronic structure. Freezing of this particular mode changes the electrostatic potential surrounding the Ce and Sr atom and shifts up Ce $4f$ and Sr $5s$ level by 2 eV and 0.5 eV respectively (See Figure 6.4).

6.3.3 Interaction with Pd layers

In order to understand the reason behind the two-fold enhancement of T_C in the point contact geometry, we examine the interaction of $Sr_{0.5}Ce_{0.5}FBiS_2$ with Pd through determination of electronic structure of $SrCeF2Bi_2S_4Pd_4$ superlattice. The metallic nature of $Sr_{0.5}Ce_{0.5}FBiS_2$ is retained even after its interaction with two atomic layers of Pd. However, this interaction perturbs the energy levels of all the atoms.

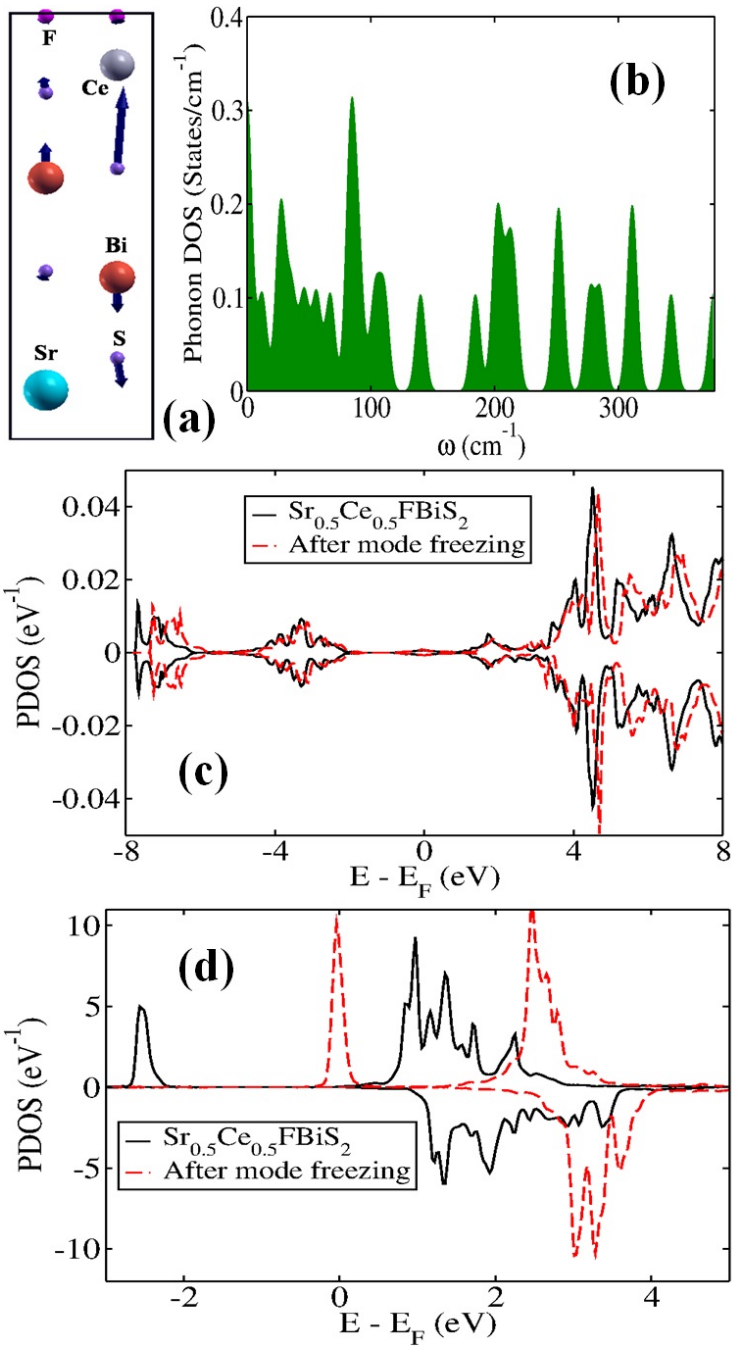

Figure 6.4: (a) Atomic displacements of A_{1g} phonon mode having frequency 46 cm $^{-1}$, which exhibits a strong electron phonon coupling and (b) distribution of frequency of phonons at Γ point of bulk $Sr_{0.5}Ce_{0.5}FBiS_2$. Change in the electronic density of states of bulk $Sr_{0.5}Ce_{0.5}FBiS_2$ after freezing the phonon mode with frequency 46 cm^{-1}: (c) projected on Sr $5s$ orbital and (d) projected on Ce $4f$ orbital.

The states in the energy range between -7.9 eV and -5 eV associated with F $2p$ orbitals get shifted down in energy with respect to E_F. Nonzero density of states at the Fermi level arises from Pd $4d$, S $3p$ and Bi $6p$ orbitals (see Figure 6.2k), reflecting a strong hybridization between Pd $4d$ and S $3p$ orbitals which is not present in the electronic structure of the bulk. Local magnetic moment per cell (1 μ_B) remains unchanged as there is no contribution coming from Pd $4d$ orbitals to magnetic moment. We notice interaction with Pd leads to an increase in the density of states at the Fermi level (N(0)) of the superlattice by 78% compared to bulk.

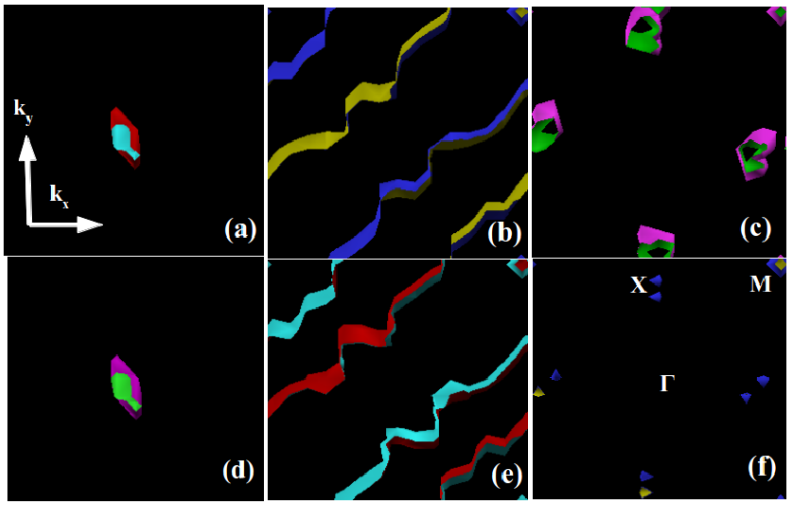

Figure 6.5: Spin resolved Fermi surface contributed by three bands crossing Fermi level of superlattice: (a) band **A** for majority spin, (b) band **B** for majority spin, (c) band **C** for majority spin, (d) band **A** for minority spin, (e) band **B** for minority spin and (f) band **C** for minority spin.

On the other hand, weaker nesting of multi-band Fermi surface of the superlattice (see Figure 6.5) compared to the bulk suggests suppression of the charge density wave like instability and thus results in the enhancement of the superconducting transition temperature under the point-contacts. We note that the increase in density of states at the Fermi level is expected to make the phase of the order parameter stiffer against fluctuations. Depending on the order of shift in stiffness, the critical temperature may increase up to a maximum of the mean field critical temperature. This further

supports the claim that the fluctuations of the phase of the complex superconducting order parameter caused by competing orders lead to the formation of a pseudogap in $Sr_{0.5}Ce_{0.5}FBiS_2$.

6.4 Summary

We identify the competing order responsible for the observed pseudogap-like feature (also linked with fluctuations of superconducting order parameter up to 40 K) in $Sr_{0.5}Ce_{0.5}FBiS_2$. Using first-principles theoretical analysis, we show that charge density wave like instability can be caused by the nesting of multi-band Fermi surface in its ferromagnetic state, and claim that it suppresses the superconducting T_C. We identify the soft Raman active phonon mode involving eigen-displacements of Bi and S atoms, which couples strongly (λ=0.34) with electrons. The electrostatic interaction of a few atomic layers of Pd with $Sr_{0.5}Ce_{0.5}FBiS_2$ weakens the nesting of Fermi surface and the competing instability, and eventually increases the superconducting T_C (5 K) through suppression of charge density wave-like instabilities.

Chapter 7

Summary

The central theme of this thesis is to explain the microscopic mechanism of unusual physical phenomena observed in complex oxides and sulphides by considering the coupling between the relevant degrees of freedom. We have investigated the effects of spin-spin, spin-phonon, strain-phonon and phonon-phonon couplings on Néel and structural transitions. In our analysis, we have employed a combination of first-principles calculations based on density functional theory, phenomenological theory and effective Hamiltonians.

We have shown that magnetic frustration and spin-orbit coupling in hexagonal $YMnO_3$ give rise to magneto-crystalline anisotropy in the noncollinear ordering of magnetic moments and a consequent gap in the electronic spectrum even with vanishing on-site electronic correlations. We have explained the observed magnitude of magnetic moment of Mn^{3+} ion by considering the splitting and ordering of d levels induced by crystal field, magnetic exchange and the spin-orbit coupling. We establish that a strong and anisotropic coupling of spins with Γ_1 phonon mode and strain stabilizes the ordering of spins according to Γ_3 symmetry and constitutes the microscopic mechanism of the "giant" magnetoelastic effect observed at Néel temperature. We highlight the presence of magnetic state with Γ_1 symmetry at the

domain walls separating two magnetic domains which are related by time reversal symmetry. Magnetic domains get locked to the structural domains because of the spin-phonon coupling. We find two topologically distinct magnetic states below T_N: (a) stripe domains of magnetic ordering and (b) magnetic vortex and antivortex states. Magnetic vortex and antivortex states arise at the intersection of six magnetic domain walls and result in the formation of structural vortex and antivortex states.

Two main sources of errors in estimating ferroelectric transition temperatures of perovskite oxides from first-principles arise from (a) inaccurate estimation of lattice constant which leads to errors in total energy surface as a function of soft mode amplitude and (b) truncation of the subspace in construction of effective Hamiltonian. We have demonstrated that the accurate estimation of lattice parameters of ferroelectric oxides using SCAN metaGGA functional allows more realistic estimation of total energy surfaces. The enhancement in the calculated depth of the potential well results in better estimation of ferroelectric T_C's. In addition, we have quantified the consequences of truncation of the subspace of the effective Hamiltonian by using the lowest-order coupling between soft and higher-energy optic modes in estimation of T_C's. Fourth-order anharmonic coupling between soft polar and higher-energy phonon modes causes notable increment in the depth of the potential energy well and consequently enhances the estimated T_C's. At the interfaces in hetero-structures or superlattices based on perovskite oxides, details of atomic-scale structure depend on the mismatch between lattice constants, and electronic band offsets depend on band gaps. We expect the SCAN metaGGA-based DFT to be very effective in simulations of perovskite hetero-structures as estimates of both lattice constants and band gaps are consistently improved.

We have continued our investigations on recently discovered lanthanide ruthenium oxides by exploring their electronic properties. We predict the stoichiometric

$LaRuO_3$ to be a half-metallic ferromagnet in its ground state. In contrast, stoichiometric $YRuO_3$ is found to be semiconducting with both ferromagnetic and antiferromagnetic ordering. Our analysis confirms the simultaneous occurrence of Ru^{4+} (S=1, d^4) and Ru^{3+} ions (S=1/2, d^5) in $LnRu_{1-\delta}O_3$. Gap in the electronic spectrum induced by cation vacancies in nonstoichiometric $LnRuO_3$ is consistent with experimental observations. A small value of cohesive energy per one Ru vacancy in $LaRuO_3$ along with the opening of gap highlight its chemical instability with respect to Ru loss. We propose charge disproportionation in $LnRuO_3$ as the mechanism that stabilizes the system to a lower energy state. In contrast to $LaRuO_3$, larger energy cost of Ru vacancies in $YRuO_3$ is due to the higher stability of Ru^{3+} ion and electronegativity of Y.

We explain the mechanism of competing orders relevant to the experimentally observed pseudogap-like feature in ferromagnetic superconductor $Sr_{0.5}Ce_{0.5}FBiS_2$. We demonstrate that electronic instability in $Sr_{0.5}Ce_{0.5}FBiS_2$ is induced by the nesting of multi-band Fermi surfaces. This instability competes with superconducting instability and suppresses the superconducting T_C through the fluctuations of the phase of superconducting order parameter. We identify the soft Raman active phonon mode involving eigen-displacements of Bi and S atoms, which couples strongly (λ=0.34) with electrons. We establish that the electrostatic interaction of few ad-layers of Pd with $Sr_{0.5}Ce_{0.5}FBiS_2$ weakens the nesting of Fermi surface and the competing instability. Eventually this increases the superconducting T_C through suppression of charge density wave-like instabilities.

We summarize our work presented in this thesis in a schematic diagram (see Figure 7.1) which expresses the central theme of the topics covered. In summary, we highlighted how the couplings between different degrees of freedom at the microscopic level give rise to unexpected physical phenomena in complex oxides and sulphides.

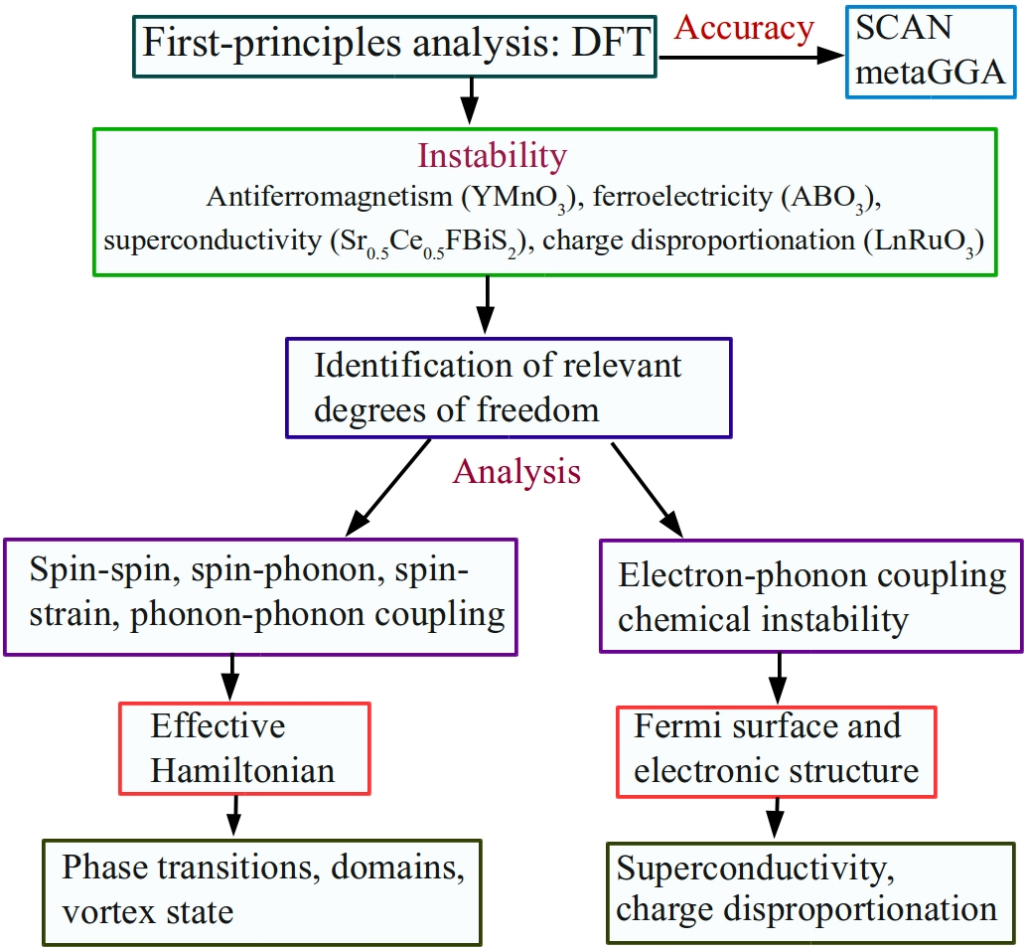

Figure 7.1: Schematic summarizing all the work presented in this thesis.

There are three directions in which further work can be taken up. Firstly, the dynamics of topological defects and domains in multiferroic $YMnO_3$ can be analyzed in future. Secondly, the first-principles studies based on SCAN metaGGA functional can be extended to (a) magnetic oxides with transition metal ion (d^n, n≠0) and (b) hetero-structures of ABO_3 perovskites.

Bibliography

[1] Y. Ying *et al.*, Phys. Rev. B **74**, 144433 (2006).

[2] J. C. Loudon, N. D. Mathur, and P. A. Midgley, Nature **420**, 797 (2002).

[3] Y. Moritomo, A. Asamitsu, H. Kuwahara, and Y. Tokura, Nature **380**, 141 (1996).

[4] S.-W. Cheong and M. Mostovoy, Nat Mater **6**, 13 (2007).

[5] J. C. Loudon, Phys. Rev. Lett. **109**, 267204 (2012).

[6] T. Asada and Y. Koyama, Phys. Rev. B **70**, 104105 (2004).

[7] Z. Wu and R. E. Cohen, Phys. Rev. Lett. **95**, 037601 (2005).

[8] C. N. R. Rao, The Journal of Physical Chemistry B **104**, 5877 (2000).

[9] H. Maeda, Y. Tanaka, M. Fukutomi, and T. Asano, Japanese Journal of Applied Physics **27**, L209 (1988).

[10] S. Yamaguchi, Y. Okimoto, H. Taniguchi, and Y. Tokura, Phys. Rev. B **53**, R2926 (1996).

[11] S. Lupi *et al.*, Nature Communications **1**, 105 (2010).

[12] B. Wul and J. M. Goldman, C. R. Acad. Sci. URRS **46**, 139 (1945).

[13] A. von Hippel, R. G. Breckenridge, F. G. Chesley, and L. Tisza, Industrial & Engineering Chemistry **38**, 1097 (1946).

[14] W. Kohn and L. J. Sham, Phys. Rev. **140**, A1133 (1965).

[15] J. M. D. Coey, M. Venkatesan, and H. Xu, *Functional Metal Oxides* (Wiley-VCH Verlag GmbH & Co. KGaA, Germany, 2013), pp. 1–49.

[16] S. Blundell, *Magnetism in Condensed Matter*, *Oxford Master Series in Condensed Matter Physics* (Oxford University Press, Oxford, 2001), Chap. 3-4.

[17] V. I. Anisimov, I. S. Elfimov, N. Hamada, and K. Terakura, Phys. Rev. B **54**, 4387 (1996).

[18] J. A. Alonso *et al.*, Phys. Rev. Lett. **82**, 3871 (1999).

[19] J. Yamashita, Journal of the Physical Society of Japan **9**, 339 (1954).

[20] V. Garcia *et al.*, Nature **460**, 81 (2009).

[21] R. Guo *et al.*, Nature Communications **4**, (2011).

[22] J. F. Scott, Ferroelectrics **314**, 207 (2005).

[23] J. Valasek, Phys. Rev. **17**, 475 (1921).

[24] G. Busch and P. Scherrer, Naturwissenschaften **23**, 737 (1935).

[25] R. S. PEASE and G. E. BACON, Nature **173**, 443 (1954).

[26] W. Cochran, Advances in Physics **9**, 387 (1960).

[27] R. E. Cohen, Nature **358**, 136 (1992).

[28] U. V. Waghmare and K. M. Rabe, Phys. Rev. B **55**, 6161 (1997).

[29] U. V. Waghmare, N. A. Spaldin, H. C. Kandpal, and R. Seshadri, Phys. Rev. B **67**, 125111 (2003).

[30] P. Hohenberg and W. Kohn, Phys. Rev. **136**, B864 (1964).

[31] M. Born and R. Oppenheimer, Annalen der Physik **389**, 457 (1927).

[32] A. K. Rajagopal and J. Callaway, Phys. Rev. B **7**, 1912 (1973).

[33] J. P. Perdew and A. Zunger, Phys. Rev. B **23**, 5048 (1981).

[34] J. P. Perdew, K. Burke, and M. Ernzerhof, Phys. Rev. Lett. **77**, 3865 (1996).

[35] J. P. Perdew, S. Kurth, A. c. v. Zupan, and P. Blaha, Phys. Rev. Lett. **82**, 2544 (1999).

[36] J. Tao, J. P. Perdew, V. N. Staroverov, and G. E. Scuseria, Phys. Rev. Lett. **91**, 146401 (2003).

[37] J. Sun, A. Ruzsinszky, and J. P. Perdew, Phys. Rev. Lett. **115**, 036402 (2015).

[38] J. Sun *et al.*, Nat Chem **8**, 831 (2016).

[39] D. A. Kitchaev *et al.*, Phys. Rev. B **93**, 045132 (2016).

[40] Z.-H. Yang, H. Peng, J. Sun, and J. P. Perdew, Phys. Rev. B **93**, 205205 (2016).

[41] P. Giannozzi *et al.*, Journal of Physics: Condensed Matter **21**, 395502 (2009).

[42] X. Gonze *et al.*, Computational Materials Science **25**, 478 (2002).

[43] O. K. Andersen, Phys. Rev. B **12**, 3060 (1975).

[44] D. R. Hamann, M. Schlüter, and C. Chiang, Phys. Rev. Lett. **43**, 1494 (1979).

[45] D. Vanderbilt, Phys. Rev. B **41**, 7892 (1990).

[46] A. J. Cohen, P. Mori-Sánchez, and W. Yang, Science **321**, 792 (2008).

[47] A. Paul, P. Sharma, and U. V. Waghmare, Phys. Rev. B **92**, 054106 (2015).

[48] N. Ray and U. V. Waghmare, Phys. Rev. B **77**, 134112 (2008).

[49] H. Das, U. V. Waghmare, T. Saha-Dasgupta, and D. D. Sarma, Phys. Rev. Lett. **100**, 186402 (2008).

[50] T. Egami *et al.*, Physica C: Superconductivity **470, Supplement 1**, S294 (2010), proceedings of the 9th International Conference on Materials and Mechanisms of Superconductivity.

[51] P. Kumar *et al.*, J. Phys.: Condens. Matter **23**, 255403 (2011).

[52] S. Kamba *et al.*, Phys. Rev. B **89**, 064308 (2014).

[53] C. J. Fennie and K. M. Rabe, Phys. Rev. Lett. **97**, 267602 (2006).

[54] J. H. Lee *et al.*, Phys. Rev. B **88**, 174426 (2013).

[55] Y. Zhou and K. M. Rabe, Phys. Rev. B **88**, 094416 (2013).

[56] T. Birol *et al.*, Current Opinion in Solid State and Materials Science **16**, 227 (2012), multiferroics.

[57] J. A. Ricodeau, Phys. Rev. B **7**, 4950 (1973).

[58] S. Zhang *et al.*, Sci. Rep. **4**, 3727 (2014).

[59] U. V. Waghmare, *Multiferroics with Magnetoelectric Coupling* (Wiley-VCH Verlag GmbH & Co. KGaA, ADDRESS, 2013), pp. 267–283.

[60] M. L. Plumer and M. B. Walker, J. Phys. C: Solid State Phys. **15**, 7181 (1982).

[61] H. Das *et al.*, Nat Commun **5**, (2014).

[62] S. Artyukhin, K. T. Delaney, N. A. Spaldin, and M. Mostovoy, Nat Mater **13**, 42 (2013).

[63] X. Fabrèges *et al.*, Phys. Rev. Lett. **103**, 067204 (2009).

[64] T. Katsufuji *et al.*, Phys. Rev. B **64**, 104419 (2001).

[65] F. Ye *et al.*, Phys. Rev. B **73**, 220404 (2006).

[66] S. Lee *et al.*, Nature **451**, 805 (2007).

[67] A. Muñoz *et al.*, Phys. Rev. B **62**, 9498 (2000).

[68] K. Lukaszewicz and J. Karut-Kalicinska, Ferroelectrics **7**, 81 (1974).

[69] C. J. Fennie and K. M. Rabe, Phys. Rev. B **72**, 100103 (2005).

[70] B. B. VanAken, T. T. Palstra, A. Filippetti, and N. A. Spaldin, Nat Mater **3**, 164 (2004).

[71] T. Choi *et al.*, Nat Mater **9**, 253 (2010).

[72] S. C. Chae *et al.*, Proceedings of the National Academy of Sciences **107**, 21366 (2010).

[73] M. Fiebig *et al.*, Phys. Rev. Lett. **84**, 5620 (2000).

[74] J. Park *et al.*, Phys. Rev. B **79**, 064417 (2009).

[75] I. V. Solovyev, M. V. Valentyuk, and V. V. Mazurenko, Phys. Rev. B **86**, 054407 (2012).

[76] S. Petit *et al.*, Phys. Rev. Lett. **99**, 266604 (2007).

[77] H. Fukumura *et al.*, J. Phys.: Condens. Matter **19**, 365239 (2007).

[78] M. Fiebig *et al.*, Nature **419**, 818 (2002).

[79] E. Hanamura, K. Hagita, and Y. Tanabe, Journal of Physics: Condensed Matter **15**, L103 (2003).

[80] E. Hanamura and Y. Tanabe, Journal of the Physical Society of Japan **72**, 2959 (2003).

[81] A. Prikockytė *et al.*, Phys. Rev. B **84**, 214301 (2011).

[82] J. E. Medvedeva *et al.*, J. Phys.: Condens. Matter **12**, 4947 (2000).

[83] C. Zhong, Q. Jiang, H. Zhang, and X. Jiang, Applied Physics Letters **94**, (2009).

[84] A. D. Corso and A. M. Conte, Phys. Rev. B **71**, 115106 (2005).

[85] J. P. Perdew and A. Zunger, Phys. Rev. B **23**, 5048 (1981).

[86] P. Giannozzi *et al.*, J. Phys.: Condens. Matter **21**, 395502 (2009).

[87] R. D. King-Smith and D. Vanderbilt, Phys. Rev. B **47**, 1651 (1993).

[88] K. Kritayakirana, P. Berger, and R. Jones, Optics Communications **1**, 95 (1969).

[89] C. Degenhardt *et al.*, Applied Physics B **73**, 139 (2001).

[90] B. H. Bransden and C. J. Joachain, *Physics of Atoms and Molecules* (Pearson Education, Noida, India, 2006), Chap. 6-8.

[91] Isotropy software suite, `http://iso.byu.edu`.

[92] M. N. Iliev *et al.*, Phys. Rev. B **56**, 2488 (1997).

[93] P. Ghosez, J.-P. Michenaud, and X. Gonze, Phys. Rev. B **58**, 6224 (1998).

[94] M. Zaghrioui, V. Ta Phuoc, R. A. Souza, and M. Gervais, Phys. Rev. B **78**, 184305 (2008).

[95] D.-Y. Cho *et al.*, Phys. Rev. Lett. **98**, 217601 (2007).

[96] M. Poirier, F. Laliberté, L. Pinsard-Gaudart, and A. Revcolevschi, Phys. Rev. B **76**, 174426 (2007).

[97] A. Paul, J. Sun, J. P. Perdew, and U. V. Waghmare, Phys. Rev. B **95**, 054111 (2017).

[98] M. Lines and A. Glass, *Principles and Applications of Ferroelectrics and Related Materials*, *International series of monographs on physics* (OUP, Oxford, 1977).

[99] R. Waser, *Nanoelectronics and Information Technology* (Wiley, New York, 2012).

[100] R. D. King-Smith and D. Vanderbilt, Phys. Rev. B **49**, 5828 (1994).

[101] K. M. Rabe, *Antiferroelectricity in Oxides: A Reexamination* (Wiley-VCH Verlag GmbH & Co. KGaA, Verlag, 2013), pp. 221–244.

[102] T. Nishimatsu, M. Iwamoto, Y. Kawazoe, and U. V. Waghmare, Phys. Rev. B **82**, 134106 (2010).

[103] U. V. Waghmare, Accounts of Chemical Research **47**, 3242 (2014).

[104] W. Zhong, D. Vanderbilt, and K. M. Rabe, Phys. Rev. B **52**, 6301 (1995).

[105] D. J. Singh and L. L. Boyer, Ferroelectrics **136**, 95 (1992).

[106] T. Hashimoto *et al.*, Japanese Journal of Applied Physics **43**, 6785 (2004).

[107] D. I. Bilc *et al.*, Phys. Rev. B **77**, 165107 (2008).

[108] J. P. Perdew, K. Burke, and M. Ernzerhof, Phys. Rev. Lett. **80**, 891 (1998).

[109] Z. Wu and R. E. Cohen, Phys. Rev. B **73**, 235116 (2006).

[110] G. Kresse and J. Furthmüller, Phys. Rev. B **54**, 11169 (1996).

[111] G. Kresse and J. Furthmller, Computational Materials Science **6**, 15 (1996).

[112] G. Kresse and D. Joubert, Phys. Rev. B **59**, 1758 (1999).

[113] T. Nishimatsu, U. V. Waghmare, Y. Kawazoe, and D. Vanderbilt, Phys. Rev. B **78**, 104104 (2008).

[114] FERAM, `http://loto.sourceforge.net/feram/`.

[115] S. D. Bond, B. J. Leimkuhler, and B. B. Laird, Journal of Computational Physics **151**, 114 (1999).

[116] A. I. Lebedev, Phys. Status Solidi B **249**, 789 (2012).

[117] G. H. Kwei, A. C. Lawson, S. J. L. Billinge, and S. W. Cheong, The Journal of Physical Chemistry **97**, 2368 (1993).

[118] G. Shirane, H. Danner, A. Pavlovic, and R. Pepinsky, Phys. Rev. **93**, 672 (1954).

[119] A. I. Frenkel *et al.*, Phys. Rev. B **56**, 10869 (1997).

[120] L. F. Wan, T. Nishimatsu, and S. P. Beckman, Journal of Applied Physics **111**, (2012).

[121] S. Piskunov, E. Heifets, R. Eglitis, and G. Borstel, Computational Materials Science **29**, 165 (2004).

[122] R. O. Bell and G. Rupprecht, Phys. Rev. **129**, 90 (1963).

[123] Z. Li, M. Grimsditch, C. Foster, and S.-K. Chan, Journal of Physics and Chemistry of Solids **57**, 1433 (1996).

[124] I. Tomeno *et al.*, Phys. Rev. B **80**, 104101 (2009).

[125] K. Ueda *et al.*, Journal of Physics: Condensed Matter **10**, 3669 (1998).

[126] W. Zhou, H. Deng, P. F, and J. Chu, Applied Physics Letters **105**, (2014).

[127] G. Li *et al.*, Journal of Solid State Chemistry **180**, 2845 (2007).

[128] S. Piskunov *et al.*, Computational Materials Science **41**, 195 (2007).

[129] R. Eglitis, Solid State Ionics **230**, 43 (2013).

[130] C.-Z. Wang, R. Yu, and H. Krakauer, Phys. Rev. B **54**, 11161 (1996).

[131] R. Wahl, D. Vogtenhuber, and G. Kresse, Phys. Rev. B **78**, 104116 (2008).

[132] O. Dieguez, K. M. Rabe, and D. Vanderbilt, Phys. Rev. B **72**, 144101 (2005).

[133] K. M. Rabe and U. V. Waghmare, Phys. Rev. B **52**, 13236 (1995).

[134] T. Nishimatsu *et al.*, Journal of the Physical Society of Japan **81**, 124702 (2012).

[135] C. J. Johnson, Appl. Phys. Lett. **7**, 221 (1965).

[136] H. Krakauer *et al.*, Journal of Physics: Condensed Matter **11**, 3779 (1999).

[137] G. Shirane, R. Pepinsky, and B. C. Frazer, Acta Cryst. **9**, 131 (1956).

[138] Y. Tokura, Reports on Progress in Physics **69**, 797 (2006).

[139] R. J. Cava, Dalton Trans. 2979 (2004).

[140] G. Cao *et al.*, Phys. Rev. B **56**, R2916 (1997).

[141] S. A. Grigera *et al.*, Science **294**, 329 (2001).

[142] H. T. Dang, J. Mravlje, A. Georges, and A. J. Millis, Phys. Rev. B **91**, 195149 (2015).

[143] J.-W. G. Bos and J. P. Attfield, Chemistry of Materials **16**, 1822 (2004).

[144] A. C. Mclaughlin, J. P. Attfield, U. Asaf, and I. Felner, Phys. Rev. B **68**, 014503 (2003).

[145] W. Klein, R. K. Kremer, and M. Jansen, J. Mater. Chem. **17**, 1356 (2007).

[146] S. A. J. Kimber *et al.*, Phys. Rev. Lett. **108**, 217205 (2012).

[147] M. D. Silverman and H. A. Levy, Journal of the American Chemical Society **76**, 3317 (1954).

[148] A. Sinclair *et al.*, Angewandte Chemie International Edition **53**, 8343 (2014).

[149] K. W. Plumb *et al.*, Phys. Rev. B **90**, 041112 (2014).

[150] G. Kresse and J. Hafner, Journal of Physics: Condensed Matter **6**, 8245 (1994).

[151] M. Takano *et al.*, Phys. Rev. Lett. **67**, 3267 (1991).

[152] M. Aslam *et al.*, Journal of Physics: Condensed Matter **28**, 195701 (2016).

[153] J. Bardeen, L. N. Cooper, and J. R. Schrieffer, Phys. Rev. B **106**, 162 (1957).

[154] A. Buzdin, Nature Materials **3**, 751 (2004).

[155] N. F. Berk and J. R. Schrieffer, Phys. Rev. Lett. **17**, 433 (1966).

[156] B. Lorenz and C.-W. Chu, Nature Materials **4**, 516 (2005).

[157] N. D. Mathur *et al.*, Nature (London) **394**, 39 (1998).

[158] R. E. Baumbach *et al.*, Phys. Rev. B **89**, 094408 (2014).

[159] M. S. Torikachvili, S. L. Bud'ko, N. Ni, and P. C. Canfield, Phys. Rev. Lett. **101**, 057006 (2008).

[160] Y. Kamihara, T. Watanabe, M. Hirano, and H. Hosono, Journal of the American Chemical Society **130**, 3296 (2008).

[161] Y. Luo *et al.*, Phys. Rev. B **83**, 054501 (2011).

[162] D. Aoki *et al.*, Nature **413**, 613 (2001).

[163] S. S. Saxena *et al.*, Nature **406**, 587 (2000).

[164] Z. Ren *et al.*, Phys. Rev. Lett. **102**, 137002 (2009).

[165] Y. Mizuguchi *et al.*, Phys. Rev. B **86**, 220510 (2012).

[166] R. Jha, B. Tiwari, and V. P. S. Awana, Journal of Applied Physics **117**, 013901 (2015).

[167] L. Li *et al.*, Phys. Rev. B **91**, 014508 (2015).

[168] J. Xing *et al.*, Phys. Rev. B **86**, 214518 (2012).

[169] V. Awana *et al.*, Solid State Communications **157**, 21 (2013).

[170] S. Demura *et al.*, Journal of the Physical Society of Japan **82**, 033708 (2013).

[171] Y. Mizuguchi *et al.*, Journal of the Physical Society of Japan **81**, 114725 (2012).

[172] D. Singh and L. Nordstrom, *Planewaves, Pseudopotentials and the LAPW Method* (Springer, US, 2006), pp. 43–49.

[173] P. Blaha *et al.*, WIEN2k: An Augmented Plane Waves plus Local Orbitals Program for Calculating Crystal Properties (2001).

[174] E. Kroumova *et al.*, Phase Transitions **76**, 155 (2003).

[175] S. F. Wu *et al.*, Phys. Rev. B **90**, 054519 (2014).

[176] V. G. Hadjiev *et al.*, Phys. Rev. B **77**, 220505 (2008).